Large Structural Change of Aggregation-Induced Emission (AIE) Molecules in the Excited State

励起状態における凝集誘起型発光(AIE)分子の大きな構造変化

Takashi MACHIDA

2020

Graduate School of Chemical Science and Engineering
Hokkaido University

Large Structural Change of Aggregation-Induced Emission (AIE) Molecules in the Excited State

励起状態における凝集誘起型発光(AIE)分子の大きな構造変化

Takashi MACHIDA

2020

Graduate School of Chemical Science and Engineering
Hokkaido University

Contents

Chapter I ----------1

General Introduction

Chapter II ----------17

The effect of liquefaction to AIE behavior

Chapter III ----------39

The effect of C=C bond twist to AIE behavior

Chapter IV ----------66

The effect of crosslinking with oligo-ethyleneglycol chains to AIE behavior

Chapter V ----------104

Photo-induced pyramidal inversion of phosphines involved in the AIE behavior

Chapter VI ----------144

Concluding Remarks

List of Publication ----------147

Chapter I

General Introduction

Chapter I

General Introduction

1. Organic luminescence molecules

Some highly π-conjugated organic molecules, when excited by absorbing energy such as light, emit energy as light rather than spending energy on intramolecular rotations or vibrations. Such molecules, called luminescence molecules or luminogens, have long been used as optical brighteners,[1] luminescence markers,[2] and clinical diagnostic reagents.[3] The reason why organic luminescence molecules have been used in a wide range of fields is that they have a number of advantages compared to the inorganic light emitting materials; high fluorescence quantum yield (Φ_f), flexibility, tailorbility, low cost and low toxicity (Figure 1).

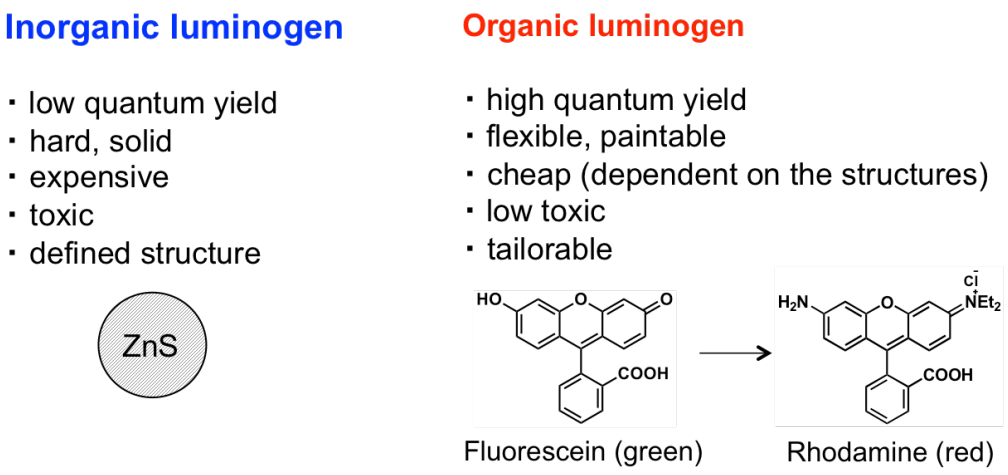

Figure 1. Comparison of inorganic and organic luminogens.

Since the fluorescence wavelength (λ_f) is determined by the energy difference (ΔE) between the singlet excited state (S_1) and the singlet ground state (S_0), the luminescence color can be controlled by proper chemical modification.[7,8] The longer-wavelength shift in luminescence by the ring expansion is the most straightforward method for luminescence color tuning because ΔE is dependent on the π-conjugated length (Figure 2). On the other hand, since the intramolecular motions such as rotations, vibrations and stretchings decrease the Φ_f, rigid luminescence molecules show intense emission with high Φ. The molecules, having longer λ_f and higher Φ_f, are desirable for any applications, therefore rigid luminogens with extended π-conjugation have been developed.

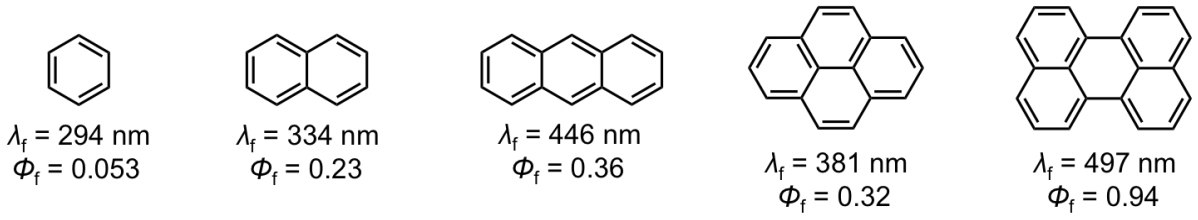

Figure 2. Fluorescence longer-wavelength maxima (λ_f) and fluorescence quantum yields (Φ_f) of typical rigid π-conjugated molecules. They were measured in the diluted cyclohexane solution.[6]

2. Aggregation-caused quenching (ACQ)

In these days, luminescence molecules have been applied for optoelectronic devices such as organic light emitting diodes (OLEDs), in which they are used as solid film.[7,8] Thus it is necessary to develop the molecules that can maintain high Φ_f in the solid state. However, the development of such molecules is challenging task, because the luminescence from the densely aggregated molecules are often quenched. This quenching behavior, called aggregation-caused quenching (ACQ), is thought to be caused by the formation of delocalized excitons via strong intermolecular π-π stacking interaction.[9,10]

For example, fluorescein is a typical ACQ molecule.[11] It is soluble in water but insoluble in most organic solvents. The diluted solution in water emits bright green luminescence, but the luminescence is gradually weakened by the addition of organic solvents miscible with water (e.g., acetone). When the fraction volume of acetone (f_a) is increased to 60 %, the ACQ effect becomes visually detectable (Figure 3). When the f_a is further increased, nano-aggregates of fluorescein are formed, and consequently the luminescence is completely quenching when the f_a is 70-90 %. The powders and crystals of fluorescein do not emit fluorescence as well as the aggregates.

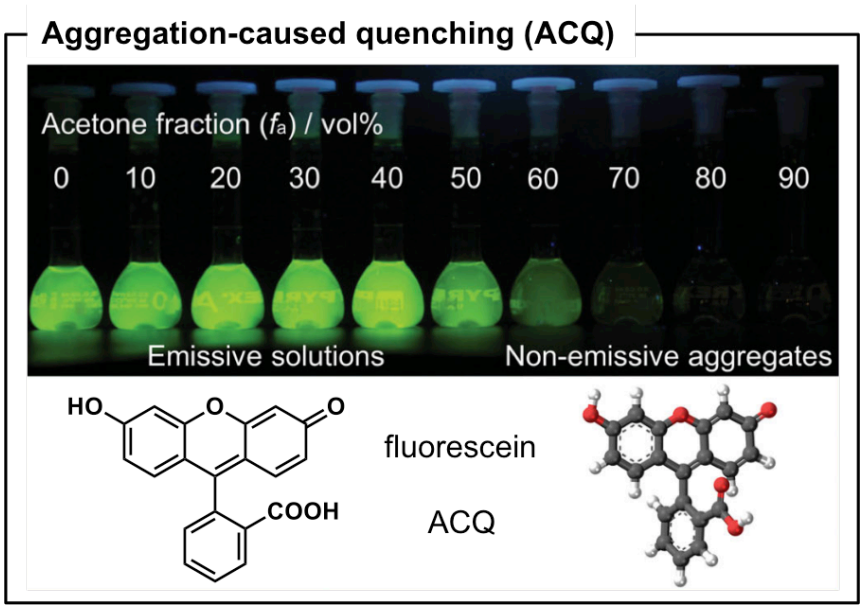

Figure 3. Aggregation-caused quenching (ACQ) behavior of fluorescein in water/acetone mixtures. Acetone fraction volume (f_a) is varied in the range of 0-90%.[11]

The ACQ effect prevents a variety of organic luminogens from the practical application.[12-14] For example, luminogens have been used to monitor bioactivity or ionic species in vivo. In this system, luminescence π-conjugated core is often tethered by polar functional units (e.g., carboxylic and sulfonic acids) to improve the hydrophilicity for solubilization, but the resulting water-soluble luminogens is prone to forming aggregates due to the invariant hydrophobicity of the π-conjugated cores. In addition, when the luminescence markers are left for a long period of time, the solvent evaporates and dried out, resulting in quenching.

3. Solutions against ACQ

Although it has been generally recognized that most luminogens having rigid π-conjugated systems suffer from the ACQ effect partially or completely, ACQ can be reduced depending on the aggregated styles. For example, *J*-aggregated crystals, which are head-to-tail type of molecular aggregate proposed by Jelly, show intense emission with rather high Φ_f in the solid state.[15] However, the luminogens forming *J*-aggregate are limited to only a few molecules such as cyanine.[16,17]

Other solutions against ACQ include wrapping luminescence molecules with bulky substituents to suppress the intermolecular stacking. For example, Nakanishi *et al.* synthesized anthracene-based molecules with long and branched alkyl chains (Figure 4).[18] The molecules became liquid state at room temperature but showed intense emission with high Φ_f even in the bulk state because bulky chains inhibited π-π stacking. This type of method is often used to obtain highly emissive luminogens,[19,20] however the substituents are too bulky to inhibit intermolecular electron transportation, limiting the application for optoelectronic devices. Therefore, it has been expected to develop molecules that show intense emission with high Φ_f in the aggregated state without any bulky substituents, regardless of the aggregated style.

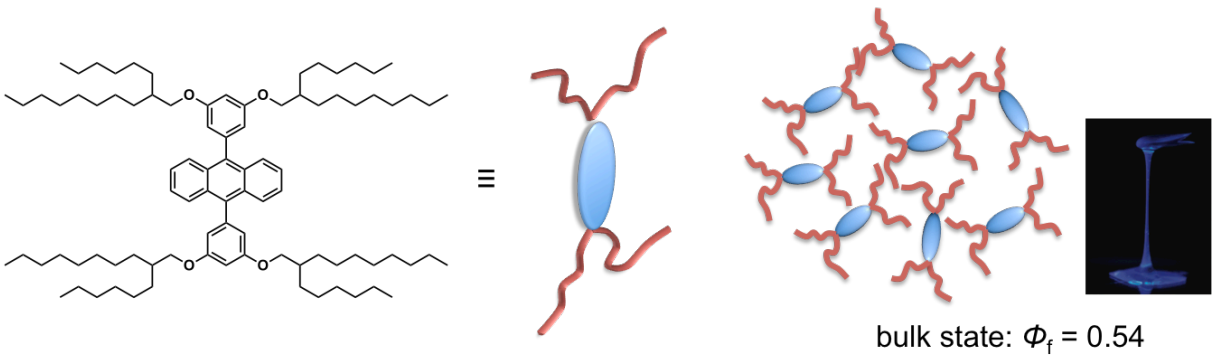

Figure 4. Chemical structure and schematic diagrams of anthracene-based molecule synthesized by Nakanishi *et al.*[18] The photograph of luminescence behavior and fluorescence quantum yield (Φ_f) in the bulk state are shown in this figure.

4. Aggregation-induced emission (AIE)

In 2001, Tang *et al.* discovered that 1-methyl-1,2,3,4,5-pentaphenylsilole exhibited unique luminescence behavior that was exactly opposite to ACQ.[21] For example, hexaphenylsilole (HPS), which is soluble in THF but insoluble in water, is non-emissive when the water volume fraction (f_w) is less than 70%. However, when the f_w reaches to 70 or 80%, the luminescence can be visually detected (Figure 5). This effect was named aggregation-induced emission (AIE) by Tang *et al*, and now is recognized as the common phenomena for seeking solid-state luminescence materials.

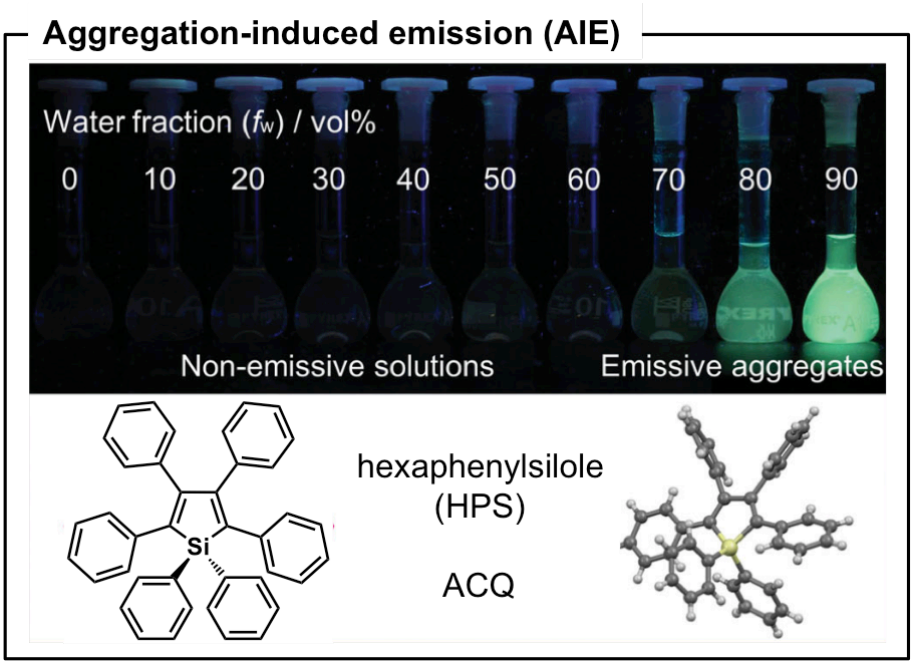

Figure 5. Aggregation-induced emission (AIE) behavior of hexaphenylsilole (HPS) in THF/water mixtures. Water volume fraction (f_w) is varied in the range of 0-90%.[11]

Since Tang *et al.* have discovered the AIE in the silole derivatives, many researchers focused on the applicability of the AIE effect and explored new AIE luminogens (AIEgens) other than silole derivatives.[22-28] One of the most well-studied AIEgens is tetraphenylethene (TPE) whose central C=C double bond is surrounded by four phenyl rings. TPE does not emit luminescence at all in the diluted solution, but emit bright blue or sky-blue luminescence in the aggregates, powders and crystals. TPE has simple structure and the backbone can be easily

synthesized by Mcmurry coupling from benzophenone, which allows us to synthesize various TPE derivatives. They have been used as various types of chemical sensors such as ions-, pH-, gases-, explosives-, peroxides-, and chirality- responsive sensors.[25] In addition to TPE, other AIEgens with various structures have been discovered one after another, which made us expect more and more research in the future.

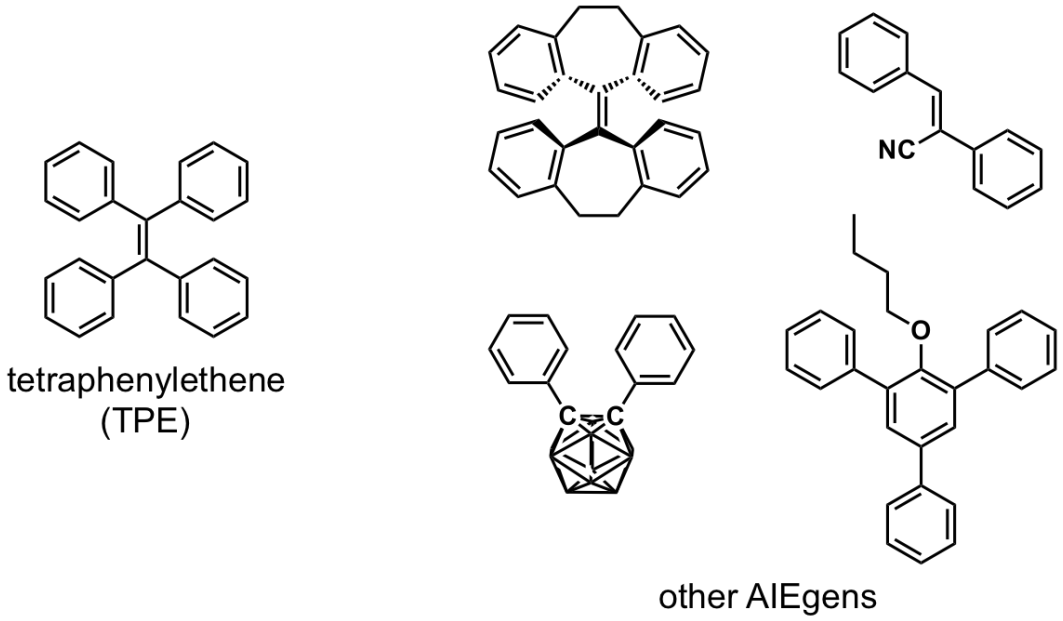

Figure 6. Chemical structures of tetraphenylethene (TPE) and other AIEgens.

5. AIE mechanism

To design new AIEgens and to control the AIE behavior, it is essential to obtain accurate understanding of AIE mechanism. Following the first report about AIE, Tang *et al.* initially suggested that restriction of intramolecular rotation (RIR) was the main cause of AIE effect.[29] That is, in the diluted solution, excited AIEgens spend energy on intramolecular rotation of rotators such as free phenyl rings, while, in the aggregated state, the nonradiative decay pathway by the intramolecular rotation was restricted, resulted in AIE (Figure 7).

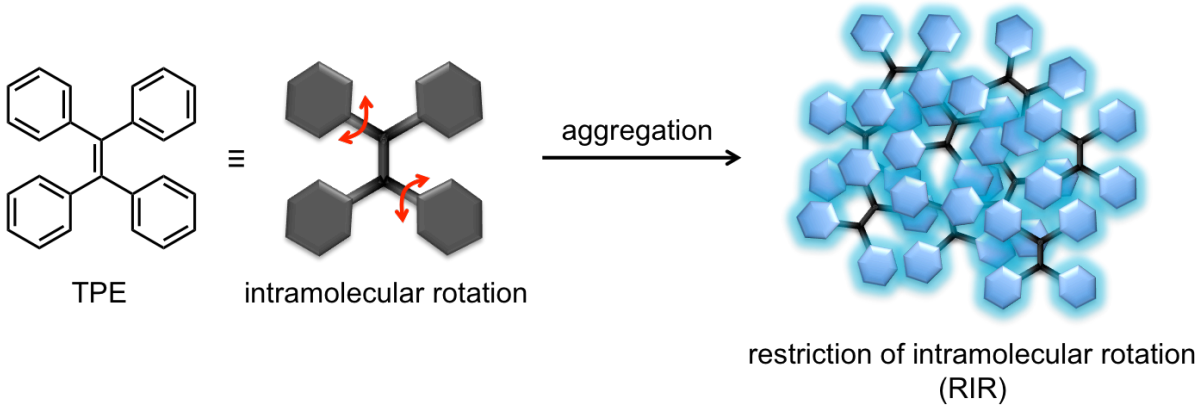

Figure 7. Schematic diagrams of restriction of intramolecular rotation (RIR) of tetraphenylethene (TPE) in the aggregated state.

Involvement of RIR process in the AIE behavior was confirmed by a variety of stimuli-responsive studies. For example, Tang *et al.* measured photoluminescence (PL) intensity of HPS derivative in glycerol/methanol mixture.[30] Viscosity of the mixture increased by addition of glycerol because the viscosity of glycerol (934 cP at 25 °C) was much higher than that of methanol (0.544 cP). When the glycerol fraction increased, the PL intensity linearly increased in the region where HPS derivative can be dissolved, indicating that the fluorescence of AIEgens was induced by high viscosity. In addition, Tang *et al.* revealed that the fluorescence was enhanced in low temperature by using variable-temperature NMR and fluorescence spectroscopy on a HPS derivative.[30] Furthermore, it was reported that the fluorescence was also enhanced under high pressure.[31] These results supported that RIR following aggregation, rather than aggregation itself, was important for AIE.

Considering RIR process in the AIE behavior, researchers have focused on induction of the strong luminescence of AIEgens without aggregation. Cyclization-induced emission (CIE), reported by Shinkai *et al.*, is one of the most noteworthy researches. In CIE system, when TPE derivative having zinc dipicolylamine groups interacts with carboxylic acid in a homogeneous buffer solution, it become emissive.[32] Wu and coworkers also reported CIE-like behavior, in which bisurea-tethering TPE showed intense luminescence under the presence of anions in a homogeneous solution.[33] Furthermore, Kokado *et al.* made network polymers using AIEgens as a crosslinker.[34,35] In network polymers, AIEgens emit strong luminescence even in the quite low concentration, but the luminescence was quenched as the polymer swelled.

Above examples seem to support the RIR process, but some AIEgens do not have rotator such as free phenyl rings, and the RIR process is not applicable to such AIEgens. Therefore, more broadly defined words restriction of intramolecular vibration (RIV) and restriction of intramolecular motion (RIM) have come to be used.

5. Survey of this thesis

As reviewed in the previous sections, AIE has emerged as a new class of photoluminescence behavior and the mechanism has been intensely studied. The previous studies suggested the molecular motion such as intramolecular rotation and vibration in the excited state related to the AIE behavior. However I had doubt about the mechanism because such small molecular motions (thermal perturbations) could occur even in the aggregated state, and recent calculations suggested the importance of photoprocess in the excited state for the AIE. Thus I proposed that "large structural change in the excited state" that should be restricted in the aggregated or solid state played crucial role for AIE behavior. To verify this hypothesis, in this thesis, I explored the large structural change of AIE molecules in the excited state by combination of various experimental and computational methods. This thesis was composed of 6 chapters including general introduction and conclusion in total.

In Chapter II, I synthesized liquid aggregation-induced emission (AIE) molecules in order to liberate the AIE molecules from the intramolecular interaction that restricted molecular motions. Liquefaction of AIE molecule was accomplished by covalently attaching long and branched alkyl chains onto tetraphenylethene TPE. The linkage between TPE and alkyl chains definitely affected the thermal property, especially, ester-linked liquid TPE showed solid-liquid phase transition at around room temperature. The liquid TPE had higher fluorescence quantum yield than solid TPE despite the reduced intramolecular interactions, which indicated that small molecular motions (thermal pertubations) such as intramolecular rotation was irrelevant to the AIE behavior. Furthermore, the liquid TPE could homogeneously dissolved another organic fluorophore, enabling to finely tune the emission color.

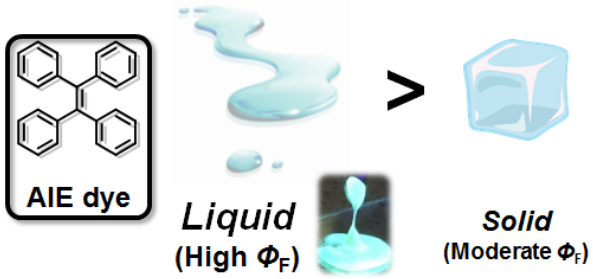

Chart 1

In Chapter III, I investigated the large structural change of TPE in the excited state by experimental observations and theoretical computations, in order to obtain deep insight into the nonradiative decay process of AIE molecules. *Cis-trans* isomers of simple TPE derivatives were obtained by carefully purifications with chromatography and recrystallization. Photoirradiation to the isomers in the diluted solutions resulted in the equilibrium state with isomeric ratio of approximately 1:1 via rapid isomerization. In contrast, photoisomerization was inhibited in the solid state. Theoretical computations could explain the experimental results. In the diluted solution, the rotation of the phenyl ring is activated by photoexcitation to achieve the planar conformation of the phenyl rings and C=C double bond, which relax the excited state, consequently leading to the nonradiative decay. In the crystal, solid and aggregated states, the C=C bond twist is severely restricted by the surrounding molecules, thereby resulting in strong emission.

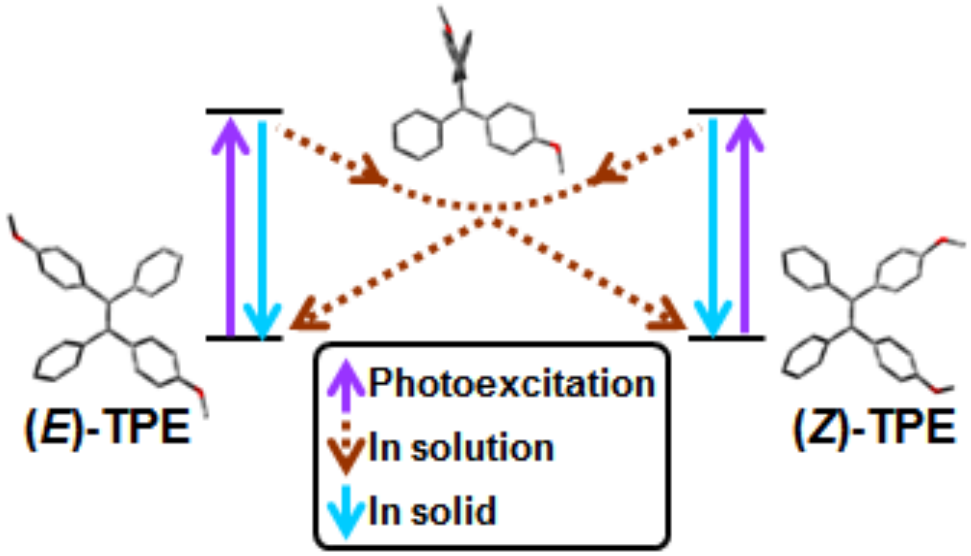

Chart 2

In Chapter IV, the I synthesized a series of TPE macrocycles having covalent oligoethylene glycol linkage between vicinal phenyl rings with various chain lengths and substituent positions. TPE macrocycles were synthesized at low concentration by slowly dripping the precursor into the reaction mixtures over several hours. They exhibited different luminescence properties depending on the chain lengths, and the substituent positions. The derivatives with shorter chains and trans isomers linked at the *o*-position showed fluorescence in the diluted solution, while the others showed typical AIE behavior similar to non-substituted TPE. From the theoretical computations for these molecules in the excited state, TPE macrocycles showing strong emission in the diluted solution exhibited smaller difference of the dihedral angle around the central C=C bond between in the ground and excited state, while showing no emission in the solution state exhibited larger difference.

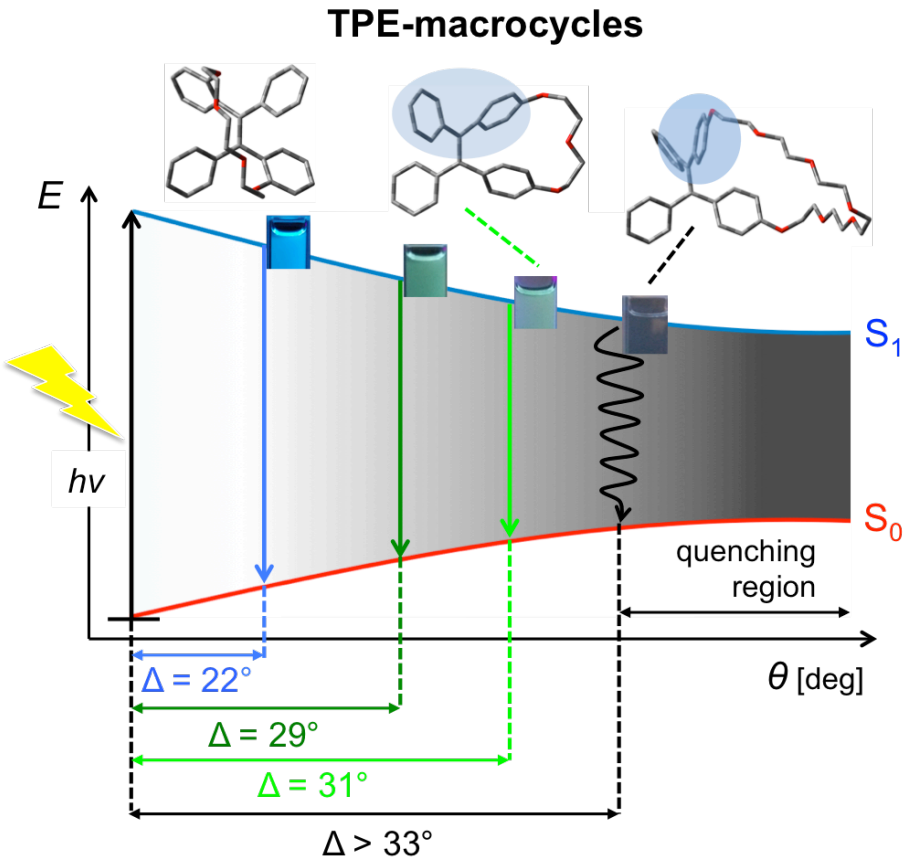

Chart 3

In Chapter V, I investigated the large structural change in the excited state of phosphines that was involved with the AIE behavior. Phosphines having three different polycyclic aromatic hydrocarbons (PAHs) were synthesized by stepwise Grignard reactions. In the diluted solution, the fluorescence intensity of the PAH-containing phosphines definitely decreased compared to the correspond PAHs, like typical AIE behavior, and at the same tome moreover, the chiral phosphines exhibited racemization easily by photoexcitation. According to the theoretical calculations, the photoplanarization of phosphines promotes nonradiative decay from the excited state, resulted in photoracemization in the diluted solution. The photoplanarization was not specific to PAH-containing phosphines, but was also observed in common phosphines such as PH_3, PMe_3, and PPh_3.

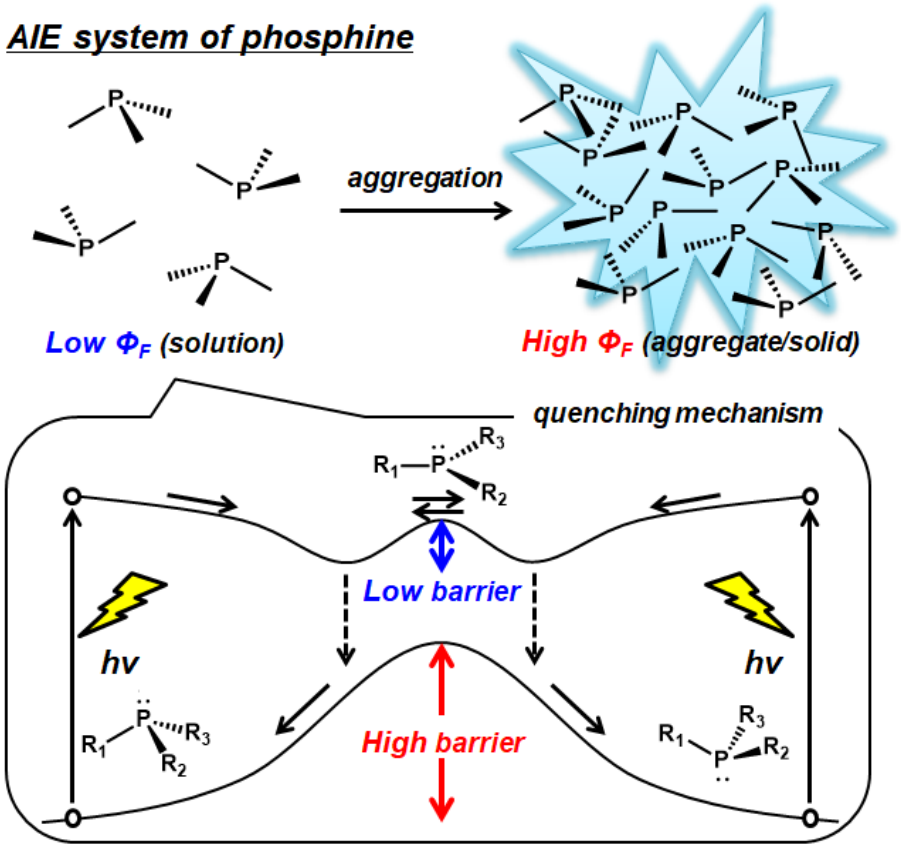

Chart 4

Relationships between Chapter II-V were summarized in Chart 5. Chapter III was motivated by the results of Chapter II. From the result of Chapter III that AIE molecules showed stronger luminescence in the bulk liquid state than in the solid state, I supposed that small motions (thermal perturbations) that can occur even in the liquid phase were not involved in the AIE mechanism, but rather the large structural change such as C=C bond twist in the excited state related closely to the AIE mechanism. The assumption was confirmed in Chapter III, following by Chapter IV. The result of Chapter IV that crosslinking styles of phenyl rings of TPE affected the photophysical properties supported my hypothesis. In Chapter II-IV, I focused on the AIE behavior of TPE, and I extended my hypothesis to phosphine in Chapter V.

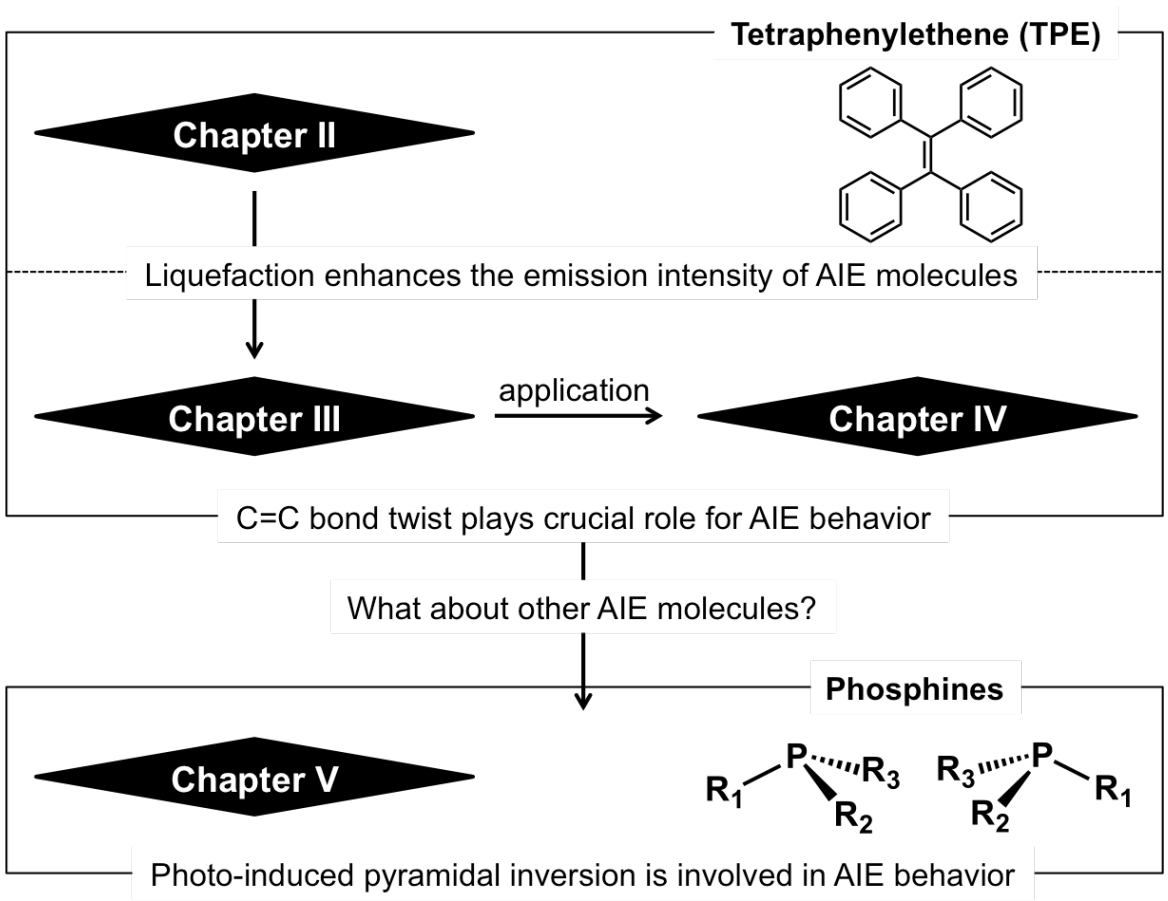

Chart 5

References

[1] E. Smulders, W. von Rybinski, E. Sung, W. Rähse, J. Steber, F. Wiebel, A. Nordskog, *Ulmann's Encyclopedia of Industrial Chemistry*, **2007**,

[2] L. Yuan, W. Y. Lin, K. B. Zheng, L. W. He, W. M. Huang, *Chem. Soc. Rev.* **2013**, *42*, 622–661.

[3] Y. M. Yang, Q. Zhao, W. Feng, F. Y. Li, *Chem. Rev.* **2013**, *113*, 192–270.

[4] E. Azuma, N. Nakamura, K. Kuramochi, T. Sasamori, N. Tokitoh, I. Sagami, K. Tsubaki, *J. Org. Chem.* **2012**, *77*, 3492-3500.

[5] Z. Lei, X. Li, X. Luo, H. He, J. Zheng, X. Qian, Y. Yang, *Angew. Chem. Int. Edit.* **2017**, *56*, 2979.

[6] I. B. Berlman, Handbook of Fluorescence Spectra of Aromatic Molecules. *Academic Press*. *N. Y*. **1971**.

[7] S. W. Thomas, G. D. Joly, T. M. Swager, *Chem. Rev.* **2007**, *107*, 1339.

[8] A. R. Murphy, J. M. J. Frechet, *Chem. Rev.* **2007**, *107*, 1066.

[9] Th, Foster, K. Z. Kasper, *Phys. Chem. N. F.* **1954**i, *1*, 275.

[10] J. B. Birks, *Photophysics of Aromatic Molecules*, Wiley, London, **1970**.

[11] J. Mei, Y. Hong, J. W. Y. Lam, A. Qin, Y. Tang, B. Z. Tang, *Adv. Mater.* **2014**, *26*, 5429–5479.

[12] R. B. Thompson, *Fluorescence Sensors and Biosensors*, CRC, Boca Raton **2006**.

[13] C. D. Geddes, J. R. Lakopwicz, *Advanced Concepts in Fluorescence Sensing*, Springer, Norwell **2005**.

[14] E. A. Jares-Erijman, T. M. Jovin, *Nat. Biotechnol.* **2003**, *21*, 1387.

[15] F. Wurthner, T. E. Kaiser, C. R. Saha-Moller, *Angew. Chem., Int. Ed.* **2011**, *50*, 3376–3410.

[16] K. Cai, J. J. Xie, D. H. Zhao, *J. Am. Chem. Soc.* **2014**, *136*, 28–31.

[17] F. C. Spano, *Acc. Chem. Res.* **2010**, *43*, 429–439.

[18] S. S. Babu, M. J. Hollamby, J. Aimi, H. Ozawa, N. Shirahata, A. Saeki, S. Seki, K. Kobayashi, K. Hagiwara, M. Yoshizawa, H. Möhwald and T. Nakanishi, *Nat. Commun*, **2013**, *4,* 1969.

[19] G. Barbarella, L. Favaretto, G. Sotgiu, M Zambianchi, A. Bongini, C. Arbizzani, M. Mastragostino, M. Anni, G. Gigli, R. Cingolani, *J. Am. Chem. Soc.* **2000**, *122*, 11971–11978.

[20] A. Iida, S. Yamaguchi, *Chem. Commun.* **2009**, 21, 3002–3004.

[21] J. Luo, Z. Xie, J. W. Y. Lam, L. Cheng, B. Z. Tang, H. Chen, C. Qiu, H. S. Kwok, X.

Zhan, Y. Liu, D. Zhu, *Chem. Commun.* **2001**, 1740

[22] Y. Hong, J. W. Y. Lam, B. Z. Tang, *Chem. Commun.* **2009**, 4332–4353.

[23] Y. Hong, J. W. Y. Lam, B. Z. Tang, *Chem. Soc. Rev.* **2011**, 40, 5361–5388.

[24] J. Mei, Y. Hong, J. W. Y. Lam, A. Qin, Y, Tang, B. Z. Tang, *Adv. Mater.* **2014**, *26*, 5429–5479.

[25] J. Mei, N. L. C. Leung, R. T. K. Kwok, J. W. Y. Lam, B. Z. Tang, *Chem. Rev.* **2015**, *115*, 11718–11940.

[26] H. Wang, E. Zhao, J. W. Y. Lam, B. Z. Tang, *Mater. Today* **2015**, *18*, 365–377.

[27] G. Feng, R. T. K. Kwok, B. Z. Tang, B. Liu, *Appl. Phys. Rev.* **2017**, *4*, 021307.

[28] Z. He, C. Ke, B. Z. Tang, *ACS Omega* **2018**, *3*, 3267–3277.

[29] H. Tong, Y. Hong, Y. Dong, M. Haußler, J. W. Y. Lam, Z. Li, Z. Guo, Z. Guo, B. Z. Tang, *Chem. Commun.* **2006**, 3705–3707.

[30] J. Chen, C. C. W. Law, J. W. Y. Lam, Y. Dong, S. M. F. Lo, I. D. Williams, D. Zhu, B. Z. Tang, *Chem. Mater.* **2003**, *15*, 1535−1546.

[31] X. Fan, J. Sun, F. Wang, Z. Chu, P. Wang, Y. Dong, R. Hu, B. Z. Tang, D. Zou, *Chem. Commun.* **2008**, 2989−2991.

[32] T. Noguchi, B. Roy, D. Yoshihara, Y. Tsuchiya, T. Yamamoto, S. Shinkai, *Chem. Eur. J.* **2014**, *20*, 381−384.

[33] J. Zhao, D. Yang, Y. Zhao, X.-J. Yang, Y.-Y. Wang, B. Wu, *Angew. Chem. Int. Ed.* **2014**, *53*, 6632–6636.

[34] R. Taniguchi, T. Yamada, K. Sada, K. Kokado, *Macromolecules,* **2014**, *47*, 6382–6388.

[35] K. Kokado, R. Taniguchi, K. Sada, *J. Mater. Chem. C,* **2015**, *3*, 8504–8509.

Chapter II

The effect of liquefaction to AIE behavior

Chapter II

The effect of liquefaction to AIE behavior

Abstract: This chapter describes the synthesis of liquid aggregation-induced emission (AIE) molecules to liberate the AIE molecules from the intramolecular interaction that restricted molecular motions. Liquefaction of AIE molecule was accomplished by covalently attaching long and branched alkyl chains onto tetraphenylethene TPE. The linkage between TPE and alkyl chains definitely affected the thermal property, especially, ester-linked liquid TPE showed solid-liquid phase transition at around room temperature. The obtained liquid TPE had higher fluorescence quantum yield than solid TPE despite the reduced intramolecular interactions, which indicated that small molecular motions such as intramolecular rotation and vibration irrelevant to the AIE behavior. Furthermore, the liquid TPE could homogeneously dissolved another organic fluorophore, enabling to finely tune the emission color.

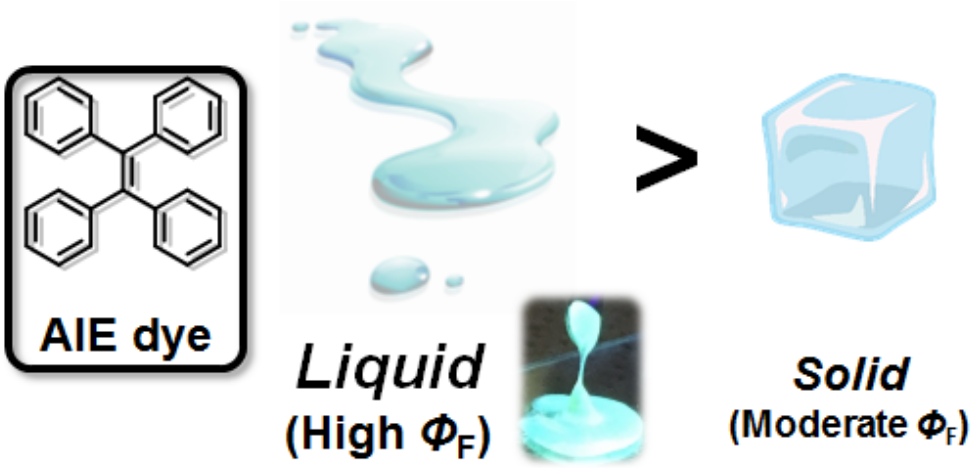

Introduction

The molecules with a robust π-conjugated backbone have been used for optical brighteners, luminescent markers, and clinical diagnostic reagents, because they exhibit strong luminescence in visible light region. In these days, luminescent molecules have been applied for optoelectronic devices such as organic light emitting diode (OLED), thereby development of luminogens that retain strong luminescence even in the solid state is required. However, the conventional luminogens (*e.g.* perylene, fluorescein) become non-emissive in the solid state because of the strong intramolecular π-π stacking. That concentration-dependent quenching behavior is called aggregation caused quenching (ACQ), has prevented its application for OLED.

Recently, Nakanishi *et al.* reported that liquefaction of conventional luminogens by attaching long alkyl chains was efficient method to diminish ACQ effect.[6,7] In this system, steric repulsion of bulky substituents and flexibility originated from liquid nature prevents intramolecular π-π stacking, resulting in the strong luminescence in the bulk state. The liquefaction method has attracted attention, because it is simple and applicable to many luminogens. On another front, aggregation-induced emission (AIE) molecules also have attracted attention because AIE is opposite effect to ACQ; AIE molecules are non-emissive in the solution state but it become emissive in high concentrated state such as aggregated, solid, bulk state.[1-5]

AIE mechanism has attracted attention to develop new AIE molecules and to control the AIE behavior. Restriction of intramolecular rotation (RIR) is initially proposed mechanism to explain the AIE behavior.[8] For example, tetraphenylethene (TPE) is a typical AIE molecule, and it has four phenyl rings around central C=C bond. In the diluted solution, the phenyl rings act as rotators and dissipate excited energy, while, in the aggregated state, the intramolecular motion of rotators are restricted which resulted in strong luminescence.[9] This mechanism has been supported for a long time by experimental studies, but recently the AIE behavior has been explored by excited state calculations. According to those calculations, AIE molecules underwent large structural change rather than intramolecular rotation in the excited state.[10]

In the first place, I had doubt the RIR mechanism because such a small molecular motion can occur even in the aggregated or solid state. Therefore, to investigate whether RIR process is involved in the AIE behavior, I adapted liquefaction method invented by Nakanishi *et al.* Since intramolecular interactions decrease in the liquid phase compared to in the solid phase, liquefaction will liberate AIE molecules from the RIR. Therefore, if the RIR process plays crucial role for the AIE behavior, liquid AIE molecules would become non-emissive. In this chapter, I attempted liquefaction of TPE by attaching long and branched alkyl chains, and investigated the ACQ effect observed in AIE molecules.

Results and Discussion

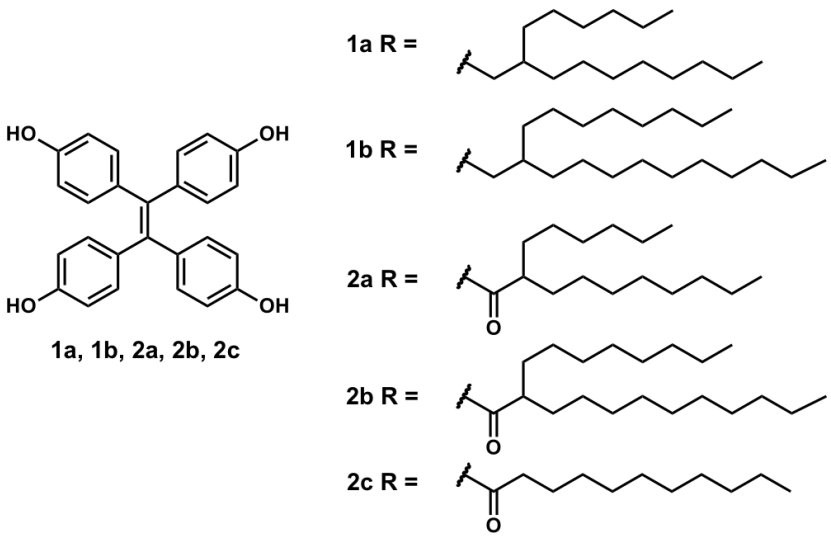

Figure 1. Chemical structures of AIE-active tetraphenylethene (TPE) derivatives.

Initially TPE derivatives with long alkyl chains were synthesized by Williamson ether reaction for **1a** and **1b**, and esterification condensation for **2a-c** (Figure 1). They were identified by ^{1}H NMR, ^{13}C NMR and high-resolution mass spectroscopy (HRMS). The molecules **1a**, **1b**, **2a**, and **2b** having branched alkyl chains were liquid at room temperature, while **2c** having straight alkyl chain was solid, which meant branched alkyl chains significantly reduce intermolecular interactions.

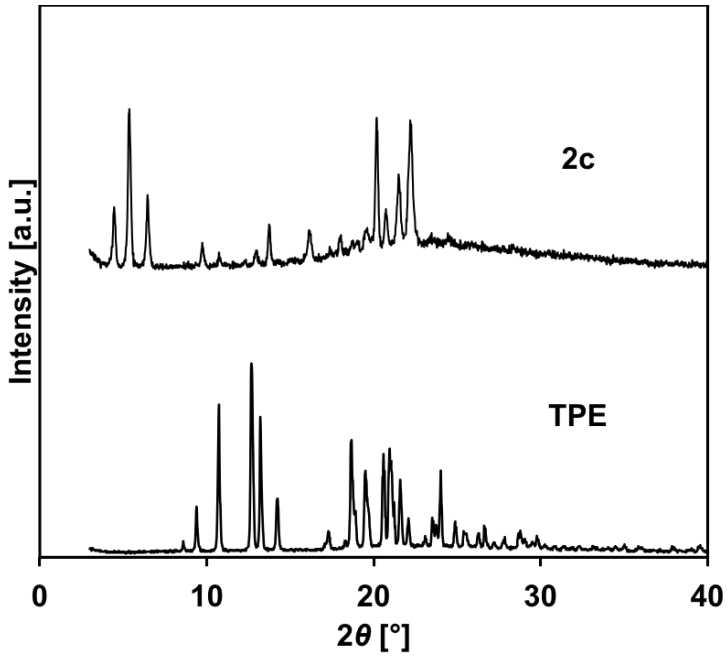

Figure 2. X-ray diffraction (XRD) patterns of **2c** and **TPE**.

Among the derivatives, X-ray diffraction (XRD) pattern of **2c** was different from that of TPE (Figure 2). In partially, the peaks at the lower 2θ were formed due to the long alkyl chains. Viscosity measurements revealed that liquid TPEs had high viscosities of around 6000 cP, which was good agreement with the viscosity of anthracene liquids previously reported.

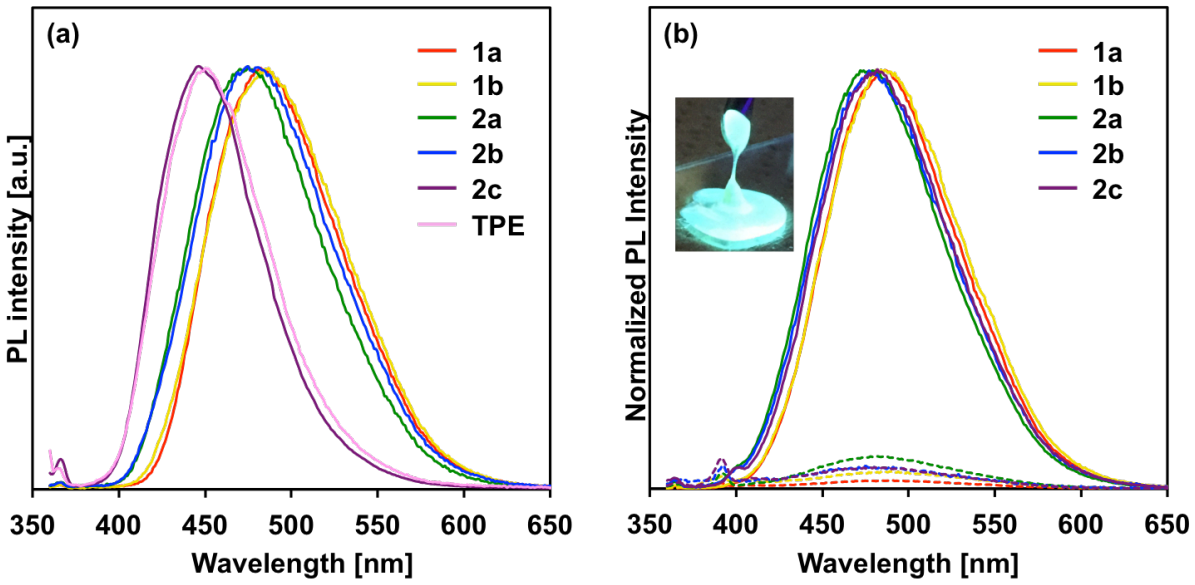

Figure 3. (a) Photoluminescence (PL) spectra of the TPE derivatives **1a**, **1b** and **2a-c** in the dissolved state in THF (dashed line) and the aggregated state (solid line) in the mixed solvent of THF/H_2O (v/v = 1/99). (b) PL spectra of the TPE derivatives and TPE in the bulk state (λ_{ex} = 350 nm). Inset shows a photograph of **2a**.

These molecules exhibited typical AIE behavior. They were non-emissive in the THF solution (absolute fluorescence quantum yield Φ_F = 0.01 for **2a**), and were highly emissive in the aggregated state in the mixture of THF and H_2O (v/v = 1/99) (Figure 3a). On the other hand, in the condensed phase, they were also emissive (Figure 3b). The emission maximum (λ_{em}) of solid molecule (**2c**) was observed at around 450 nm, similar to that of mother compound TPE, while the λ_{em} of liquid molecules (**1a**, **1b**, **2a**, and **2b**) were observed at round 480-490 nm. The red shift in liquid molecules was attributed to the extended effective conjugated length relaxation process derived from the relaxation process in the excited state, suggesting that the restriction of intramolecular motion was relaxed in the liquid phase.

Table 1. Summary of photophysical properties of TPE derivatives in the bulk state.

Compound	State at r.t.	λ_{em} [nm]	Φ_f	τ [ns]	k_r [s^{-1}]	k_{nr} [s^{-1}]
1a	Liquid	482	0.93	3.19	0.29	0.022
1b	Liquid	487	0.77	3.40	0.23	0.068
2a	Liquid[a]	475	0.67	4.31	0.16	0.077
2b	Liquid[a]	475	0.65	3.86	0.17	0.091
2c	Solid	446	0.46	1.77	0.26	0.31
TPE	Solid	448	0.49	1.37	0.36	0.37

[a] Supercooling liquid as revealed by DSC measurement (*vide infra*)

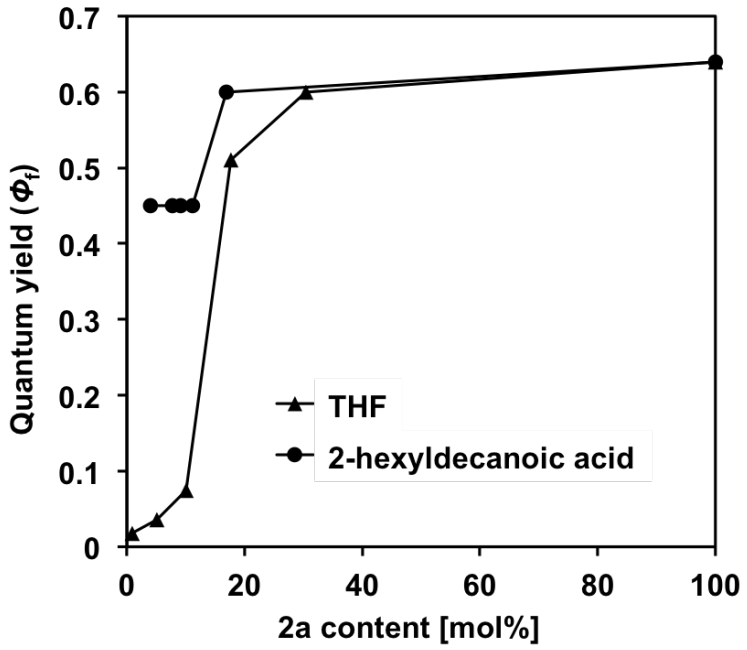

Figure 4. Photoluminescence quantum yield (Φ_F) of **2a** in THF and 2-hexyldecanoic acid with various molar ratio.

The photophysical properties of these molecules in the bulk state at room temperature were summarized in Table 1. The ether-linked liquid molecules **1a** and **1b** exhibited the highest Φ_f of 0.93 and 0.77, respectively, and ester-linked liquid molecules **2a** and **2b** exhibited the second highest Φ_f of 0.67 and 0.65, respectively. The solid molecules **2c** exhibited a moderate Φ_f of 0.46, which was similar value to that of **TPE**. Thus, the liquid molecules (**1a**, **1b**, **2a**, and **2b**) presented higher Φ_f despite their liquid state, probably because of their high viscosity.

To confirm the effect of viscosity, Φ_f of **2a** was measured in the mixtures of low-viscosity solvents, such as THF (0.46 cP at 25 °C) or 2-hexyldecanoic acid (33.7 cP at 25 °C) (Figure 4). After the progressive dilution with THF, Φ_f of **2a** drastically decreased at 20 mol% of **2a**, and eventually to almost 0. While, when 2-hexyldecanoic acid was used, Φ_f of **2a** was decreased to a moderate Φ_F of 0.45 at 20 mol% of **2a**, and further dilution did not change the Φ_F, meant that the viscosity provide significant effect to Φ_F of AIE molecules.

The fluorescence lifetime measurement of these molecules revealed that the first-order decay, and the time constant (τ) was larger for the liquid molecules (**1a**, **1b**, **2a**, and **2b**; 3-4 ns^{-1}) than that for the solid molecule (**2c**; <2 ns). The rate constants for the radiative and nonradiative processes (k_r and k_{nr}) were calculated from Φ_F and τ. According to the calculations, k_r were almost the same in both liquid and solid molecules, but k_{nr} of liquid molecules (<0.1 ns^{-1}) were smaller than that of solid molecules (> 0.3 ns^{-1}).

Judging from these photophysical observations, I can conclude the following two points. (1) The molecular state (liquid or solid) is not related to the Φ_f due to the high viscosity of liquid molecules. (2) The inherent amorphous nature of liquid molecules provide higher Φ_f (derived from low k_{nr}) and red-shifted λ_{em} compared to those of solid molecules. The lower Φ_f of **2a** and **2b** compared to those of **1a** and **1b** were probably due to the intermolecular interaction caused by the hydrogen bonding in ester moieties, which was confirmed by X-ray and thermal analysis (*vide infra*)

Table 2. Summary of crystallographic data of **1me** and **2me**.

Identification code	**1me**	**2me**
Empirical formula	$C_{30}H_{28}O_4$	$C_{34}H_{28}O_8$
Formula weight	452.52	564.56
Temperature	153(2) K	93(2) K
Crystal system, space group	monoclinic, $P2_1/n$	monoclinic, $P2_1/c$
Unit cell dimensions	a = 9.6317(3) Å α = 90 °	a = 10.4605(8) Å α = 90 °
	b = 15.5277(6) Å β = 92.4928(12) °	b = 20.3913(13) Å β = 102.144(2) °
	c = 16.0905(5) Å γ = 90 °	c = 14.1238(8) Å γ = 90 °
Volume	2404.19(14) $Å^3$	2945.2(3) Å^3
Z, Calculated density	4, 1.250 g/cm^3	4, 1.273 g/cm^3
Absorption coefficient	0.082 mm^{-1}	0.091 mm^{-1}
F(000)	960	1184
Crystal size	0.50 × 0.50 × 0.20 mm	0.40 × 0.40 × 0.40 mm
Theta range for data collection	3.37 to 27.46 °	3.12 to 27.48 °
Limiting indices	-12<=*h*<=12, -20<=*k*<=20, -20<=*l*<=20	-7<=*h*<=13, -26<=*k*<=26, -17<=*l*<=17
Reflections collected / unique	38180 / 5479 [R_{int} = 0.0369]	13829 / 6223 [R_{int} = 0.0512]
Completeness to theta = 27.46	99.60%	92.10%
Max. and min. transmission	0.9838 and 0.9602	0.9646 and 0.9646
Refinement method	Full-matrix least-squares on F^2	Full-matrix least-squares on F^2
Data / restraints / parameters	5479 / 0 / 311	6223 / 0 / 383
Goodness-of-fit on F^2	1.055	1.078
Final *R* indices [I>2sigma(I)]	R_1 = 0.0510, wR_2 = 0.1073	R_1 = 0.0626, wR_2 = 0.1630
R indices (all data)	R_1 = 0.0630, wR_2 = 0.1130	R_1 = 0.1279, wR_2 = 0.2300
Largest diff. peak and hole	0.259 and -0.200 e. $Å^{-3}$	0.337 and -0.339 e. $Å^{-3}$

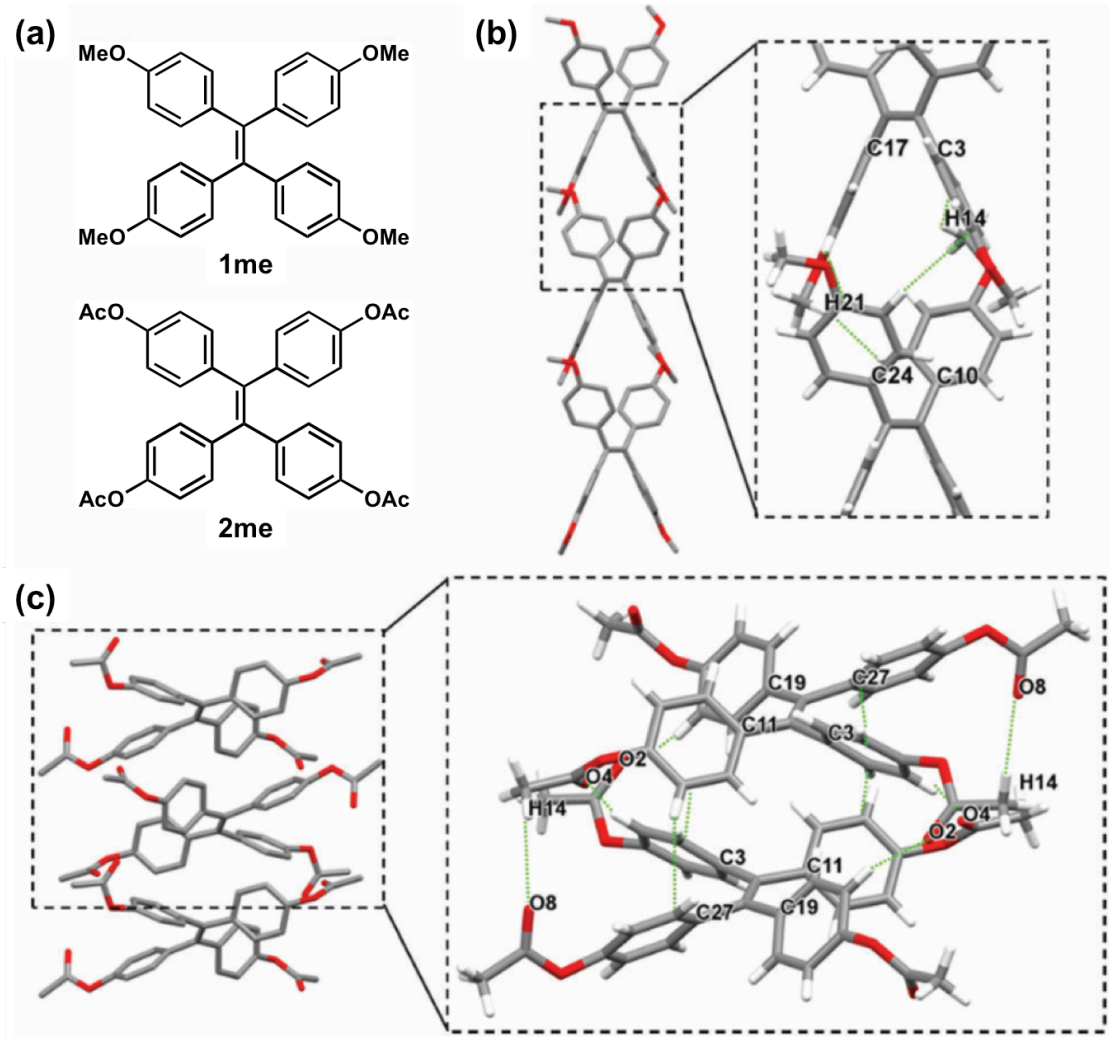

Figure 5. (a) Chemical structures of **1me** and **2me**. Crystal packing of (b) **1me** and (c) **2me** viewed from the b axis. Hydrogen atoms are omitted in the big-picture view for clarity. For phenyl rings In the magnified view, the smallest label for carbon atom in one phenyl ring is noted, which is the carbon atom linked with the central C=C bond. The light green dotted lines represent short contacts less than the sum of van der Waals radii.

To compare the effect of the crystalline and amorphous states of the AIE molecules, single crystal X-ray analysis was performed using model compounds **1me** and **2me** with different linkage styles of alkyl chains (Figure 5a). Single crystals of **1me** and **2me** were obtained by simple recrystallization process. Both crystals had a monoclinic lattice system with $P2_1/n$ and $P2_1/c$ space groups, respectively. The molecular packing styles were largely different (Figure 5b and 5c). **1me** had two T-stacking type π-π interactions (C3-C8 and C24-C29, C17-C22 and C24-C29) and two interactions between phenyl ring and hydrogen atom (C10-C15 and H21, C3-C8 and H14) on the methoxy group with *ca.* 2.8 Å were observed in one-dimensional **1me** column. As a result, lateral stacking in the bay region and vertical stacking of the central C=C bond were observed as shown in Figure 5b. On the other hand, **2me** had three T-stacking type π-π interactions (C3-C8 and C11-C16, C11-C16 and C27-C32, C19-C24 and C27–C32), indicating a one-dimensional **2me** column. In addition, three carbonyl oxygen atoms interacted with phenyl rings (O2 and C19-C24, O4 and C3-C8, O6 and C27-C32), and the other oxygen interacted with hydrogen atom on the acetoxy group (O8 and H14) in the one-dimensional column. As the result, face-to-face stacking of TPE, out-of-plane of and perpendicular to the central C=C bond, was observed as shown in Figure 5c. The highly polar carbonyl groups in **2me** are responsible for the tightly packing structure. Indeed, the crystal density of **2me** (1273 gcm^{-3}) was *ca*. 2 % larger than the crystal density of **1me** (1250 gcm^{-3}).

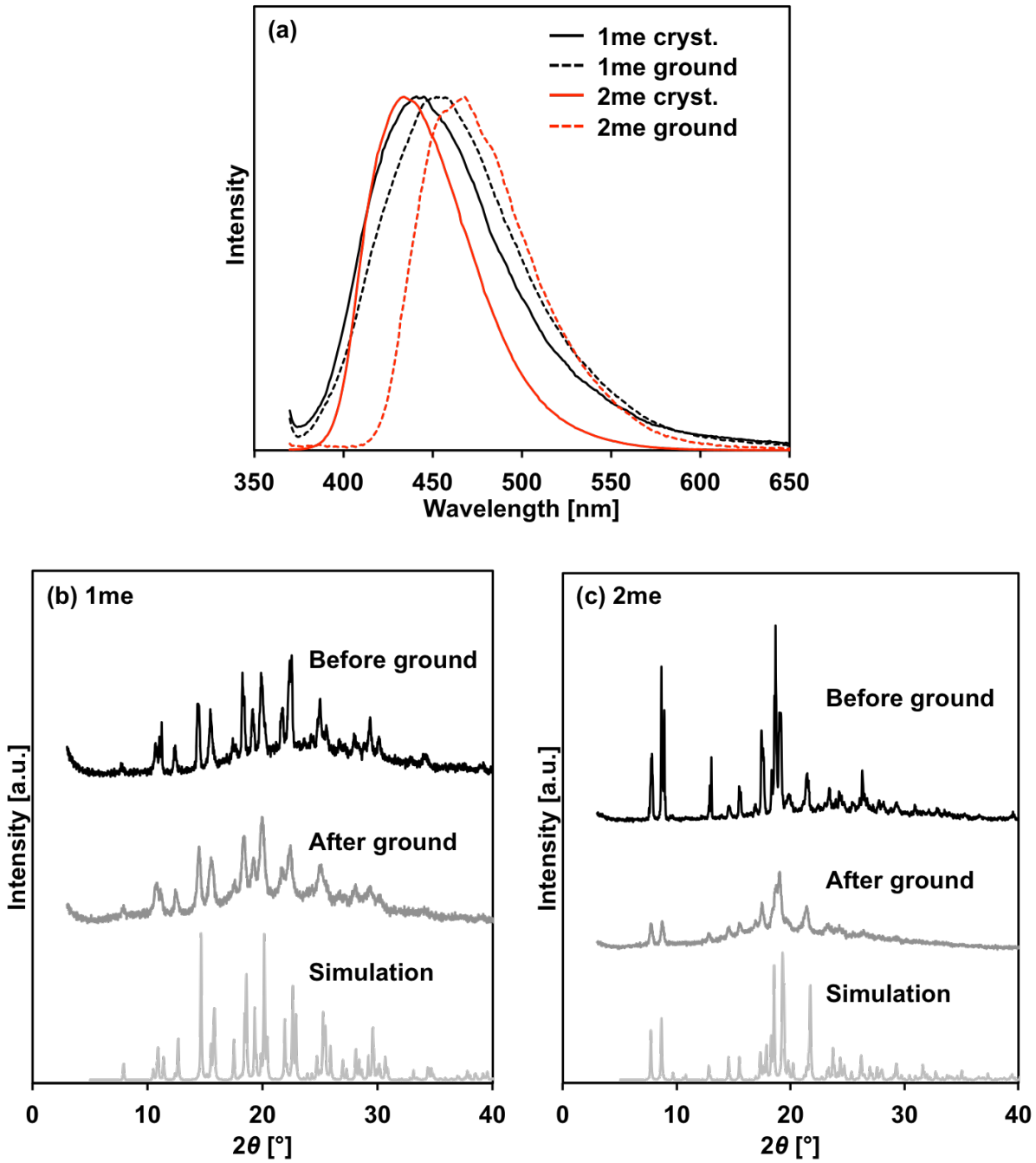

Figure 6. (a) Photoluminescence spectra of **1me** (black) and **2me** (red) in crystalline state (solid line) and ground state (dashed line). XRD patterns of (b) **1me** and (c) **2me** before ground, after ground, and simulated pattern from single crystal diffraction.

The change of molecular packing related to their mechanochromic properties. Grinding of the both crystals induced bathochromic emission shift (Figure 6a). Notably, densely packed **2me** showed a large shift of 36 nm from 435 nm to 471 nm by grinding, whereas the gently packed showed a small shift of 13 nm from 442 nm to 455 nm. The crystallinity of both crystals was degraded by grinding according to the XRD patterns before and after grinding (Figure 6b and 6c). Although the reason for the difference of λ_{em} after grinding is not clear at this moment, the difference in the amount of bathochromic shift should be caused by the change of molecular packing.

From these findings about **1me** and **2me**, following two implications were suggested. (1) the crystalline or less crystalline state can provide a significant effect on the photophysical properties. (2) The type of linkage with the alkyl chain can also affect the photophysical properties as well as the thermal properties (*vide infra*).

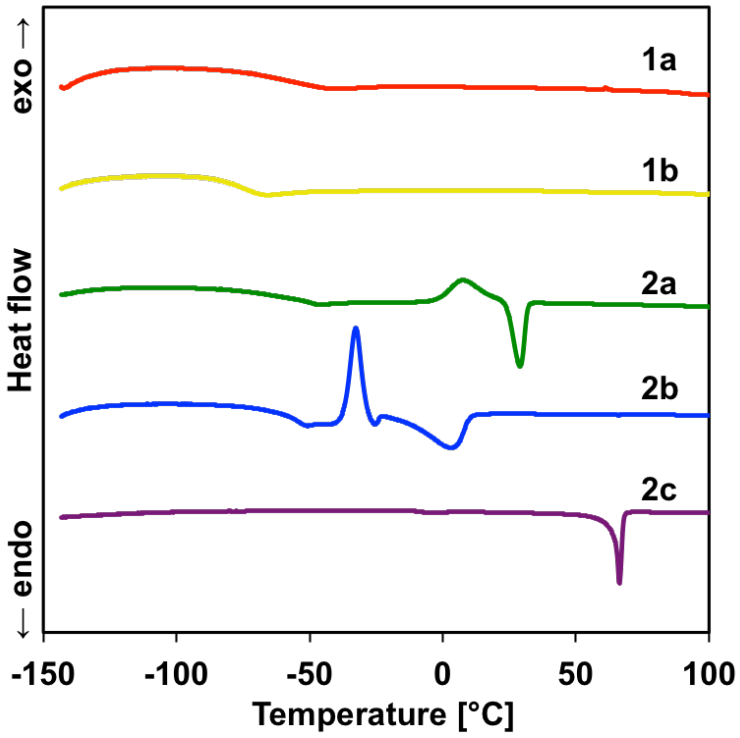

Figure 7. Differential scanning calorimetry (DSC) chart of the TPE derivatives.

Table 3. Summary of thermal properties, measured by DSC under a nitrogen atmosphere. Heating rate was 10 °C min^{-1}.

Compound	T_g [°C]	T_c [°C]	T_m [°C]
1a	−54.1	n.a.	n.a.
1b	−76.8	n.a.	n.a.
2a	−64.0	6.2	29.7
2b	−60.2	−32.7	3.2
2c	n.a.	n.a.	63.8

Their thermal properties were analyzed by differential scanning calorimetry (DSC) (Figure 7 and Table 3). During the heating process, the ether-linked liquid **1a** and **1b** simply showed a glass transition temperature (T_g) at −54.1 °C and −78.8 °C, respectively, while the ester-linked liquid **2a** and **2b** showed crystallization and melting point (T_c and T_m) in addition to T_g. The T_c and T_m were 6.2 °C and 29.7 °C for **2a**, and −32.7 °C and 3.2 °C for **2b** respectively. Thus, it was suggested that the pristine liquid just after synthesis of **2a** was supercooling liquid at room temperature.

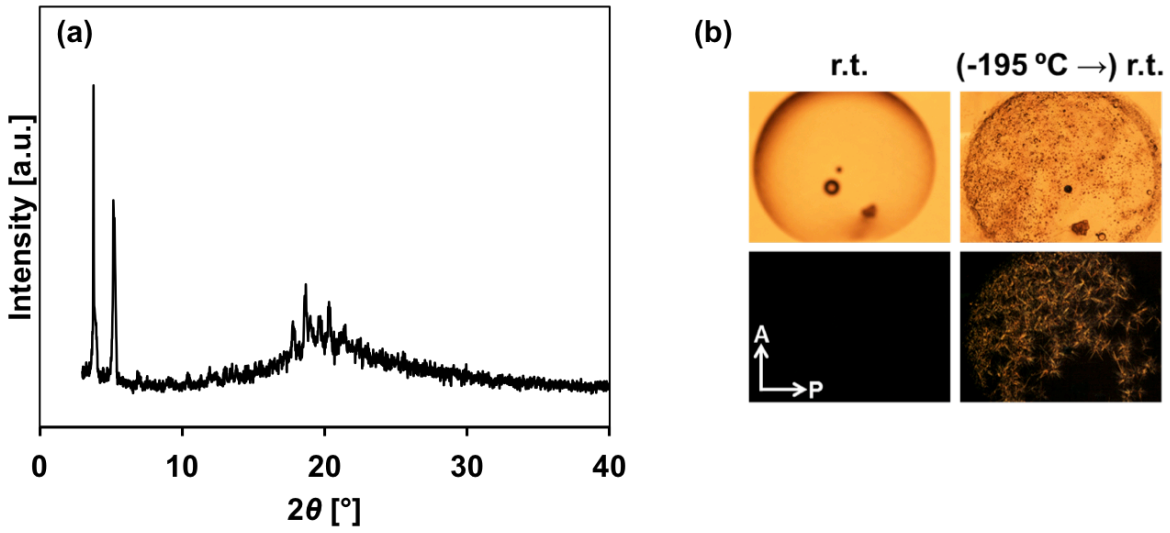

Figure 8. (a) XRD pattern of 2a at room temperature after cooling to −196 °C. (b) Polarized light microscopy image of 2a at room temperature as prepared (left) and after cooling to −196 °C (right).

When **2a** was slowly warmed to room temperature after cooling at −150 °C, the diffraction pattern of **2a** was observed by XRD measurement, and birefringence was also observed on a cross polarized microscopy. Similar to the differences in photophysical properties between **2a** and **2c** shown in Table 1, the Φ_f of **2a** after experience of cooling process was lower than **2a** just after synthesis, while the Φ_f of **2a** was extremely high (0.98) at −196 °C. Interestingly, **2a** and **2b** had no peaks on DSC measurements during the cooling process after heating to 100 °C. Thus, **2a** and **2b** are liquid at around room temperature after heating, and solid after cooling, indicating that they had the hysteresis in the thermal process.

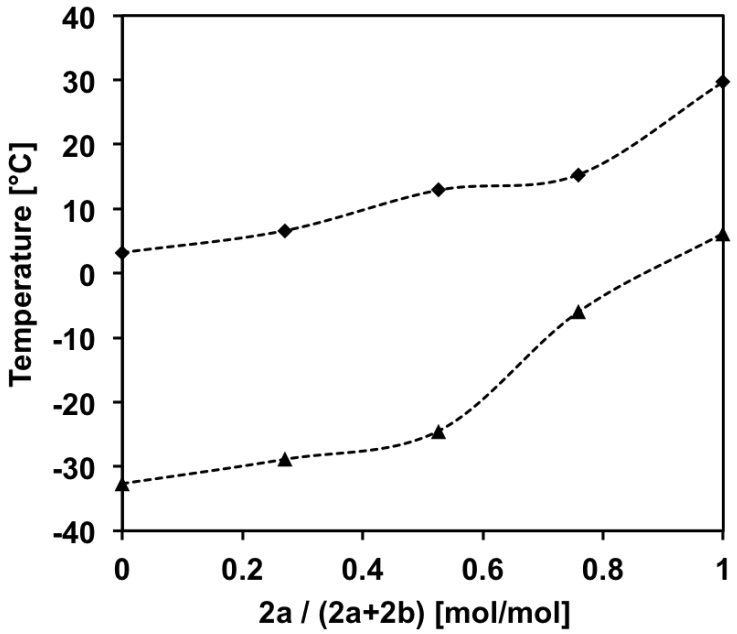

Figure 9. Phase diagram of **2a** and **2b**, and the mixture of **2a** and **2b** with various molar ratio.

When **2a** and **2b** were mixed, their T_c and T_m were readily shifted depending on the molecular ratio of **2a** and **2b**, implying that the phase transition temperature was controllable.

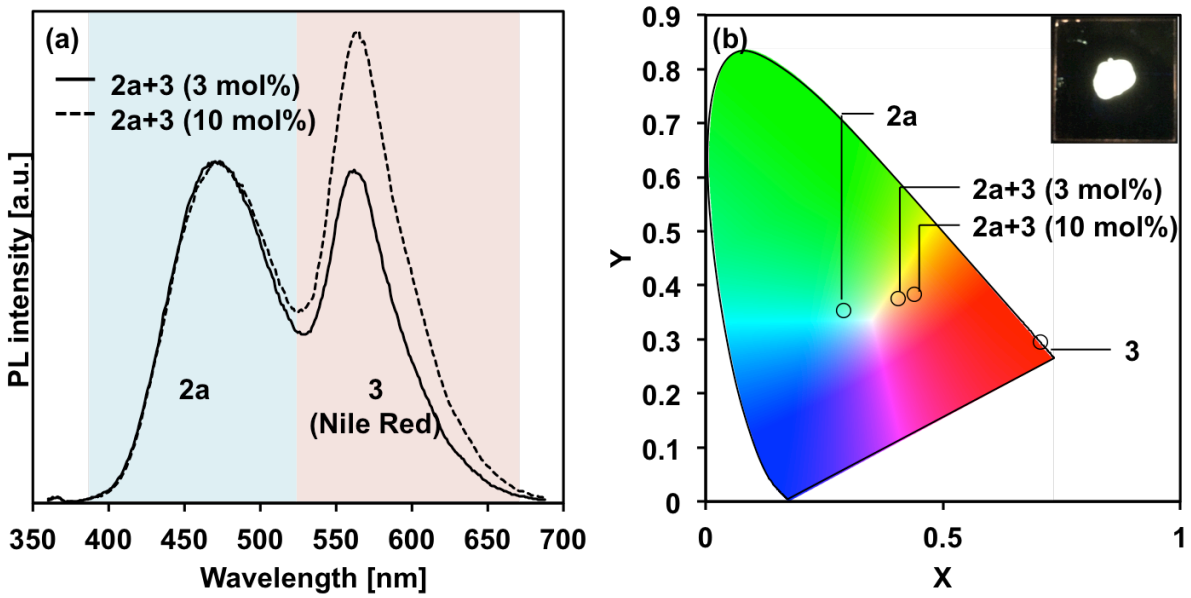

Figure 10. (a) PL spectra of **2a** and **3** (Nile red) mixtures. (b) Commission Internationale de l'Eclairage (CIE) chromaticity diagram mapping the x,y colour coordinates of **2a** (bulk state), **3** (dissolved in ethyl acetate), and the mixture of **2a** and **3** (bulk state). The inset shows a photograph of **2a** + **3** (3 mol%) under UV light irradiation (365 nm).

Thanks to the liquid nature, the liquid molecules synthesized in this study solubilize other organic dyes. To demonstrate this idea, the red luminescent organic dye Nile Red (**3**) was added to **1b** and subsequently stirred the mixtures will to be dissolved in liquid molecule **1b**. Originally, **2a** showed bright sky blue emission in the bulk state, however, when the two emission spectra integrated by mixing **2a** and **3** (**3**/**2a** = 3 mol%), they emit while luminescence under UV light irradiation (Figure. 10a). The energy transfer efficiency (Φ_T) was calculated according to the following equation; $\Phi_T = 1 - \Phi_{f,mixed\mathbf{2a}}/\Phi_{f,pure\mathbf{2a}}$. The Φ_T of **2a** + **3** was 85 %, which was good agreement with the previous report. On the Commission Internationale de l'Eclairage (CIE) chromaticity diagram mapping, a composite emission color (0.41, 0.38) located at the midpoint between **2a** (0.29, 0.35) and **3** (0.70, 0.29) (Figure 10b). Increasing the amount of 3 (**3**/**2a** = 10 mol%) resulted in a moderate change in the emission color (0.43, 0.38), proving that the emission color can be fine-tuned by the mixing ratio. The liquid molecules are also applicable in ink-jet printing.

Conclusion

This chapter described the liquefaction of TPE and their luminescent properties. Liquid TPE was synthesized by introducing of bulky alkyl chains. The liquefaction provided significant differences to the photophysical and thermal properties. In the bulk state, the TPE showed strong emission with higher Φ_f and longer λ_{em} in the liquid state than in the solid state because of the inherent amorphous nature of liquid molecules, which indicated ACQ effect was also observed in densely packed crystals of AIE molecules as well as crystals of general luminogens. The ester-linked liquid TPE was a supercooling liquid just after the synthesis and showed lower Φ_f than the ether-linked TPE, also suggesting intermolecular interactions, such as hydrogen bonding, affected the luminescence properties of AIE molecules in the bulk state. Furthermore, the luminescent color of liquid TPE could be readily tuned by mixing with other luminescent dyes.

Experimental Section

Materials. All other reagents were obtained from commercial sources and used without further purification. Tetra(4-hydroxyphenyl)ethane (**TPE-4OH**),[10] 1-bromo-2-hexyldecane,[11] 1-bromo-2-octyldodecane,[11] 2-octyl-1-dodecanoic acid,[12] **1Me**,[10] and **2Me**[13] was synthesized and characterized according to the reported method. The reaction was carried out under nitrogen atmosphere. DMAP: *N*,*N*-dimethyl-4-aminopyridine, EDC: 1-ethyl-3-(3-dimethylaminopropyl)carbodiimide.

Measurements. ^{1}H (500 MHz) and ^{13}C (126 MHz) NMR measurements were recorded on a Bruker Biospin AVANCE DRX500 instrument, using 0.05% tetramethylsilane (TMS) as an internal standard. UV-Vis spectra were recorded on a JASCO V-570 spectrophotometer. Emission spectra were obtained with SHIMADZU RF5300PC spectrofluorometer. The absolute luminescence quantum yield (Φ_F) was measured by a Hamamatsu C9920-02 absolute photoluminescence quantum yield measurement system equipped with an integrating sphere apparatus and a 150W continuous-wave xenon light source. Fourier transform infrared (FTIR) spectra were observed with a JASCO FTIR-4100 SK spectrometer with a diamond prism kit PKS-ZNSE for (attenuated total reflection) ATR technique. Differential Scanning Calorimetry (DSC) was conducted by METLLER TOLEDO DSC1 Star System with heating rate of 10 °C /min under nitrogen atmosphere. X-ray diffraction (XRD) patterns were obtained by using a Bruker D8Advance / D with Cu Kα radiation source (40 kV, 40mA). Optical / Polarization micrographs were obtained by using a Nikon instruments SNZ1000 stereoscopic zoom microscope. Viscosity measurement was conducted by using a TA Instruments ARES-G2 Viscometer and Brookfield Engineering DV2T Viscometer. Electron spray ionization mass spectroscopy (ESI-MS) was carried out at Global Facility Center, Hokkaido University.

X-ray Crystallography Analyses. Single-crystals of **1Me** and **2Me** were mounted in the loop using paraffin oil. The data were collected on a Rigaku AFC-7R Mercury diffactometer with graphite monochromated Mo Kα radiation (0.71069 Å) and a rotating-anode generator operating at 50 kV and 200 mA. Diffraction data were collected and processed using the CrystalClear program.[14] Structures were solved by direct methods using SHELXS-97.[15] Structural refinements were conducted by the full-matrix least-squares method using SHELXH-97.[15] Non-H atoms were refined anisotropically, and H atoms were refined using the riding model. All calculations were performed using the Yadokari-XG software package.[16]

Synthetic procedure and characterization.

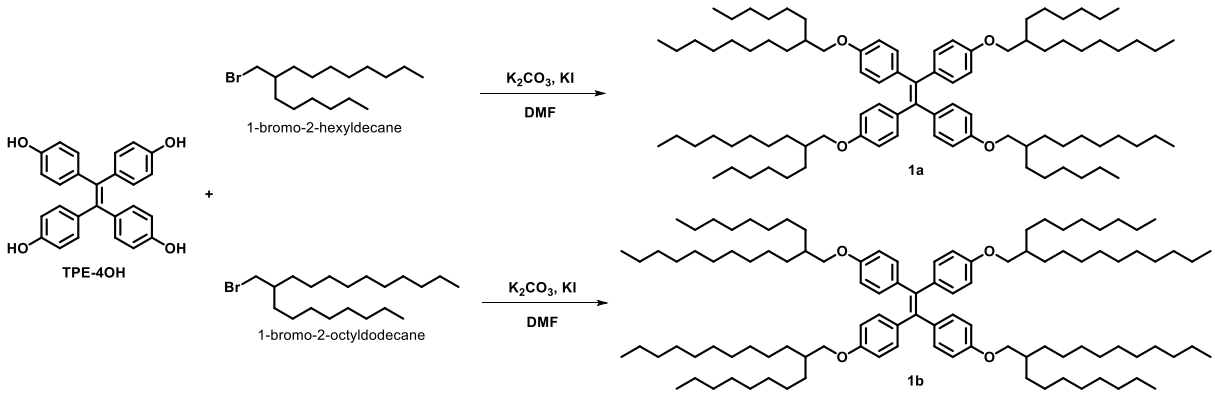

Scheme 1. Synthetic route for ether compounds **1a** and **1b**.

In a 50 mL three necked flask, tetra(4-hydroxyphenyl)ethene (**TPE-4OH**, 132 mg, 0.333 mmol), K_2CO_3 (553 mg, 4.00 mmol) and KI (3.38 mg, 0.0204 mmol) were added into anhydrous DMF (10 mL). An alkyl bromide (2.13 mmol) in anhydrous DMF (2 mL) was then added dropwise, and the mixture was stirred at 120 °C for 24 h. After cooling to room temperature, water and $CHCl_3$ were added. The organic layer was separated and the water layer was extracted with $CHCl_3$. The organic layer was combined, washed with brine three times and dried over Na_2SO_4. The solvent was removed under reduced pressure and the resulting crude product was purified by silica gel column chromatography (n-hexane / $CHCl_3$ = 5 / 1) to afford **1a** and **1b** as a yellow viscous liquid.

1a (61%): ^{1}H NMR (500 MHz, $CDCl_3$) δ (ppm): 6.91 (8H, d, J = 8.7 Hz), 6.62 (8H, d, J = 8.8 Hz), 3.74 (8H, d, J = 5.8 Hz), 1.78-1.70 (4H, m), 1.42-1.20 (80H, m), 0.87 (24H, t, J = 6.9 Hz).

^{13}C NMR (126 MHz, $CDCl_3$) δ (ppm): 157.55, 138.26, 136.80, 132.51, 113.58, 70.83, 38.04, 31.93, 31.37, 30.04, 29.71, 29.61, 29.36, 26.89, 22.70, 14.14. HRMS(ESI) Calcd. for $C_{90}H_{148}O_4$ $[M+H]^+$: *m*/*z* 1294.1456, Found: *m*/*z* 1294.1450..

1b (35%): ^{1}H NMR (500 MHz, $CDCl_3$) δ (ppm): 6.90 (8H, d, J = 8.8 Hz), 6.62 (8H, d, J = 8.8 Hz), 3.74 (8H, d, J = 5.7 Hz), 1.76-1.65 (4H, m), 1.42-1.20 (136H, m), 0.88 (24H, t, J = 6.9 Hz). ^{13}C NMR (126 MHz, $CDCl_3$) δ (ppm): 157.56, 138.27, 136.81, 132.51, 113.59, 70.84, 38.04, 31.94, 31.37, 30.05, 29.67, 29.37, 26.90, 22.72, 14.15; HRMS(ESI) Calcd. for $C_{106}H_{180}O_4$ $[M+H]^+$: *m*/*z* 1518.3960. Found: *m*/*z* 1518.3954.

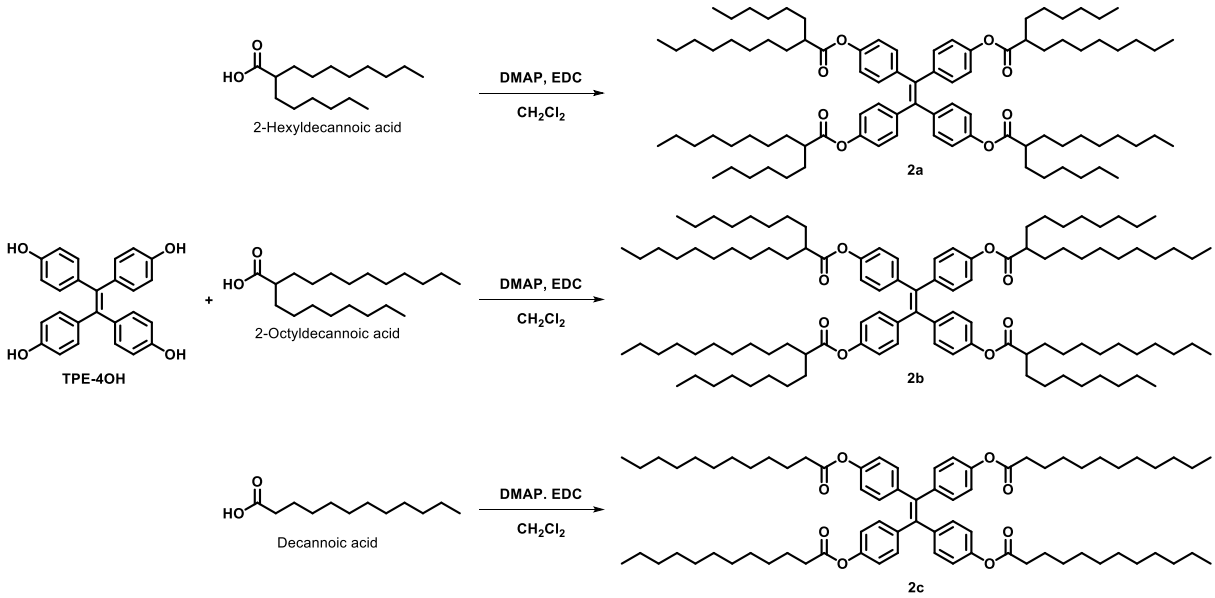

Scheme 2. Synthetic route for ester compounds **2a-c**.

In a 100 mL three necked flask, tetra(4-hydroxyphenyl)ethene (300 mg, 0.757 mmol), DMAP (407 mg, 3.33 mmol) were dissolved in anhydrous $CHCl_3$ (40 mL). After the solution was cooled, a carbonic acid (3.33 mmol) and EDC·HCl in anhydrous $CHCl_3$ (15 mL) was added dropwise to the solution. The mixture was stirred at room temperature for 18h. Then the mixture was washed with diluted HCl and H_2O, and dried over $MgSO_4$. The solvent was removed under reduced pressure and the resulting crude product was purified by silica gel column chromatography using n-hexane / ethyl acetate mixture as an eluent. The volume ratio of n-hexane to ethyl acetate was adjusted according to each molecule. The products were given as a yellow viscous liquid.

2a (87%): ^{1}H NMR (500 MHz, $CDCl_3$) δ (ppm): 7.01 (8H, d, J = 8.6 Hz), 6.82 (8H, d, J = 8.7 Hz), 2.55-2.48 (4H, m), 1.75-1.67 (15H, m), 1.58-1.50 (8H, m), 1.39-1.25 (80H, m), 0.89-0.85 (24H, m). ^{13}C NMR (126 MHz, $CDCl_3$) δ (ppm): 174.81, 149.47, 140.69, 139.54, 132.34, 121.06, 45.86, 32.50, 31.84, 31.68, 29.58, 29.44, 29.24, 27.46, 22.63, 14.06. HRMS(ESI) Calcd. for $C_{90}H_{140}O_8$ $[M+Na]^+$: *m*/*z* 1372.0446. Found: *m*/*z* 1372.0440.

2b (34%): ^{1}H NMR (500 MHz, $CDCl_3$) δ (ppm): 7.02 (8H, d, J = 8.8 Hz), 6.82 (8H, d, J = 8.5 Hz), 2.55-2.48 (4H, sep, J = 5.3 Hz), 1.61-1.45 (8H, m), 1.40-1.20 (112H, m), 0.88 (24H, t, J = 6.3 Hz). ^{13}C NMR (126 MHz, $CDCl_3$) δ (ppm): 174.88, 149.43, 140.69, 139.51, 132.36, 121.08, 45.86, 32.50, 31.92, 29.62, 29.50, 29.45, 29.30, 27.51, 22.71, 14.14. HRMS(ESI) Calcd. for $C_{106}H_{172}O_8$ $[M+Na]^+$: *m*/*z* 1596.2950. Found: *m*/*z* 1596.2944.

2c (87%): ^{1}H NMR (500 MHz, $CDCl_3$) δ (ppm): 7.00 (8H, d, J = 8.7 Hz), 6.84 (8H, d, J = 8.7 Hz), 2.50 (8H, t, J = 7.5 Hz), 1.72 (8H, quin, J = 7.5 Hz), 1.21-1.40 (64H, m), 0.88 (12H, t, J = 6.9 Hz). ^{13}C NMR (126 MHz, $CDCl_3$) δ (ppm): 172.10, 149.39, 140.58, 139.63, 132.33, 120.95, 34.43, 31.93, 29.62, 29.47, 29.35, 29.29, 29.12, 24.91, 22.71, 14.15. HRMS(ESI) Calcd. for $C_{74}H_{108}O_8$ $[M+Na]^+$: *m*/*z* 1147.7942. Found: *m*/*z* 1147.7936.

References

[1] J. Mei, N. L. C. Leung, R. T. K. Kwok, J. W. Y. Lam, B. Z. Tang, *Chem. Rev.*, **2015**, *115,* 11718–11940.

[2] X. Zhang, X. Zhang, L. Tao, Z. Chi, J. Xu, Y. Wei, *J. Mater. Chem. B*, **2014**, *2*, 4398–4414.

[3] A. Qin, J. W. Y. Lam, B. Z. Tang, *Prog. Polym. Sci.*, **2012**, *37*. 182–209.

[4] Y. Hong, J. W. Y. Lam, B. Z. Tang, *Chem. Soc. Rev.*, **2011**, *40*, 5361–5388.

[5] Y. Hong, J. W. Y. Lam, B. Z. Tang, *Chem. Commun.*, **2009**, 4332–4353.

[6] S. S. Babu, J. Aimi, H. Ozawa, N. Shirahata, A. Saeki, S. Seki, A. Ajayaghosh, H. Möhwald, T. Nakanishi, *Angew. Chem. Int. Ed.,* **2012**, *51*, 3391–3395.

[7] S. S. Babu, M. J. Hollamby, J. Aimi, H. Ozawa, N. Shirahata, A. Saeki, S. Seki, K. Kobayashi, K. Hagiwara, M. Yoshizawa, H. Möhwald, T. Nakanishi, *Nat. Commun*, **2013**, *4,* 1969.

[8] J. Chen, C. C. W. Law, J. W. Y. Lam, Y. Dong, S. M. F. Lo, I. D. Williams, D. Zhu, B. Z. Tang, *Chem. Mater.* **2003**, *15*, 1535–1546.

[9] H. Tong, Y. Hong, Y. Dong, M. Haußler, J. W. Y. Lam, Z. Li, Z. Guo, Z. Guo, B. Z. Tang, *Chem. Commun.* **2006**, 3705–3707.

[10] K. Kokado, R. Taniguchi, K. Sada, *J. Mater. Chem. C*, **2015**, *3*, 8504−8509.

[11] H. Li, S. Diele, S, S. Babu, S, T. Turner, D. Neher, M. J. Hollamby, T. Seki, S. Yagai, Y. Deguchi, H. Möhwald, T. Nakanishi, *J. Mater. Chem. C*, **2013**, *1*, 1943−1951.

[12] J. W. Rumer, S. Dai, M. Levick, L. Biniek, D, J. Procter, I. McCulloch, *J. Polym. Chem. A Polym. Chem.*, **2013**, *51*, 1285−1291.

[13] A. Schreivogel, J. Maurer, R. Winter, A. Baro, S. Laschat, *Eur. J. Org. Chem.*, **2006**, 3395−3404.

[14] *CrystalClear*; Molecular Structure Corp.: Orem, UT, **2001**.

[15] *SHELX-97*; G. M. Sheldrick, *Acta Crystallogr.*, *Sect. A: Found. Crystallogr.*, **2008**, *64*, 112−122.

[16] *Yadokari-XG*; Program for Crystal Structure Analysis. K. Wakita, **2000**.

Chapter III

The effect of C=C bond twist to AIE behavior

Chapter III

The effect of C=C bond twist to AIE behavior

Abstract: This chapter describes the large structural change of TPE in the excited state with experimental observations and theoretical computations, in order to obtain deep insight into the nonradiative decay process of AIE molecules. Cis-trans isomers of TPE derivatives were obtained by carefully purifications with chromatography and recrystallization. Photoirradiation to the isomers in the diluted solutions resulted in the equilibrium state with isomeric ratio of approximately 1:1 via rapid isomerization. In contrast, photoisomerization was inhibited in the solid state. Theoretical computations could explain the experimental results. In the diluted solution, the rotation of the phenyl ring is activated by photoexcitation to achieve the planar conformation of the phenyl rings and C=C double bond, which relax the excited state, consequently leading to the nonradiative decay. In the crystal, solid and aggregated states, the C=C bond twist is severely restricted by the surrounding molecules, thereby resulting in strong emission.

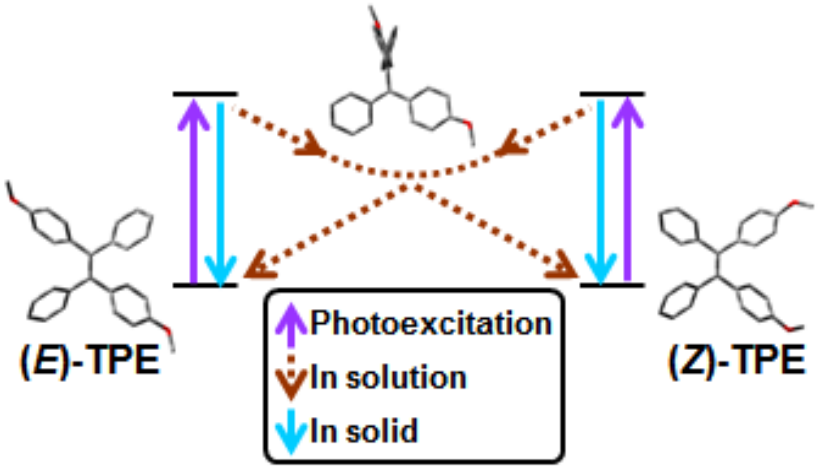

Introduction

Aggregation-induced emission (AIE) is a unique photoluminescent behavior; AIE luminogens (AIEgens) are non-emissive in the diluted solution but they become emissive by aggregation.[1-5] Due to the attractive solid-state emission and switchable properties, AIEgens have been intensely studied for the use in organic light emitting diode (OLED)[6-8] and fluorescence probes.[9-11] To advance such applied researches, it is important to understand the mechanism underlying the AIE phenomenon, which will lead to the rational design of new AIEgens without trial and error or accidental discovery.

Tetraphenylethene (TPE) is archetypal AIEgen and the AIE mechanism have been well studied. The restriction of intramolecular rotation (RIR) of the phenyl rings at the aggregated state is generally accepted as a main cause of the AIE phenomenon of TPE.[12] In these days, however, RIR mechanism has been suspected, because a few system that can induce luminescence without RIR have been reported. For example, Shinkai *et al.* reported "cyclization-induced emission" of TPE derivatives with zinc dipicolylamine groups interacting with dicarboxylic acids in homogeneous buffer solution.[13] Notably, the rotation of phenyl rings can still occur even after cyclization, because the phenyl rings are linked between vicinal positions of TPE derivatives.

Since TPE is a symmetrical α,α'-diphenylstilbene, is it reasonable to consider that TPE undergoes *E*-*Z* isomerization (EZI) through a π-bond twist (π-twist) after photoexcitation in a similar manner as stilbene and its derivatives.[14-25] Indeed, before the recognition of AIE phenomenon, Babra *et al.* and Greene independently reported π-twist of TPE in the excited state based on temperature- and viscosity-dependent fluorescence and picosecond spectroscopy in the solution,[26,27] followed by femtosecond spectroscopy by Wiersma and co-workers.[28,29] Nonetheless, the studies considering the π-twist of TPE derivatives, including EZI, in the excited state has very limited in the field of AIE.[30-33]

In earlier reports, Tang *et al.* denied the involvement of EZI because of the results from conventional photoluminescence measurements of pure *E* and *Z* isomers of TPE derivatives.[30,31] On the other hand, in a recent report, they recognized the involvement of EZI

in quenching mechanism of TPE derivatives in the solution.[32] Furthermore, recent computational studied suggested that, in the ultrafast photophysical quenching process of TPE derivatives, existence of conical intersection (CI) related to the cyclization and π-twist rather than the rotation of phenyl rings.[34-35] Inspired by these reports, in this chapter, I performed photochemical experiments and theoretical calculations of di-substituted TPE derivatives to elucidate the origin of the quenching mechanism of TPE derivatives in the solution.

Results and Discussion

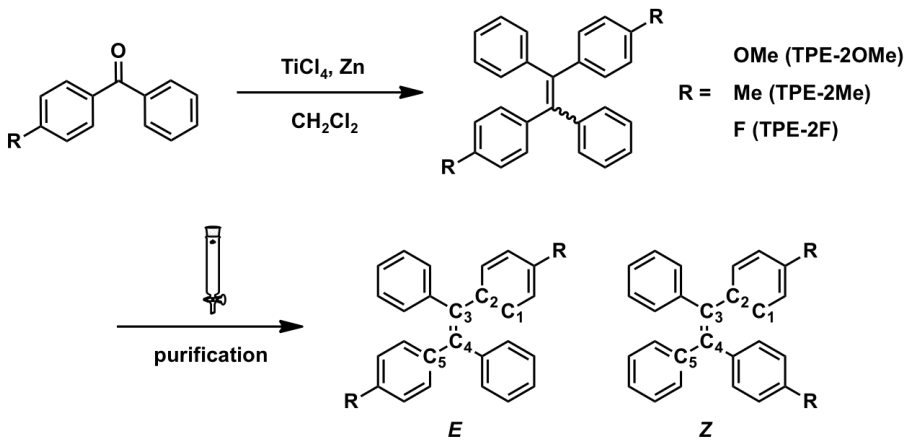

Figure 1. Synthesis of *E* and *Z* isomers of **TPE-2OMe**, **TPE-2Me**, and **TPE-2F**.

Di-substituted TPE derivatives, named **TPE-2OMe**, **TPE-2Me**, and **TPE-2F** were synthesized by Mcmurry coupling from the corresponding mono-substituted benzophenone derivatives (Figure 1). They were carefully purified by silica gel column chromatography or recrystallization to obtain *E* and *Z* isomers. The para-substituents mainly affected the reaction yield rather than the *E*/*Z* ratio of the product, unlike the bulky ortho-substituent.[36] For these molecules, the *E*/*Z* ratio of the product before purification was close to 50/50. The ease of purification using silica gel column chromatography was mainly dependent on the substituents at the para-position; the *E* and *Z* isomers having large dipole moment from heteroatomic substituents (**TPE-2OMe**, **TPE-2F**) were separated easily, whereas hydrocarbon-substituted TPE (**TPE-2M**) showed no difference in the retension times, consistent with previously reports.

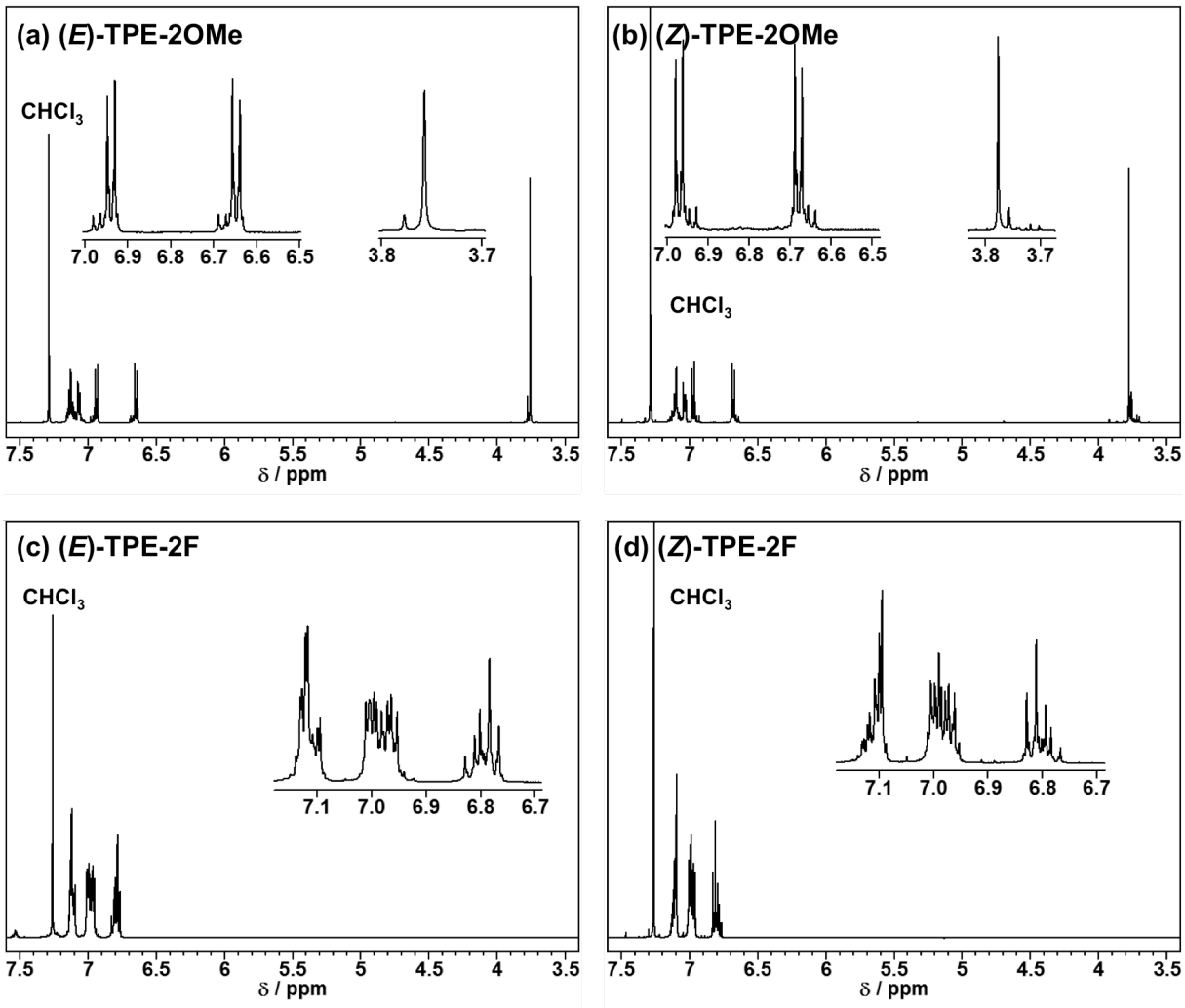

Figure 2. ^{1}H NMR spectra of (a) (*E*)-rich **TPE-2OMe**, (b) (*Z*)-rich **TPE-2OMe**, (c) (*E*)-rich **TPE-2F**, (b) (*Z*)-rich **TPE-2F** (500 MHz, $CDCl_3$).

The *E* and *Z* isomers were distinguishable by ^{1}H NMR spectroscopy (Figure 2). For example, the protons on the methoxy groups of **TPE-2OMe** resulted in a 0.02 ppm chemical shift difference between the *E* and *Z* isomers. A similar difference in chemical shift was observed in **TPE-2F** isomers.

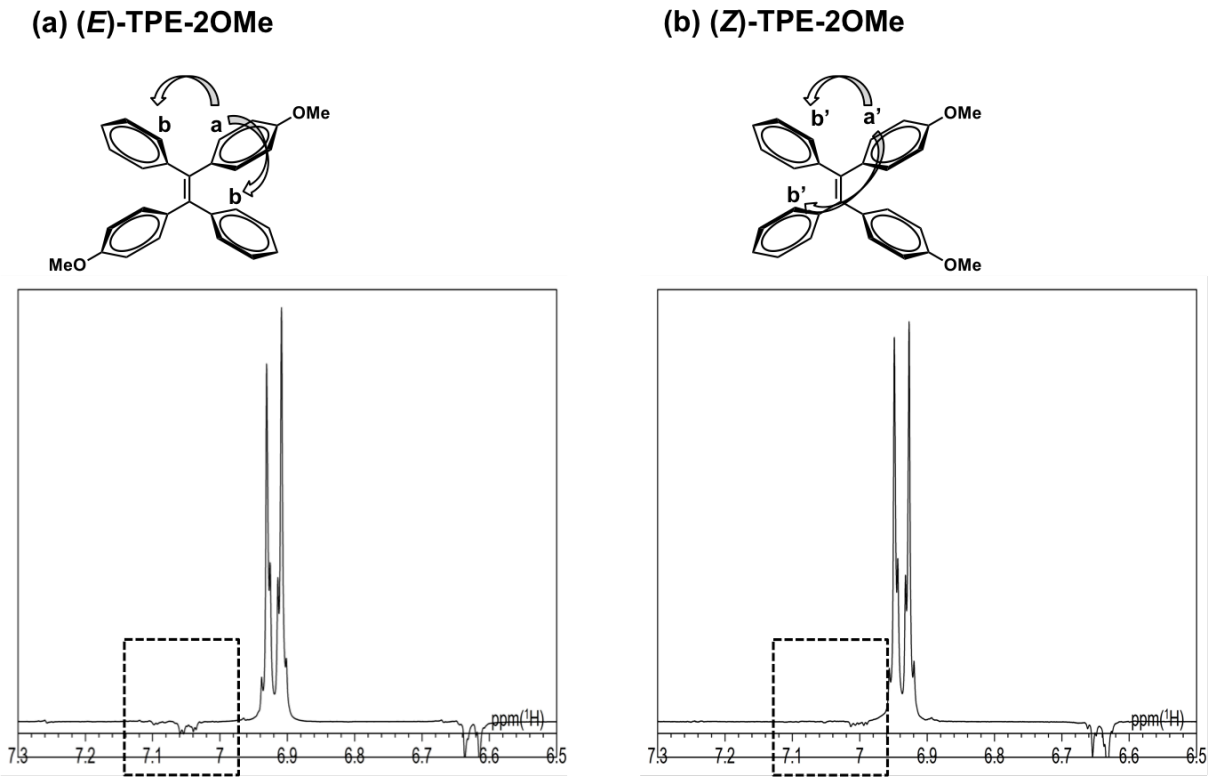

Figure 3. Nuclear Overhauser effect (NOE) spectra of (a) (*E*)-**TPE-2OMe** and (b) (*Z*)-**TPE-2OMe**.

The isomers could be identified by nuclear Overhauser effect (NOE) spectra between protons at the ortho-positions of different and vicinal phenyl groups (Figure 3).

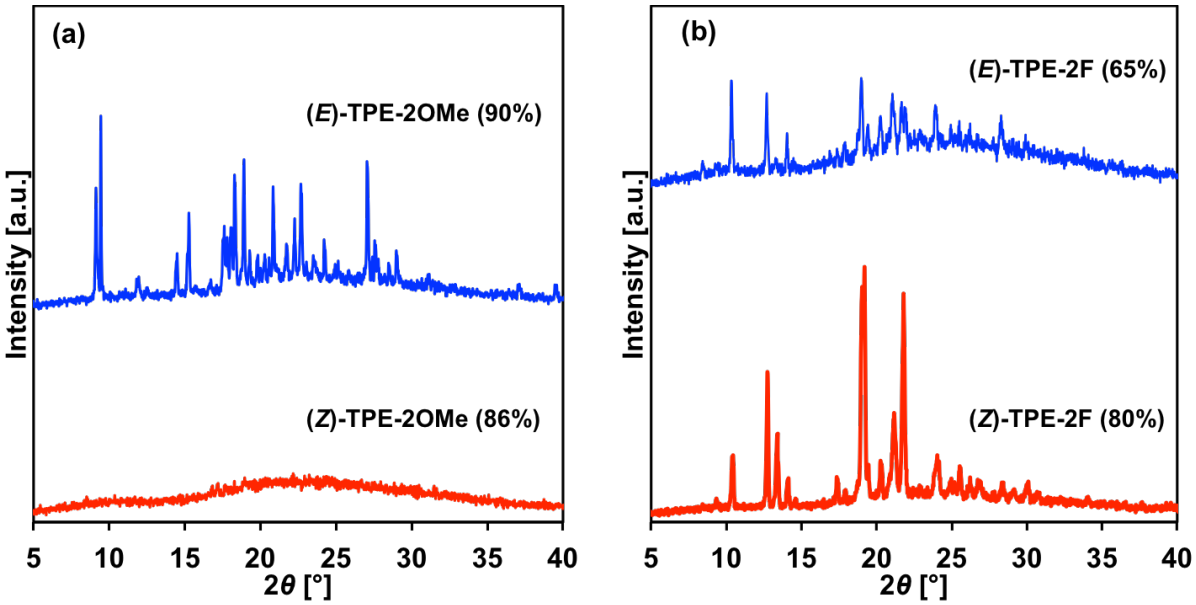

Figure 4. X-ray diffraction (XRD) patterns of (a) (*E*)-rich **TPE-2OMe** ((*E*) isomer: 90 %) and (*Z*)-rich **TPE-2OMe** ((Z) isomer: 86 %), and (b) (*E*)-rich **TPE-2F** ((*E*) isomer: 65 %) and (*Z*)-rich **TPE-2F** ((Z) isomer: 80 %).

These isomers exhibited different crystallinities, as revealed by X-ray diffraction (XRD) measurements (Figure 4). In particular, it was observed that *Z*-rich **TPE-2OMe** was amorphous while *E*-rich **TPE-2OMe** was crystalline. Both isomers of **TPE-2F** were also crystalline, but the XRD patterns were different.

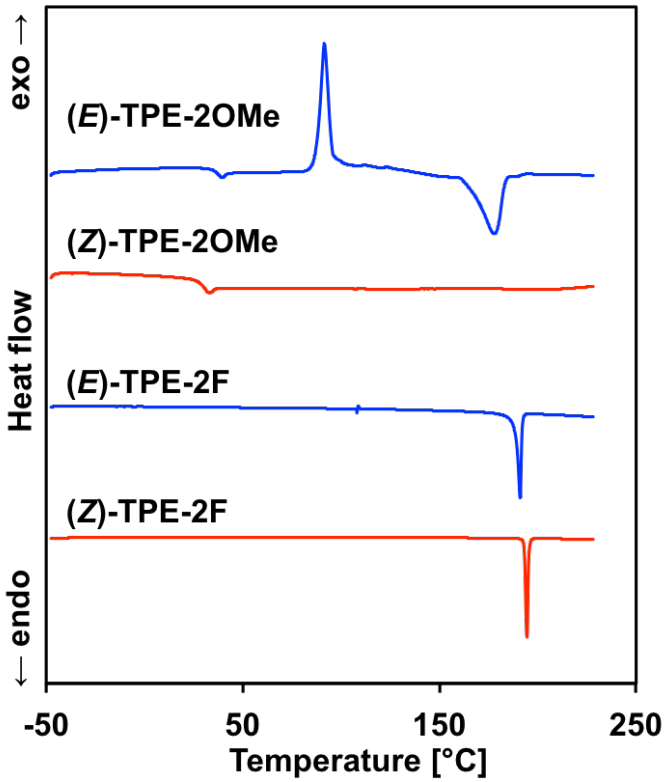

Figure 5. Different scanning calorimetry (DSC) chart of (a) (*E*)-rich **TPE-2OMe** ((*E*) isomer: 90 %), (*Z*)-rich **TPE-2OMe** ((Z) isomer: 86 %), (b) (*E*)-rich **TPE-2F** ((*E*) isomer: 65 %), and (*Z*)-rich **TPE-2F** ((Z) isomer: 80 %). The chart shows the result of 2nd scan with 10 °C/min heating rate.

Table 1. Thermal properties of the isomers. Measured by DSC under nitrogen atmosphere. Heating rate was 10 °C/min.

Compound	T_g [°C]	T_c [°C]	T_m [°C]
(*E*)-TPE-2OMe	35.3	91.6	178.3
(*Z*)-TPE-2OMe	28.6	n.a.	n.a.
(*E*)-TPE-2F	n.a.	n.a.	191.0
(*Z*)-TPE-2F	n.a.	n.a.	194.5

Differential scanning calorimetry (DSC) measurements also revealed that the behavior of the isomers of **TPE-2OMe** was different during heating process (Figure 5, Table 1). In contrast, the two isomers of **TPE-2F** showed almost the similar melting points.

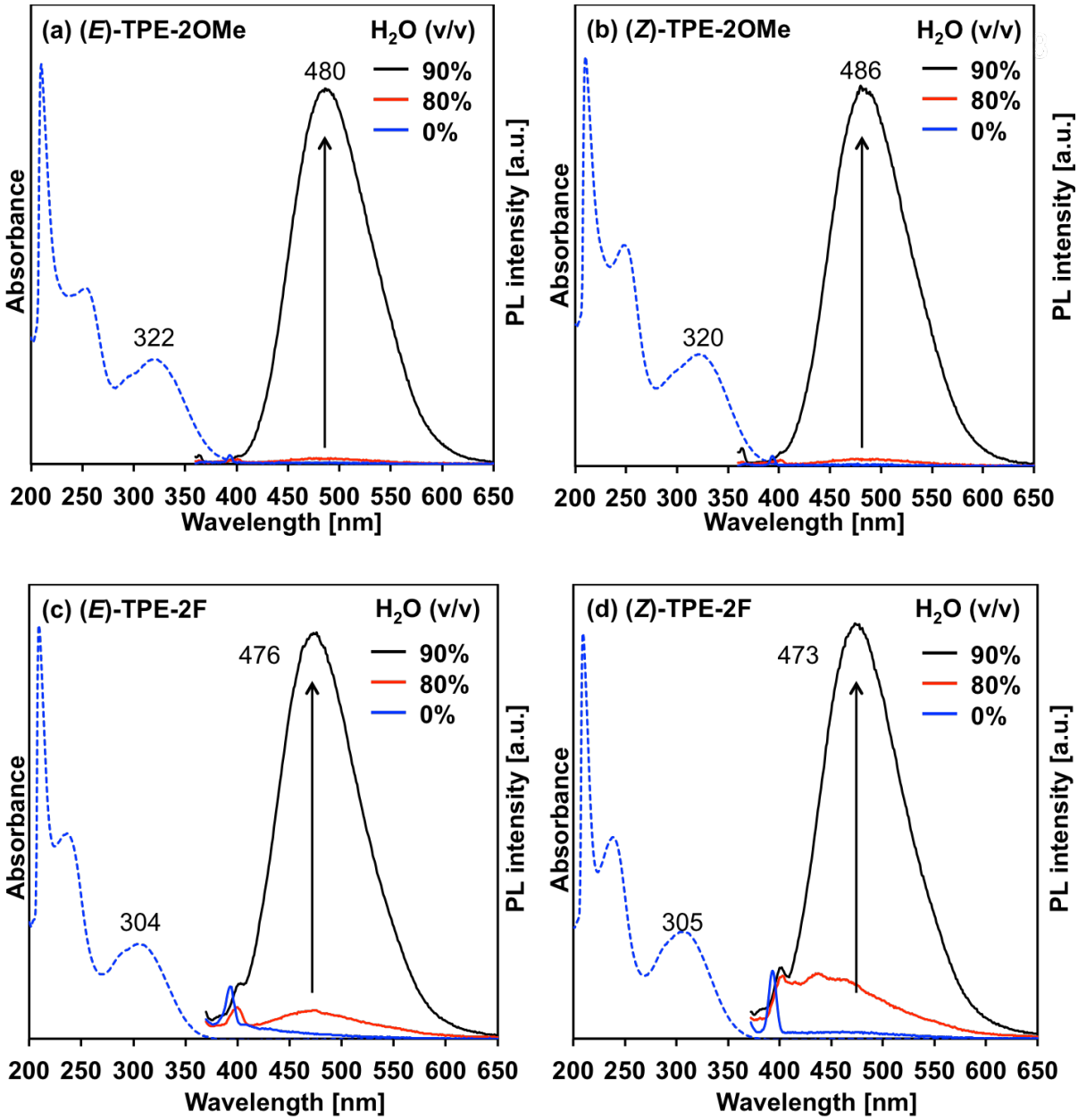

Figure 6. UV-vis and photoluminescence (PL) spectra of (a) (*E*)-**TPE-2OMe**, (b) (*Z*)-**TPE-2OMe**, (c) (*E*)-**TPE-2F**, and (d) (*Z*)-**TPE-2F**. UV-vis spectra were measured in THF (10 μM), and PL spectra were measured in THF/H_2O mixed solvent (10 μM).

The enriched isomers were subjected to photophysical experiments. It was found that both *E* and *Z*-rich **TPE-2OMe** and **TPE-2F** showed typical AIE properties; they were non-emissive in the diluted solution but were emissive in the aggregated state. These isomers showed similar absorption and photoluminescent spectra. **TPE-2F** showed hypsochromically shifted absorption and emission maxima compared with **TPE-2OMe** (Figure 6).

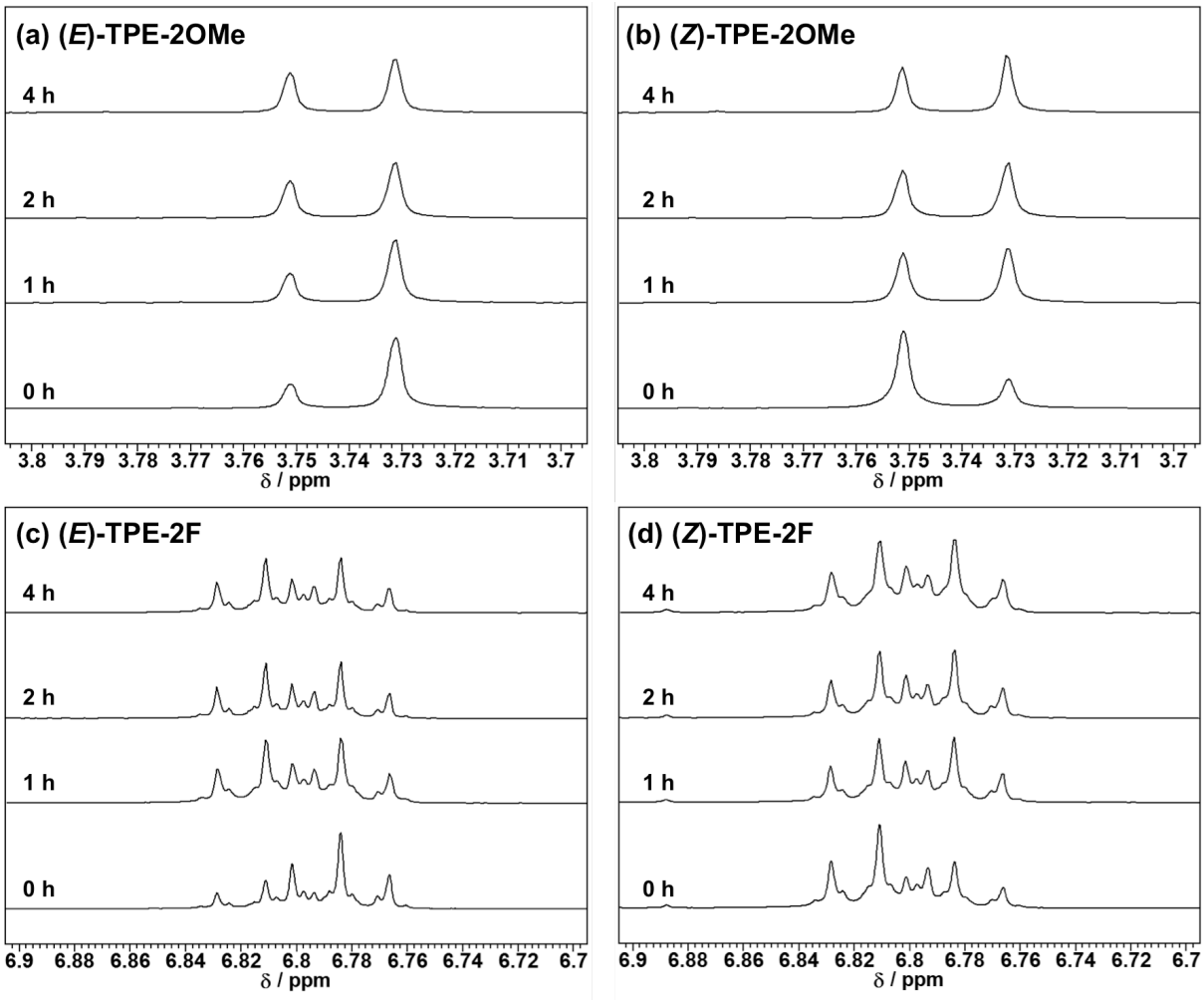

Figure 7. Time course change of ^{1}H NMR spectra upon deep UV lamp irradiation to (a) (*E*)-rich **TPE-2OMe**, (b) (*Z*)-rich **TPE-2OMe**, (c) (*E*)-rich **TPE-2F**, and (d) (*Z*)-rich **TPE-2F** (500 MHz, $CDCl_3$).

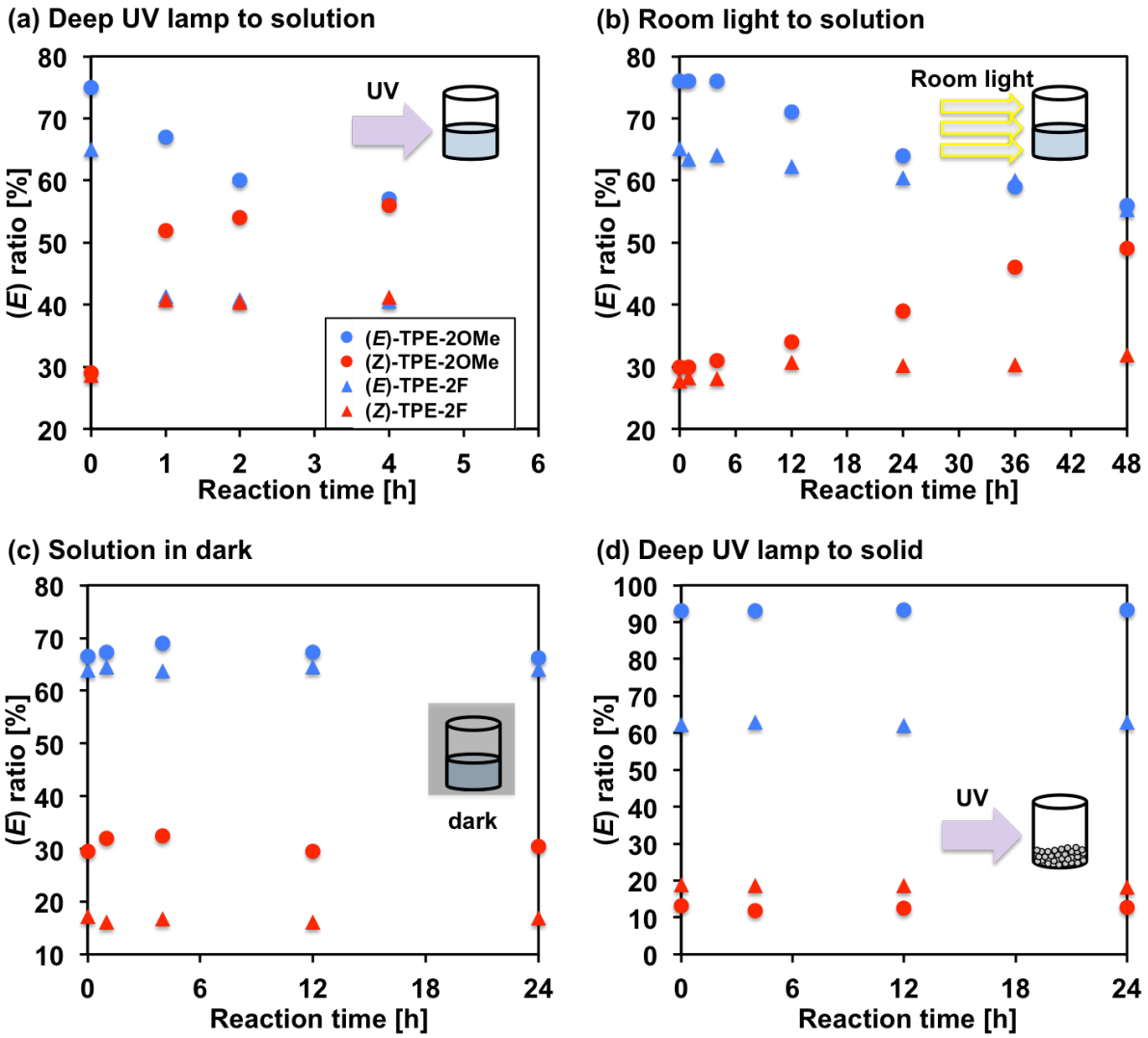

Figure 8. (a-c) Photoisomerization of **TPE-2OMe** and **TPE-2F** in chloroform solution (a) under deep-UV irradiation, (b) under ambient-light irradiation, and (c) in the dark. (d) Photoisomerization of **TPE-2OMe** and **TPE-2F** in the solid state under deep-UV lamp irradiation.

After irradiation of *E*- or *Z*-rich isomers with a deep ultraviolet (deep-UV) lamp (6.2 mW/cm^2), they showed the isomerization behavior and approached to the photostationary state, as revealed by ^1H NMR measurements (Figure 7a, 8a and 8b). In addition, the photostationary state was achieved after 1-4 h. The isomerization behavior was also observed under ambient light conditions (0.32 mW/cm^2). **TPE-2OMe** became photostationary state after 48 h irradiation of ambient light. The difference between the deep-UV light irradiation and the ambient light irradiation was due to the irradiation power and the wavelength range of the light sources. Therefore, the slow isomerization behavior of **TPE-2F** observed in the ambient light is probably due to the difference in absorption wavelength (Figure 7a, 8c and 8d). I would like to emphasize that the *E* and *Z* isomers exhibit nearly identical UV-vis absorption spectra, as shown in Figure 6, and therefore the two isomers should be equally excited. Under dark conditions, they did not exhibit isomerization behavior even after the long-time photoirradiation (Figure 7c). Moreover, in the solid state, **TPE-2OMe** and **TPE-2F** also did not show isomerization behavior under deep UV lamp irradiation (Figure 7d). I also note that I did not observed photocyclization behavior reported in other literature in the experimental condition. These results indicate that the isomerization of **TPE-2OMe** and **TPE-2F** occur under typical optical measurement conditions (0.64 mW/cm^2), and the isomerization is suppressed in the solid state under UV irradiation as well as in the solution under dark conditions. In conclusion, the alternative correlation between the isomerization and the occurrence of AIE should be observed.

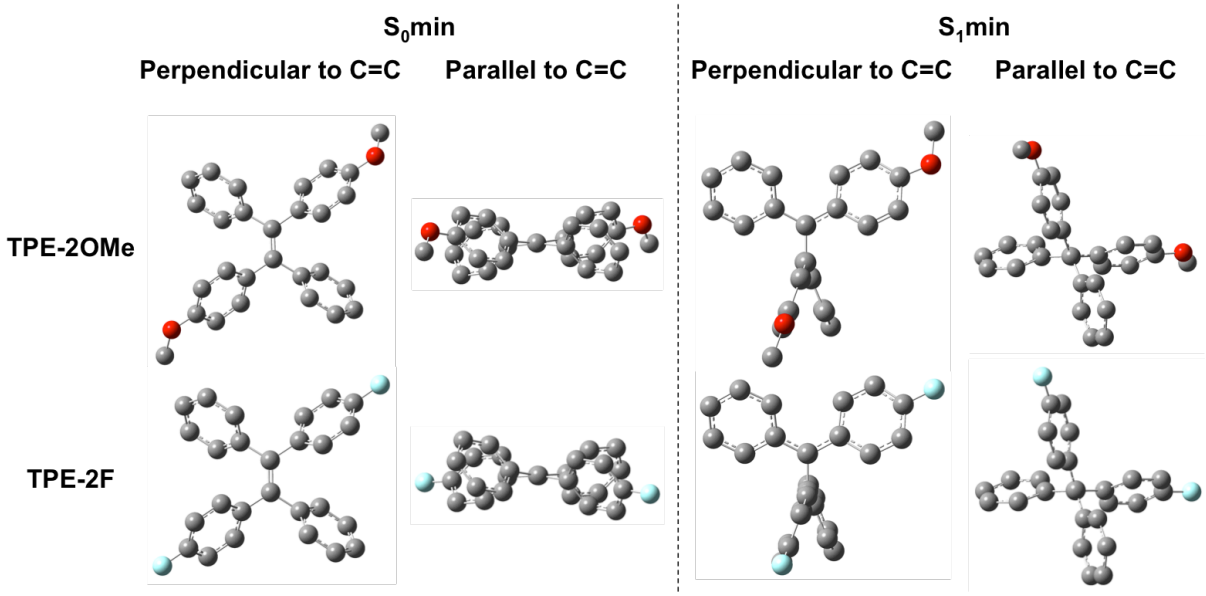

Figure 9. S_0min and S_1min structures of **TPE-2OMe**, **TPE-2F** in solution ($CHCl_3$) as obtained using the polarizable continuum model (PCM) with density functional theory (DFT) and time-dependent DFT (TDDFT) at the B3LYP/6-31+G(d) level using Gaussian 16.

Table 2. Geometrical parameters for **TPE-2OMe** and **TPE-2F** at S_0min and S_1min as calculated at the B3LYP/6-31+G(d) level.

Compound	$\theta(C_2C_3C_4C_5)$ [°]		$\theta(C_1C_2C_3C_4)$ [°]		C_3=C_4 [Å]		C_2=C_3 [Å]	
	S_0min	S_1min	S_0min	S_1min	S_0min	S_1min	S_0min	S_1min
TPE-2OMe	167	111	49	20	1.368	1.490	1.493	1.443
TPE-2F	168	105	51	20	1.366	1.490	1.496	1.447

EZI was spectroscopically observed in case of di-substituted TPE derivatives, but of course not in the tetra-substituted or naked TPEs. EZI of the di-substituted TPE derivatives should occur via π-twist in the photoexcited state, but the transitions from *E* to *E* or from *Z* to *Z* isomers is cannot be detected and is thus ignored, even though they occur via π-twist.

To obtain a deeper insight into the AIE mechanism, theoretical computations were conducted for **TPE-2OMe** and **TPE-2F** in the ground state (S_0) and singlet excited state (S_1) in solution using the polarizable continuum model (PCM)[37] by density functional theory (DFT) and time-dependent DFT (TDDFT) at the B3LYP[38,39]/6-31+G(d) level using Gaussian 16.[40] S_0min and S_1min mean the most stable optimized conformation in the S_0 and S_1 state, respectively. In chloroform solution, the calculated energies of the electron transitions from highest occupied molecular orbital (HOMO) to the lowest unoccupied molecular orbital (LUMO) (3.38 eV, f = 0.4757 for **TPE-2OMe**; 3.58 eV, f = 0.4456 for **TPE-2F**) showed the good agreement with the absorption energies observed in the ultraviolet-visible (UV-vis) absorption spectra. The dihedral angles of the C=C bonds [$\theta(C_2C_3C_4C_5)$, Figure 1] at S_0min were calculated to be 167° for **TPE-2OMe** and 168° for **TPE-2F**, while, in the excited state, they were calculated to be 111° for **TPE-2OMe** and 105° for **TPE-2F** (Figure 9 and Table 2). Additionally, the central C=C bonds considerably elongated from 1.368 Å (S_0min) to 1.490 Å (S_1min) in **TPE-2OMe** and from 1.366 Å (S_0min) to 1.490 Å (S_1min) in **TPE-2F**. Thus, the large structural change around the central C=C bond was induced by photoexcitation. However, the dihedral angle related to the central C=C bonds and phenyl rings [$\theta(C_1C_2C_3C_4)$] were calculated to be 49° (S_0min) and 20° (S_1min) for **TPE-2OMe** and 51° (S_0min) and 20° (S_1min) for **TPE-2F**, showing the variation of $\theta(C_2C_3C_4C_5)$ was much larger than that of $\theta(C_1C_2C_3C_4)$. These results indicated that the π-twist was the major role for quenching process of AIE.

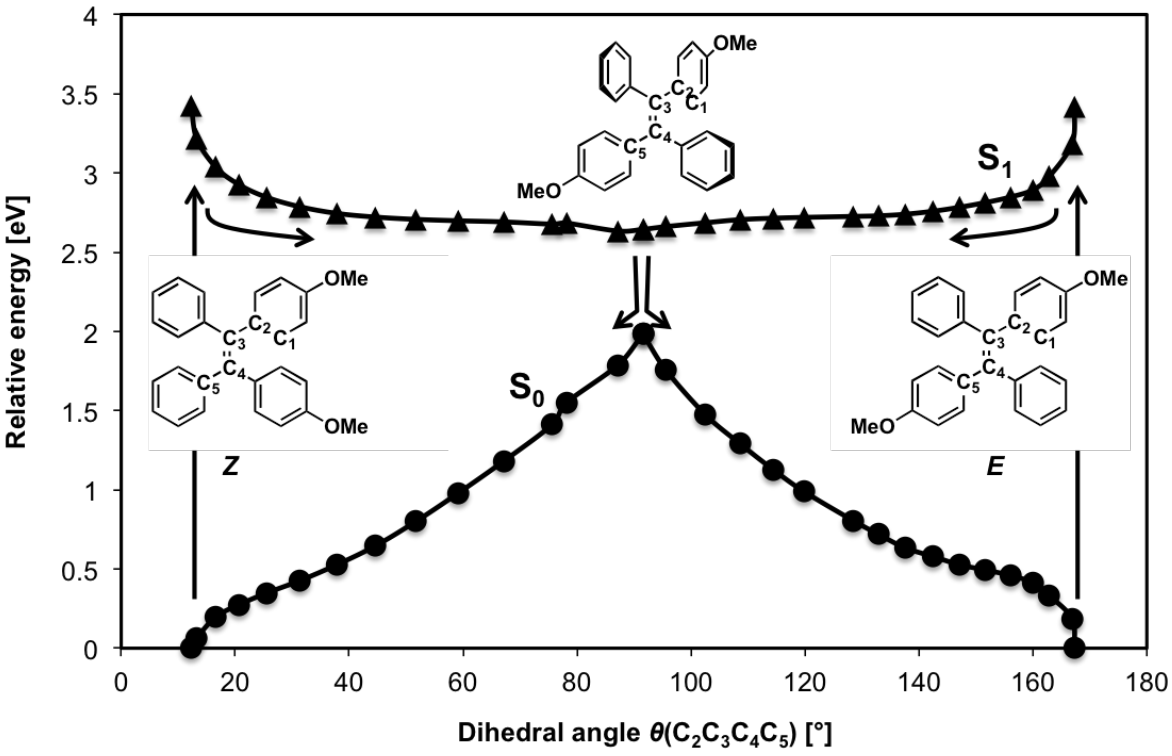

Figure 10. Energy diagram of the S_1 and S_0 state along the steepest-descent (SD) pathway in the S_1 state of **TPE-2OMe**. The horizontal and vertical axes correspond to the π-twist angle $\theta(C_2C_3C_4C_5)$ and the relative energy, respectively. The SD pathways in the S_1 state were calculated from the Frank-Condon (FC) structures (= S_0min) of the *E* and *Z* isomers.

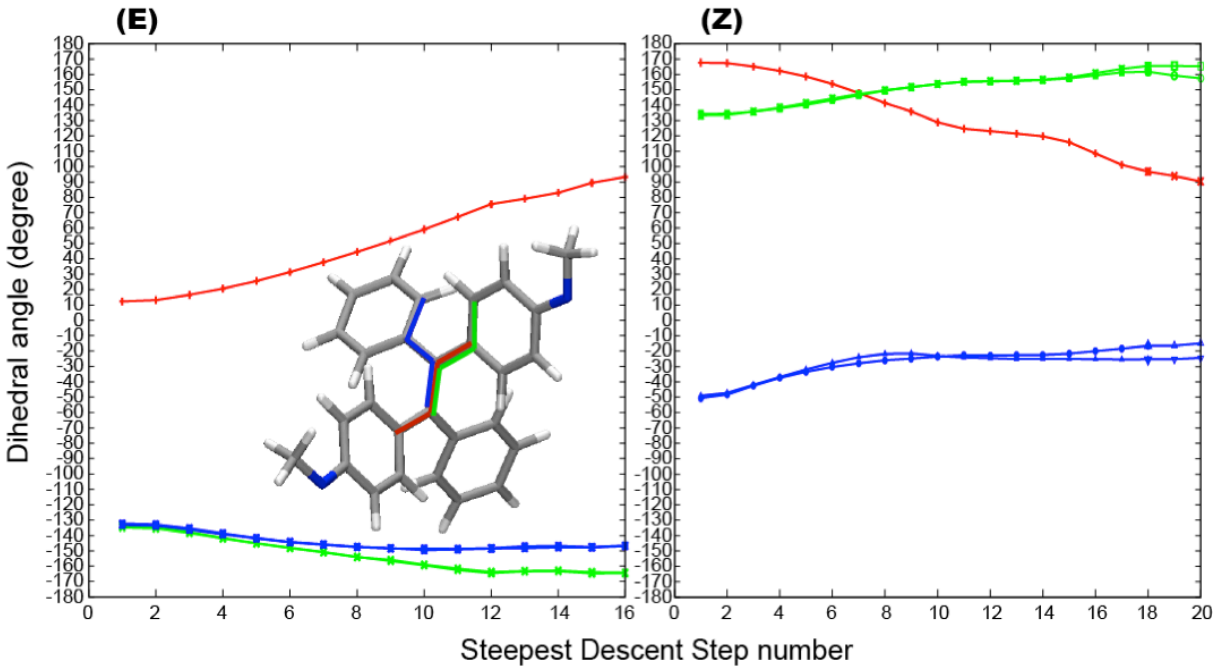

Figure 11. Dihedral angles concerning the rotation around the C=C bond (red), two PhOMe (green×2), and two Ph rings (blue×2) as shown in the inset for one of the rings are plotted against the step number of the steepest descent (SD) pathways for (*E*) and (*Z*) isomers of **TPE-2OMe**. Along the SD pathway, the C=C bond rotates constantly, while the PhOMe and Ph rings rotate mostly in the beginning and then settle down.

To verify the relaxation mechanism of the TPE derivatives in the excited state, TDDFT calculations at the B3LYP/def-SV(P) level[41] were performed using TURBOMOLE[42,43] to calculate the steepest descent pathway of the *E* and *Z* isomers of **TPE-2OMe** in the S_1 state started from their Frank-Condon (FC) structures. Figure 10 shows the energy profiles of S_1 and S_0 states along the SD pathway from the FC structures of the *E* and *Z* isomers to the midpoint as a function of the dihedral angles $\theta(C_2C_3C_4C_5)$. It should be noted that the two conformations obtained from the FC structures do not correspond at the midpoint [$\theta(C_2C_3C_4C_5) = 90°$]. Along the SD pathway, the phenyl rings initially rotate with a decrease in the dihedral angle $\theta(C_2C_3C_4C_5)$, and then the rotational motion occurred around the central C=C bond, leading to the perpendicular structure [$\theta(C_2C_3C_4C_5) = 90°$, (Figure 11)]. As the S1 energy gradually decreases, the S_0 energy increases accordingly, and finally the energy difference between the S_1 and S_0 state decreases to 0.5 eV at $\theta(C_2C_3C_4C_5) \approx 90°$,

suggesting the presence of a conical intersection (CI) near there. Although TDDFT/DFT is not a suitable method to describe the electronic structure around the CI of S_0 and S_1 states, the SCF calculations for the SD pathway converged in this study and showed that the **TPE-2OMe** non-radiatively deactivated to the ground state at CI [$\theta(C_2C_3C_4C_5) \approx 90°$], followed by a rotational pathway on the central C=C bond.

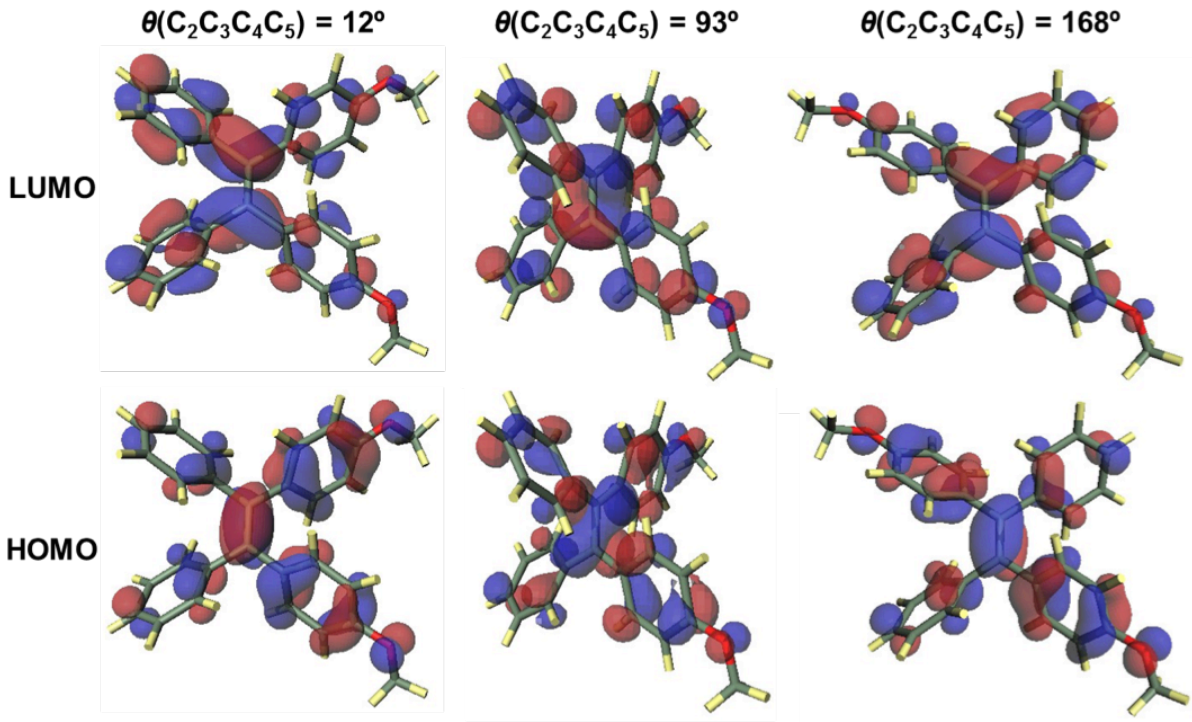

Figure 12. HOMO and LUMO of **TPE-2OMe** at $\theta(C_2C_3C_4C_5)$ = 12°, 93°, and 168°, located on the steepest-descent (SD) pathway in the S_1 state as obtained using B3LYP/def-SV(P).

Very recently, other theoretical approach had been reported. TPE derivatives having two pathways to CIs were reported in similar system; one was via C=C bond twisting, and another was via cyclization of two phenyl rings. It should be noted that simple calculation for SD pathway from the FC structures do not allow the CI structure to be obtained from the minimum of the FC state in the presence of a barrier, requiring additional calculations. Therefore, HOMO (π) and LUMO (π*) at 12°, 93°, 168° were shown in Figure 12. At the perpendicular structure at the θ = 93° (close to CI), HOMO and LUMO have almost the same structure, indicating that the S_1 and S_0 states are degenerated, in addition, the HOMO and LUMO energies are close to each other compared to the energy at S_0min. These results indicate the TPE derivatives go through nonradiative decay in the solution via CI, and the π-twist including EZI should occur, similar to the experimental results described above.

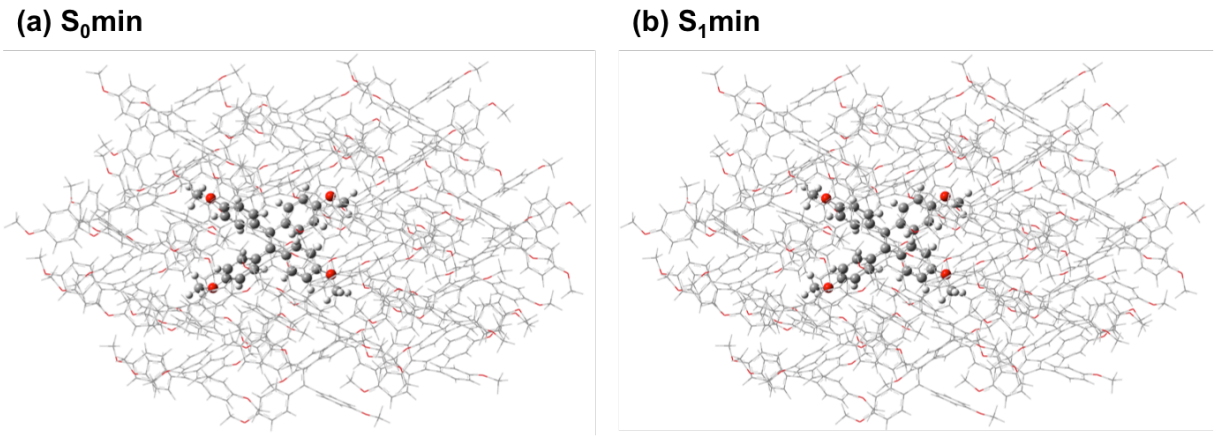

Figure 13. (a) S_0min and (b) S_1min of **TPE-4OMe** in the crystal state determined by the ONIOM method, with the high layer (ball-and-stick model) at the B3LYP/6-31+G(d) level and the low layer (stick model) at the UFF level.

Table 3. Geometrical parameters for **TPE-4OMe** in crystal at S_0min and S_1min as calculated at the B3LYP/6-31+G(d) level.

Compound	$\theta(C_2C_3C_4C_5)$ [°]		$\theta(C_1C_2C_3C_4)$ [°]		$C_3=C_4$ [Å]		$C_2=C_3$ [Å]	
	S_0min	S_1min	S_0min	S_1min	S_0min	S_1min	S_0min	S_1min
TPE-4OMe (in crystal)	175	167	63	45	1.366	1.440	1.496	1.445

To discuss an emission from TPE derivatives at the aggregated or crystalline state, the theoretical computations of **TPE-4OMe** in the crystalline state were performed on the basis of the crystal structure of **TPE-2OMe**. In the calculation, 30 molecules were extracted from the experimentally obtained crystal structure and the central molecule was treated as a higher layer at the B3LYP/6-31+G(d) level, while the surrounding 29 molecules were treated as a lower layer at the Universal Capacity Field (UFF) level by the ONIOM method (Figure 13). According to the structural optimization, the dihedral angle $\theta(C_2C_3C_4C_5)$ at the S_0min was calculated to be 175°, which is similar value in the solution (167°). In contrast, the $\theta(C_2C_3C_4C_5)$ at the S_1min was calculated to be 167°, which is almost the same in the S_0min. On the other hand, the dihedral angle $\theta(C_1C_2C_3C_4)$ showed similar variation (63° at S_0min → 45° at S_0min) compared to that in the solution. These results indicated that access to the CI was strictly inhibited by the surrounding molecules in the crystal.

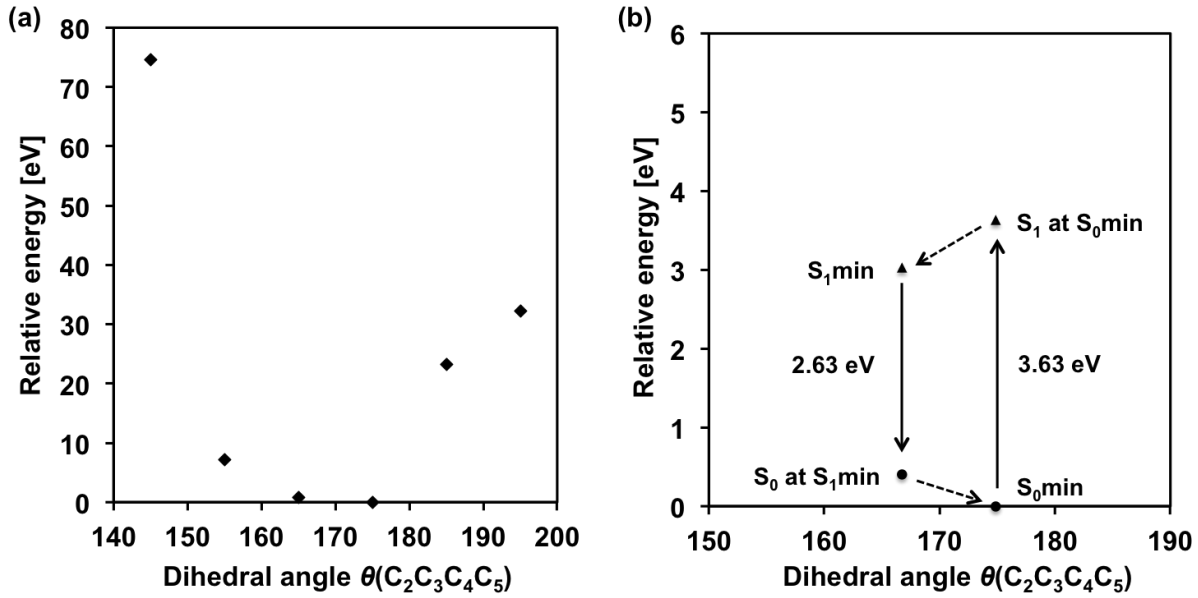

Figure 14. (a) The calculated relative energies of **TPE-4OMe** as a function of $\theta(C_2C_3C_4C_5)$ (175° at S_0min) in crystal in the S_0 state. (b) The calculated relative energies along the radiative decay pathway of **TPE-4OMe** in crystal.

Indeed, when the calculations were performed with $\theta(C_2C_3C_4C_5)$ fixed from 140° to 200°, the total energy increased sharply with only a 10° or 20° rotation (Figure 14a), indicating severe restriction of π-twist of the central molecule. Although the rotations of the phenyl rings in the excited state were also restricted [$\Delta\theta(C_1C_2C_3C_4)$ = 18°], I could conclude that the restriction of π-twist in the crystal mainly dominated the AIE behavior [$\Delta\theta(C_2C_3C_4C_5)$ = 56°]. Furthermore, the S_0 state at the S_1min was 2.63 eV lower than the S_1 state at the S_1min. The calculated energy between those two states was well corresponded to the experimental value (442 nm), validating their calculations.

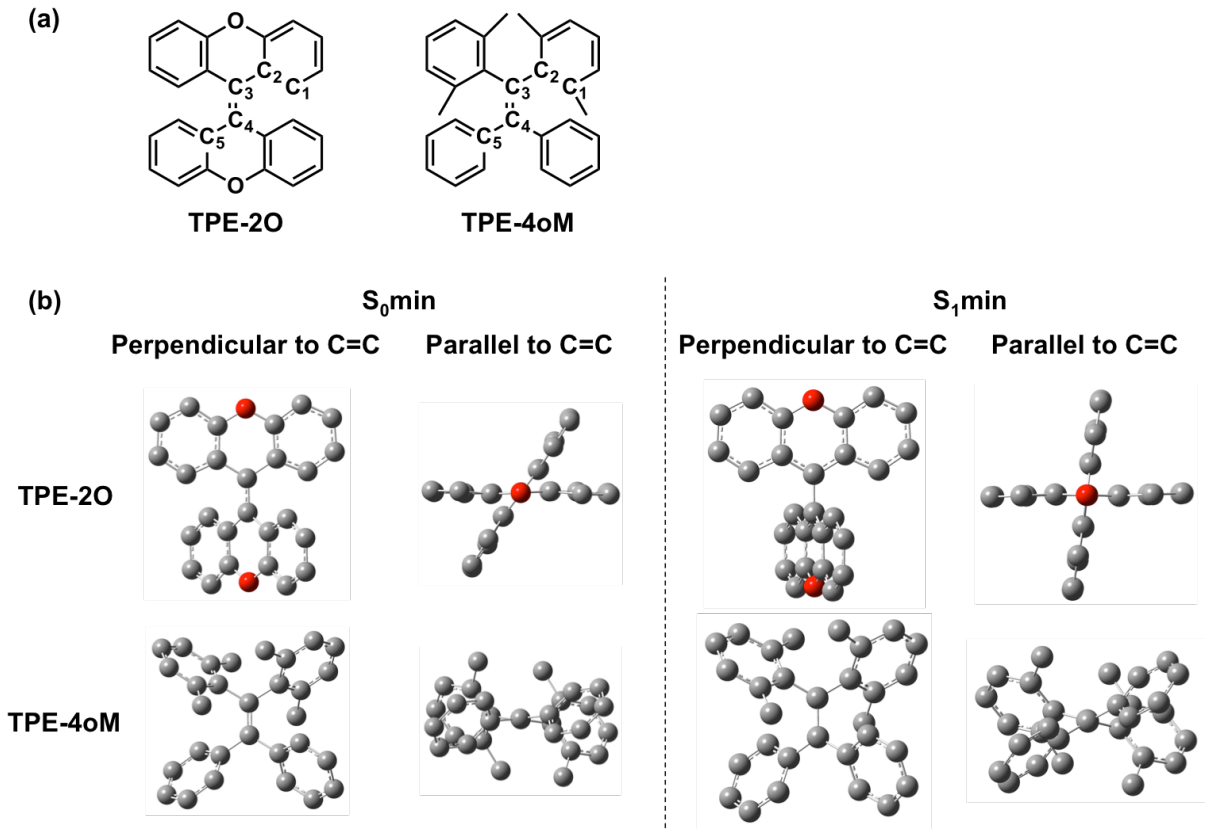

Figure 15. (a) Chemical structures of **TPE-2O** and **TPE-4oM**. (b) S_0min and S_1min structures of **TPE-2O**, **TPE-4oM** in solution ($CHCl_3$) as obtained using the polarizable continuum model (PCM) with density functional theory (DFT) and time-dependent DFT (TDDFT) at the B3LYP/6-31+G(d) level using Gaussian 16.

Table 4. Geometrical parameters for **TPE-2O** and **TPE-4oM** at S_0min and S_1min as calculated at the B3LYP/6-31+G(d) level.

Compound	$\theta(C_2C_3C_4C_5)$ [°]		$\theta(C_1C_2C_3C_4)$ [°]		$C_3=C_4$ [Å]		$C_2=C_3$ [Å]	
	S_0min	S_1min	S_0min	S_1min	S_0min	S_1min	S_0min	S_1min
TPE-2O	130	106	9	−1	1.415	1.486	1.470	1.435
TPE-4oM	167	136	59	43	1.370	1.468	1.511	1.467

My hypothesis that π-twist mainly affects the efficient quenching of AIEgen in the solution is supported by other AIE-inactive TPE derivatives. For example, it is known that **TPE-2O** (Figure 15) is AIE-inactive; emissive both in the solution and at the aggregated state.[44] In the S_0 state, **TPE-2O** has fully twisted structure due to the strongly anchored phenyl rings, thus it cannot be accompanied by the large structural change due to photoexcitation. In addition, tetra-ortho-substituted TPE (**TPE-4oM**, Figure 15) was reported to be AIE-inactive.[45] According to the calculations, the $\Delta\theta(C_2C_3C_4C_5)$ of **TPE-4oM** is lower than that of AIE-active TPE derivatives (**TPE-2OMe**, **TPE-2F**), which is due to its steric hindrance. These results also suggest the importance of π-twist in the excited state in solution for AIEgens and related compounds.

Conclusion

This chapter described the relationship between C=C bond twisting (π-twist) of TPE and AIE behavior. Some photoexperiments of di-substituted TPE derivatives revealed that TPE showed photoisomerization behavior in the diluted solution, although the photoisomerization was restricted in the solid state. According to the theoretical computations, in the diluted solution, the twisted structure of C=C bond was stable in the excited state, and the nonradiative deactivation was accelerated in the twisted structure. However the calculations in the crystalline state using ONIOM method revealed that the restriction of π-twist played more important role than that of rotations of phenyl rings in the AIE behavior. Furthermore, the hypothesis π-twist played crucial role in the AIE effect was also appreciable to the AIE-inactive molecules. These results will not only allow for the rational molecular design of TPE derivatives, but also help to elucidate the mechanisms of AIE molecules other than TPE derivatives.

Experimental Section

Materials and Measurements. All other reagents were obtained from commercial sources and used without further purification. The reaction was carried out under nitrogen atmosphere. ^{1}H (500 MHz) and ^{13}C (126 MHz) NMR measurements were recorded on a Bruker Biospin AVANCE DRX500 instrument, using 0.05% tetramethylsilane (TMS) as an internal standard. Photoirradiation was carried out using USHIO Deep UV lamp UXM-500SX with band-pass filter (AGC Asahi Glass UV-D33S), or room light. UV-Vis spectra were recorded on a JASCO V-570 spectrophotometer. Emission spectra were obtained with SHIMADZU RF5300PC spectrofluorometer. The absolute luminescence quantum yield (ΦF) was measured by a Hamamatsu C9920-02 absolute photoluminescence quantum yield measurement system equipped with an integrating sphere apparatus and a 150W continuous-wave xenon light source. Differential Scanning Calorimetry (DSC) was conducted by METLLER TOLEDO DSC1 Star System with heating rate of 10 °C /min under nitrogen atmosphere. X-ray diffraction (XRD) patterns were obtained by using a Bruker D8Advance / D with Cu Kα radiation source (40 kV, 40mA). Atmospheric pressure chemical ionization mass spectroscopy (APCI-MS) and Electron ionization mass spectroscopy (EI-MS) was carried out at Global Facility Center, Hokkaido University.

Photoirradiation

Deep UV lamp: Disubstituted TPE was dissolved in $CDCl_3$, and first isomer ratio of disubstituted TPE was determined by integral ratio of ^{1}H NMR spectra. After 1h photoirradiation was carried out using deep UV lamp, isomer ratio was determined in the same way. The same procedure was repeated several hours later.

Room light: Photoirradiation was carried out by leaving the sample under room light.

Dark: Photoirradiation was not carried out and disubstituted TPE solution was covered with aluminum foil.

Solid: Photoirradiation by deep UV lamp was carried out at solid state. The energy density was measured by THORLABS PM100D digital power meter equipped with S310C thermal sensor.

Synthetic procedure and characterization.

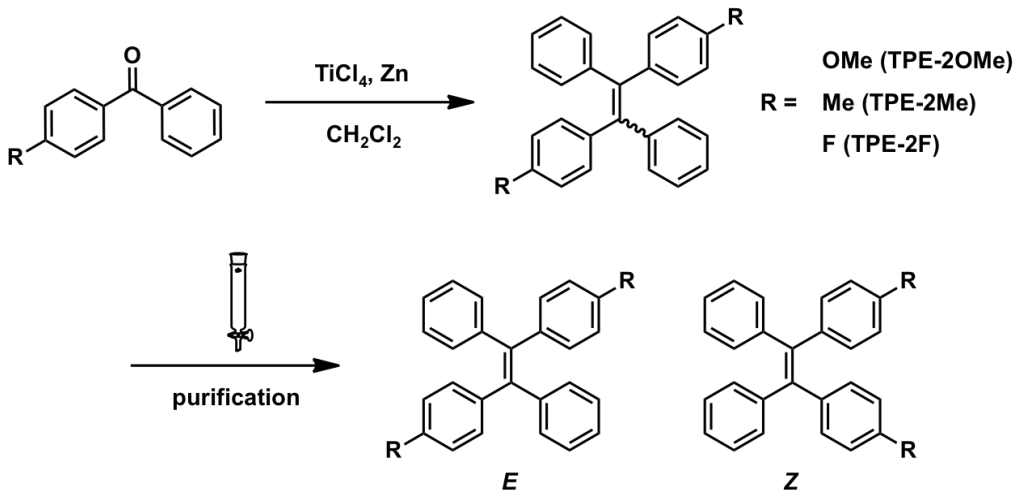

Scheme 1. Synthetic route for di-substituted TPE.

In a 300 mL three necked flask, zinc powder (1.16 g, 17.7 mmol) THF (35 mL), pyridine (0.59 mL) were added. After cooling the solution to 0 °C, 1M $TiCl_4/CH_2Cl_2$ solution (9 mL, 9 mmol) was added. Then mono-substituted benzophenone (2.00 g, 8.26 mmol) in anhydrous THF (25 mL) and CH_2Cl_2 (35 mL) was added dropwise, and the resulting mixture was stirred at 60 °C for 24 h. After cooling to room temperature, the mixture was hydrolyzed by addition of aqueous K_2CO_3 solution (100 mL, 10 %) and distilled water (100 mL). After filtration and distilling off THF, the organic layer was separated and the aqueous layer was extracted with CH2Cl2. The organic layer was combined, dried over $MgSO_4$ and the solvent was removed under reduced pressure. After the purification of the crude product by flash chromatography on SiO_2 (n-hexane/$CHCl_3$), equal mixture of isomers was obtained.

TPE-2OMe: (*E*)-rich mixture was obtained by recrystallization from hexane. (*Z*)-rich mixture was obtained by silica gel column chromatography due to difference in retention time. In this system, (*E*)-rich mixture was eluted first and (*Z*)-rich mixture later eluted. ((*E*) isomer: 90 %, (*Z*) isomer: 86 %) ^{1}H NMR (500 MHz, $CDCl_3$) δ (ppm): 3.73 (3H, s), 3.75 (3H, s), 6.62 (2H, d, *J* = 8.8 Hz), 6.65 (2H, d, *J* = 8.8 Hz), 6.91 (2H, d, *J* = 8.9 Hz), 6.94 (2H, d, *J* = 8.9 Hz), 7.00-7.13 (10H, m). ^{13}C NMR (126 MHz, CDCl3) δ (ppm): 157.81, 144.17, 144.09, 139.53, 136.30, 136.24, 132.41, 132.38, 131.29, 131.26, 127.54, 127.43, 126.05, 112.97, 112.87. HRMS(APCI) Calcd. for C28H24O2 $[M+H]^+$: m/z 393.1849 Found: m/z 393.1851.

TPE-2Me: Separation of (*E*)-(*Z*) isomers was difficult due to no difference in retention time. ^{1}H NMR (500 MHz, CDCl3) δ (ppm): 2.25 (3H, s), 2.26 (3H, s), 6.89 (4H, s), 6.91 (4H, s), 6.99-7.05 (4H, m), 7.06-7.11 (6H, m). ^{13}C NMR (126 MHz, CDCl3) δ (ppm): 144.30, 141.06, 140.53, 136.04, 131.51, 131.47, 131.37, 131.31, 128.53, 128.47, 127.74, 127.68, 126.32. HRMS(APCI) Calcd. for C28H24 $[M+H]^+$: m/z 361.1951, Found: m/z 369.1950.

TPE-2F: Each isomers was separated by silica gel column chromatography due to difference in retention time. In this system, (*E*)-rich mixture was eluted first and (*Z*)-rich mixture later eluted. ((*E*) isomer: 65 %, (*Z*) isomer: 80 %) ^{1}H NMR (500 MHz, $CDCl_3$) δ (ppm): 6.76-6.84 (4H, m), 6.94-7.02 (8H, m), 7.08-7.15 (6H, m). ^{13}C NMR (126 MHz, CDCl3) δ (ppm): 143.48, 140.18, 139.63, 133.02, 132.95, 131.35, 128.05, 127.91, 126.83, 126.79, 115.02, 114.89, 114.85, 114.73. HRMS(EI) Calcd. for C26H18F2 M^+: m/z 368.1377, Found: m/z 368.1385.

References

[1] J. Mei, N. L. C. Leung, R. T. K. Kwok, J. W. Y. Lam, B. Z. Tang, *Chem. Rev.*, **2015**, *115,* 11718–11940.

[2] X. Zhang, X. Zhang, L. Tao, Z. Chi, J. Xu, Y. Wei, *J. Mater. Chem. B*, **2014**, *2*, 4398–4414.

[3] A. Qin, J. W. Y. Lam, B. Z. Tang, *Prog. Polym. Sci.*, **2012**, *37*. 182–209.

[4] Y. Hong, J. W. Y. Lam, B. Z. Tang, *Chem. Soc. Rev.*, **2011**, *40*, 5361–5388.

[5] Y. Hong, J. W. Y. Lam, B. Z. Tang, *Chem. Commun.*, **2009**, 4332–4353.

[6] Z. Zhao, C. Y. K. Chan, S. Chen, C. Deng, J. W. Y. Lam, C. K. W. Jim, Y. Hong, P. Lu, Z. Chang, X. Chen, P. Lu, H. S. Kwok, H. Qiu, B. Z. Tang, *J. Mater. Chem.*, **2012**, *22*, 4527–4534.

[7] W. Qin, J. W. Y. Lam, Z. Yang, S. Chen, G. Liang, W. Zhao, H. S. Kwok, B. Z. Tang, *Chem. Commun.*, **2015**, *51*, 7321–7324.

[8] Z. Ning, Z. Chen, Q. Zhang, Y. Yan, S. Qian, Y. Cao, H. Tian, *Adv. Funct. Mater.*, **2007**, *17*, 3799–3807.

[9] Y. Liu, Y. Tang, N. N. Barashkov, I. S. Irgibaeva, J. W. Y. Lam, R. Hu, D. Birimzhanova, Y. Yu, B. Z. Tang, *J. Am. Chem. Soc.*, **2010**, *132*, 13951–13953.

[10] N. B. Shustova, B. D. McCarthy, M. Dincă, *J. Am. Chem. Soc.*, **2011**, *133*, 20126–20129.

[11] T. Han, X. Feng, B. Tong, J. Shi, L. Chen, J. Zhi, Y. Dong, *Chem. Commun.*, **2012**, *48*, 416-418.

[12] H. Tong, Y. Hong, Y. Dong, M. Haußler, J. W. Y. Lam, Z. Li, Z. Guo, Z. Guo, B. Z. Tang, *Chem. Commun.* **2006**, 3705–3707.

[13] T. Noguchi, B. Roy, D. Yoshihara, Y. Tsuchiya, T. Yamamoto, S. Shinkai, *Chem. Eur. J.* **2014**, *20*, 381−384.

[14] D. H. Waldeck, *Chem. Rev.* **1991**, *91*, 415−436.

[15] C. Dugave, L. Demange, *Chem. Rev.* **2003**, *103*, 2475−2532.

[16] N. Koumura, R. W. J. Zijlstra, R. A. van Delden, N. Harada, B. L. Feringa, *Nature,* **1999**, *401*, 152−155.

[17] B. G. Levine, T. J. Martinez, *Annu. Rev. Phys. Chem.* **2007**, *58*, 613−634.

[18] L. K. Rothberg, M. Yan, S. Son, M. E. Galvin, E. W. Kwock, T. M. Miller, H. E. Katz, R. C. Haddon, *Synth. Met.* **1996**, *78*, 231−236.

[19] D. Oelkrug, A. Tompert, J. Gierschner, H.-J. Egelhaaf, M. Hanack, M. Hohloch, E. Steinhuber, *J. Phys. Chem. B* **1998**, *102*, 1902−1907.

[20] D. A. Whitten, *Acc. Chem. Res.* **1993**, *26*, 502−509.

[21] J. Shi, L. E. Aguilar Suarez, S.-J. Yoon, S.-J. Varghese, C. Serpa, S. Y. L. Lüer, D. Roca-Sanjuań, B. Miliań-Medina, J. Gierschner, *J. Phys. Chem. C,* **2017**, *121*, 23166−23183.

[22] S. Takeuchi, S. Ruhman, T. Tsuneda, M. Chiba, T. Taketsugu, T. Tahara, *Science,* **2008**, *322*, 1073−1077.

[23] Y. Harabuchi, K. Keipert, F. Zahariev, T. Taketsugu, M. S. Gordon, *J. Phys. Chem. A,* **2014**, *118*, 11987−11998.

[24] P. Duan, N. Yanai, Y. Kurashige, N. Kimizuka, *Angew. Chem., Int. Ed.* **2015**, *54*, 7544−7549.

[25] Y. Harabuchi, R. Yamamoto, S. Maeda, S. Takeuchi, T. Tahara, T. Taketsugu, *J. Phys. Chem. A*. **2016**, *120*, 8804−8812.

[26] P. F. Barbara, S. D. Rand, P. M. Rentzepis, *J. Am. Chem. Soc.* **1981**, *103*, 2156−2162.

[27] B. I. Greene, *Chem. Phys. Lett.* **1981**, *79*, 51−53.

[28] E. Lenderink, K. Duppen, D. A. Wiersma, *J. Phys. Chem.* **1995**, *99*, 8972−8977.

[29] R. W. J. Zijlstra, P. Th. van Duijnen, B. L. Feringa, T. Steffen, K. Duppen, D. A. Wiersma, *J. Phys. Chem. A,* **1997**, *101*, 9828−9836.

[30] J. Wang, J. Mei, R. Hu, J. Z. Sun, A. Qin, B. Z. Tang, *J. Am. Chem. Soc.* **2012**, *134*, 9956−9966.

[31] Z. Yang, W. Qin, N. L. C. Leung, M. Arseneault, J. W. Y. Lam, G. Liang, H. H. Y. Sung, I. D. Williams, B. Z. Tang, *J. Mater. Chem. C,* **2016**, *4*, 99−107.

[32] X. Fang, Y.-M. Zhang, K. Chang, Z. Liu, X. Su, H. Chen, S. X.-A. Zhang, Y. Liu, C. Wu, *Chem. Mater.* **2016**, *28*, 6628−6636.

[33] G.-J. Zhao, K.-L. Han, Y.-B. Lei, Y.-S. Dou, *J. Chem. Phys.* **2007**, *127*, 094307.

[34] Y-J Gao, X.-P Chang, X.-Y. Liu, Q.-S. Li, G. Cui, W. Thiel, *J. Phys. Chem. A,* **2017**, *121*, 2572−2579.

[35] A. Prlj, N. Dosl'ic C. Corminboeuf, *Phys. Chem. Chem. Phys.* **2016**, *18*, 11606−11609.

[36] C. Lee, W. Yang, R. G. Parr, *Phys*. *Rev*. *B: Condens*. *Matter Mater*. *Phys*. **1988**, *37*, 785−789.

[37] Z. Zhao, B. He, H. Nie, B. Chen, P. Lu, A. Qin, B. Z. Tang, *Chem. Commun.* **2014**, *50*, 1131−1133.

[38] M. Cossi, V. Barone, R. Cammi, J. Tomasi, *Chem. Phys. Lett.* **1996**, *255*, 327−335.

[39] A. D. Becke, *J. Chem*. *Phys*. **1993**, *98*, 5648−5652.

[40] Gaussian 16, Revision A.03, M. J. Frisch, G. W. Trucks, H. B. Schlegel, G. E. Scuseria, M. A. Robb, J. R. Cheeseman, G. Scalmani, V. Barone, G. A. Petersson, H. Nakatsuji, X. Li, M. Caricato, A. V. Marenich, J. Bloino, B. G. Janesko, R. Gomperts, B. Mennucci, H.

P. Hratchian, J. V. Ortiz, A. F. Izmaylov, J. L. Sonnenberg, D. Williams-Young, F. Ding, F. Lipparini, F. Egidi, J. Goings, B. Peng, A. Petrone, T. Henderson, D. Ranasinghe, V. G. Zakrzewski, J. Gao, N. Rega, G. Zheng, W. Liang, M. Hada, M. Ehara, K. Toyota, R. Fukuda, J. Hasegawa, M. Ishida, T. Nakajima, Y. Honda, O. Kitao, H. Nakai, T. Vreven, K. Throssell, J. A. Montgomery, Jr., J. E. Peralta, F. Ogliaro, M. J. Bearpark, J. J. Heyd, E. N. Brothers, K. N. Kudin, V. N. Staroverov, T. A. Keith, R. Kobayashi, J. Normand, K. Raghavachari, A. P. Rendell, J. C. Burant, S. S. Iyengar, J. Tomasi, M. Cossi, J. M. Millam, M. Klene, C. Adamo, R. Cammi, J. W. Ochterski, R. L. Martin, K. Morokuma, O. Farkas, J. B. Foresman, D. J. Fox, Gaussian, Inc., Wallingford CT, **2016**.

[41] A. Schaf̈er, H. Horn, R. Ahlrichs, *J. Chem. Phys.* **1992**, *97*, 2571− 2577.

[42] TURBOMOLE: Program Package for ab Initio Electronic Structure Calculations, version 7.0−7.1; TURBOMOLE GmbH: Karlsruhe, Germany, 2015−2016; available from http://www.turbomole.com (accessed Nov 15, 2017).

[43] R. Ahlrichs, M. Baẗr, M. Haš er, H. Horn, C. Kölmel, *Chem. Phys. Lett.* **1989**, *162*, 165−169.

[44] J. Shi, N. Chang, C. Li, J. Mei, C. Deng, X. Luo, Z. Liu, Z. Bo, Y. Q. Dong, B. Z. Tang, *Chem. Commun.* **2012**, *48*, 10675−10677.

[45] G.-F. Zhang, Z.-Q. Chen, M, P, Aldred, Z. Hu, T. Chen, Z. Huang, X. Meng, M.-Q. Zhu, *Chem. Commun.* **2014**, *50*, 12058−12060.

Chapter IV

The effect of crosslinking with oligo-ethyleneglycol chains to AIE behavior

Chapter IV

The effect of crosslinking with oligo-ethyleneglycol chains to AIE behavior

Abstract: This chapter describes synthesis of a series of TPE macrocycles having covalent oligo-ethyleneglycol linkage between vicinal phenyl rings with various chain lengths and the substituent positions. They were synthesized under high-diluted conditions and by slowly addition of the reagents over several hours. They exhibited different luminescent properties depending on the chain lengths, substituent positions, and *cis-trans* isomers. TPE macrocycles with shorter chains and *trans* isomers linked at the *o*-position showed fluorescence in the diluted solution, while the others showed typical AIE behavior similar to non-substituted TPE. From the theoretical computations for these molecules in the excited state, TPE macrocycles showing strong emission in the diluted solution exhibited smaller difference of the dihedral angle around the central C=C bond between in the ground and excited state, while showing no emission in the solution state exhibited larger difference.

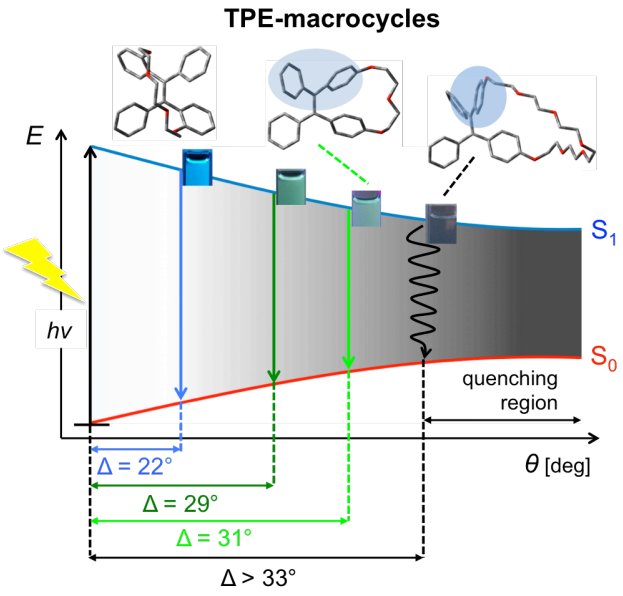

Introduction

In recent twenty years, aggregation-induced emission (AIE) have emerged as a new class of photophenomenon, in which so called AIE luminogens (AIEgens) are non-emissive in the diluted solution but is highly emissive at the aggregated state.[1-5] Since Tang *et al*. reported AIE phenomenon in silole derivative in 2001, the application for optoelectronic devices such as organic light emitting diode (OLED) has attractive attention.[6-8]

Understanding the mechanism of AIE is very important, because it should lead to the discovery of new AIEgens and the control of AIE phenomenon. In Chapter III, I demonstrated one hypothesis that the twisting of central C=C bond (π-twist) of tetraphenylethene (TPE) derivatives played a crucial role in the AIE, which was supported by some photoexperiments and theoretical computations of di-substituted TPE derivatives. This hypothesis was also supported by other researchers. For example, Shinkai *et al.* reported "cyclization-induced emission" of a TPE derivative having zinc dipicolylamine group which can interact with dicarboxylic acid.[9] Wu *et al*. synthesized emissive TPE derivatives having bisurea moiety recognizing oxoacid anions such as $PO4^{3-}$and $SO4^{2-}$.[10] Hahn *et al*. observed emission of TPE derivative tethering N-heterocyclic carbene (NHC) by interacting with metal cation.[11] Notably, in these reports, the π-twist is restricted but the phenyl rings are rotatable after supramolecular dimerization.

Very recently, the most conclusive evidence was reported by *Tang et al.* They synthesized TPE derivatives whose phenyl rings were cyclically linked by covalent bonds with rigid chains.[12] The derivatives linked at the vicinal positions of ethylene did not emit luminescence in the diluted solution, while those linked at the germinal positions became emissive even in the diluted solution. This result strongly supported the author's hypothesis that the π-twist induced the AIE phenomenon, however, the quantitative evaluation of restriction of the π-twist by the covalent linkage both in the ground state and in the excited state have not yet explored probably due to the cumbersome synthetic procedure to change the tightness of covalent linkage "fastener" bit by bit.

Herein, I synthesized a series of TPE macrocycles in which the vicinal phenyl rings were covalently linkage by flexible oligoethyleneglycol (OEG) chains with different chain lengths and linkage positions. In this system, the effect of the tightness of linkage to AIE phenomenon can be investigated in detail because the tightness of OEG chains varied dependent on the chain lengths and linkage positions. This research will provide a new perspective for the origin of AIE property and a rational molecular design for a novel TPE macrocycles.[13]

Results and Discussion

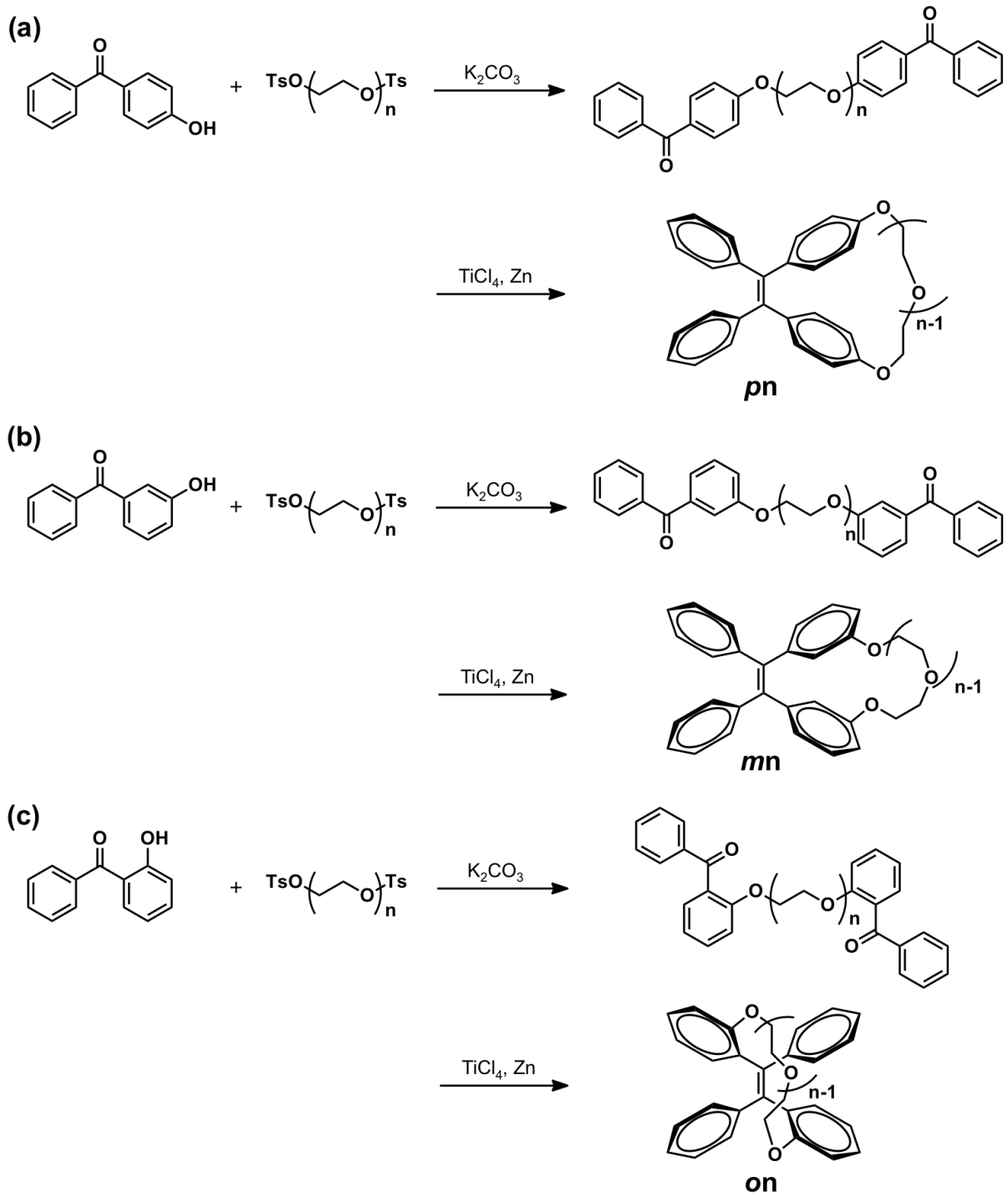

Figure 1. Synthetic route for (a) ***p*n** (n = 2-6), (b) ***m*n** (n = 2-6), and (c) ***o*n** (n = 3,4).

A series of TPE macrocycles [***p*n** (n = 2-6), ***m*n** (n = 2-6), ***o*n** (n = 3,4)] were synthesized by intramolecular Mcmurry coupling from the corresponding OEG-linked benzophenone dimers that are obtained by Williamson ether synthesis (Figure 1). To promote intramolecular reaction rather than intermolecular reaction, the reagent solution was added slowly in a dropwise manner under a high diluted condition to the reaction mixture over 6 h. ^{1}H NMR, ^{13}C NMR spectroscopies, and high solution mass spectroscopy (HRMS) revealed the formation of TPE macrocycles. The results of HRMS indicated suggested that the intramolecular cyclic compounds were obtained instead of the cyclic polymers. According to the NMR studies, all TPE macrocycles consisted of one isomer, except for ***o*4**. The NMR spectrum of ***o*4** suggested the presence of two isomers in a ratio of 89/11, and the major isomer was isolated by silica gel column chromatography.

Table 1. Energy difference between *cis* and *trans* isomers.

Compound	isomer	$E_{trans} - E_{cis}$ [eV]
***p*2**	*cis*	-[a]
***p*3**	*cis*	-[a]
***p*4**	*cis*	0.70
***p*5**	*cis*	0.42
***p*6**	*cis*	0.31
***m*2**	*cis*	0.49
***m*3**	*cis*	0.49
***m*4**	*cis*	0.30
***m*5**	*cis*	0.21
***m*6**	*cis*	0.16
***o*3**	*trans*	−0.40
***o*4**	*cis* (major)	−0.007

[a] The energy of *trans* isomer was not obtained due to high instability.

To determine the stability between *cis* and *trans* isomers of TPE macrocycles were obtained, the energy differences between *cis* and *trans* isomers in the ground states were calculated by density functional theory (DFT) method at the B3LYP/6-31G(d) level using Gaussian 16. According to the calculations, for ***p*2**-***p*6** and ***m*2**-***m*6**, *cis* isomers were much more thermodynamically stable than the *trans* isomers. In particular, the calculations of *trans* isomer of ***p*2** and ***p*3** were not converged due to its too high energy (Table 1). On the other hand, the *trans* isomer of ***o*3** was found to be more stable than the *cis* isomer, and almost no energy difference was observed in the isomers of ***o*4**, which corresponded to the NMR results that isomeric mixtures were obtained.

Table 2. Summary of crystallographic data.

Identification code	***p*3**	***m*2**
Empirical formula	$C_{64}H_{60}O_8$	$C_{30}H_{26}O_3$
Formula weight	957.12	434.51
Temperature (K)	193(2)	193(2)
Crystal system	Triclinic	Monoclinic
Space group	*P*-1	$P2_1/c$
a (Å)	13.9927(3)	13.49730(10)
b (Å)	13.9930(4)	8.90620(10)
c (Å)	14.3817(4)	19.1393(2)
α(°)	74.428(2)	90
β(°)	74.344(2)	90.6610(10)
γ(°)	71.519(2)	90
Volume (Å^3)	2519.52(11)	2300.58(4)
Z	2	4
Calculated density (g/cm^3)	1.262	1.254
Absorption coefficient (mm^{-1})	0.653	0.630
F(000)	1016	920
Reflections collected / unique	17346 / 9007 [R_{int} = 0.0160]	16678 / 4690 [R_{int} = 0.0233]
Completeness to theta = 77.40	84.0%	96.0%
Goodness-of-fit on F^2	1.016	1.052
Final *R* indices [I>2sigma(I)]	R_1 = 0.0744, wR_2 = 0.2159	R_1 = 0.0513, wR_2 = 0.1331
R indices (all data)	R_1 = 0.0790, wR_2 = 0.2206	R_1 = 0.0539, wR_2 = 0.1354

Table 3 (*continued*). Summary of crystallographic data.

Identification code	***o*3**	***o*4 (*cis*)**
Empirical formula	$C_{33}H_{34}O_5$	$C_{34}H_{34}O_5$
Formula weight	510.60	522.61
Temperature (K)	293(2)	293(2)
Crystal system	Triclinic	Triclinic
Space group	*P*-1	*P*-1
a (Å)	10.8265(3)	9.6286(3)
b (Å)	11.5183(3)	10.0918(3)
c (Å)	12.4106(3)	15.5411(3)
α(°)	78.076(2)	78.560(2)
β(°)	66.748(2)	82.821(2)
γ(°)	85.843(2)	67.359 (3)
Volume ($Å^3$)	1391.18(6)	1364.09(6)
Z	2	2
Calculated density (g/cm^3)	1.219	1.272
Absorption coefficient (mm^{-1})	0.648	0.674
F(000)	544	556
Reflections collected / unique	18129 / 5646 [R_{int} = 0.0223]	14953 / 5492 [R_{int} = 0.0265]
Completeness to theta = 76.74	96.1%	96.2%
Goodness-of-fit on F^2	1.066	1.059
Final *R* indices [I>2sigma(I)]	R_1 = 0.0676, wR_2 = 0.2012	R_1 = 0.0519, wR_2 = 0.1435
R indices (all data)	R_1 = 0.0723, wR_2 = 0.2062	R_1 = 0.0544, wR_2 = 0.1461

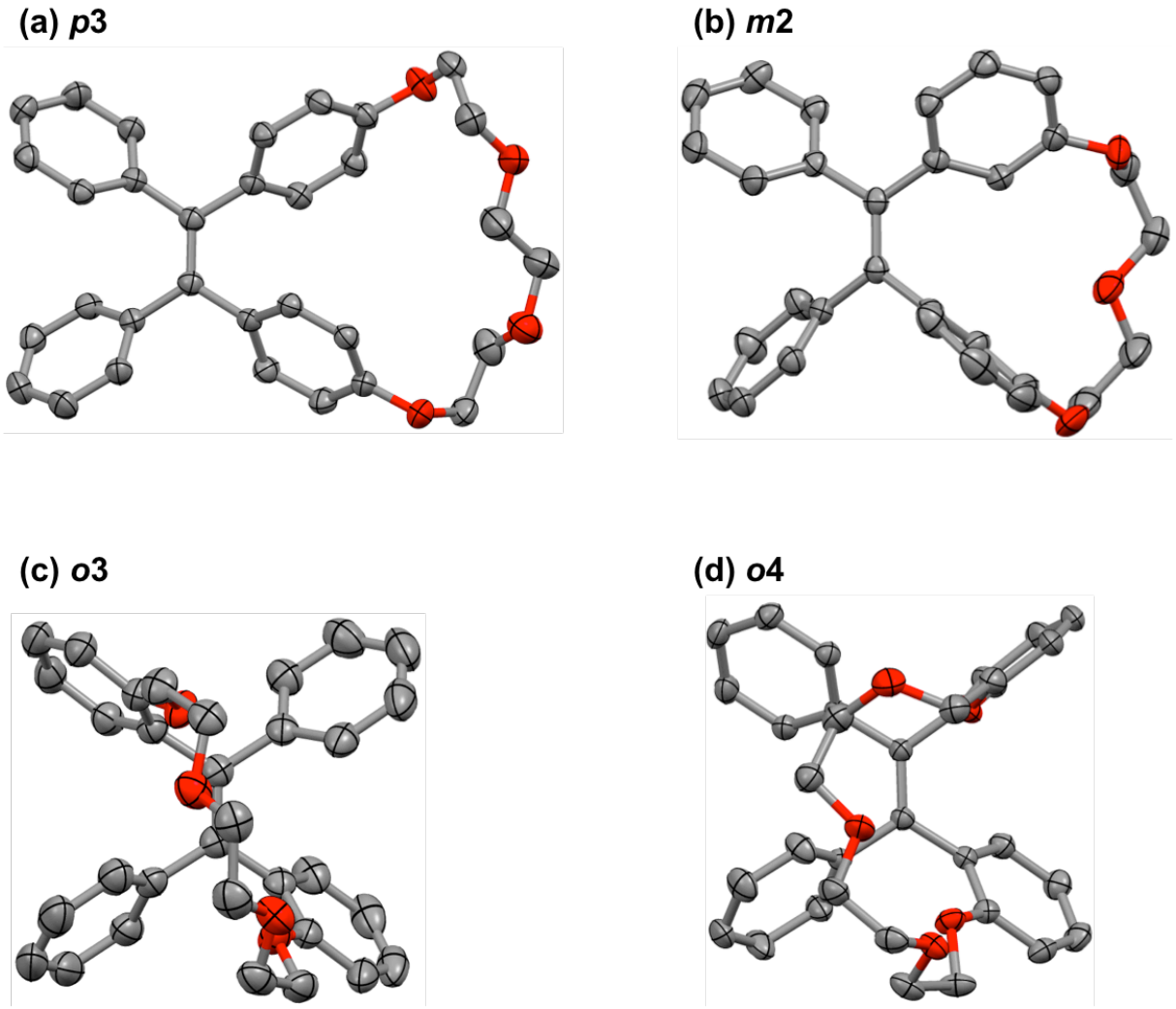

Figure 2. Crystal structures of (a) ***p*3**, (b) ***m*2**, (c) ***m*3**, and (d) ***o*4**. Thermal ellipsoids are drawn at the 50% probability level. All hydrogen atoms were omitted for clarity.

The single crystals of ***p*3**, ***m*2**, ***o*3**, and ***o*4** could be obtained by slow evaporation. X-ray single crystal analysis revealed that the major isomers of ***p*3**, ***m*2**, and ***o*4** were *cis* isomers, while ***o*3** was *trans* isomer (Table 2, 3, and Figure 2). These observations were in a good agreement with the above calculations (Table 1).

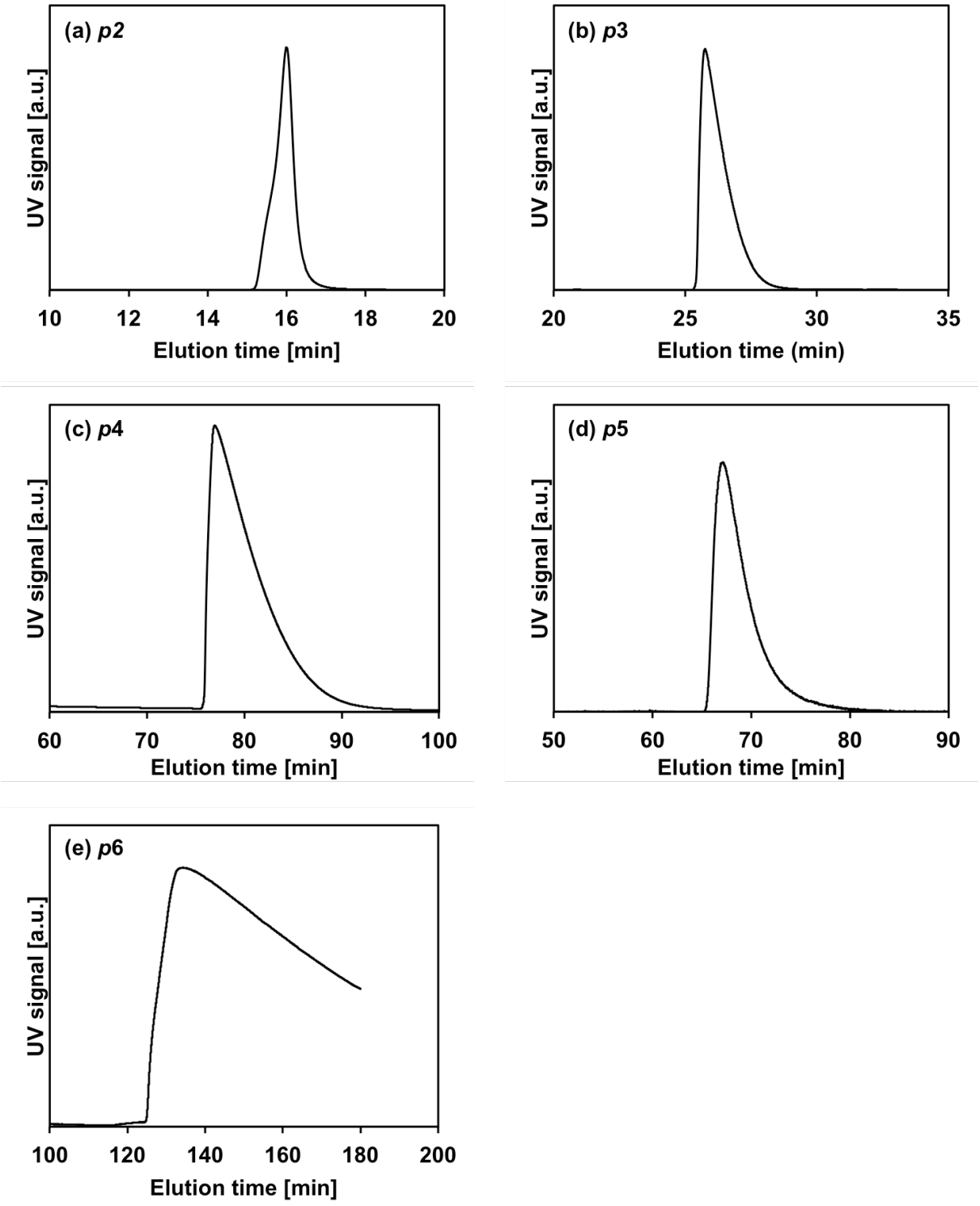

Figure 3. Chiral column chromatograms of (a) ***p*2**, (b) ***p*3**, (c) ***p*4**, (d) ***p*5**, and (e) ***p*6**.

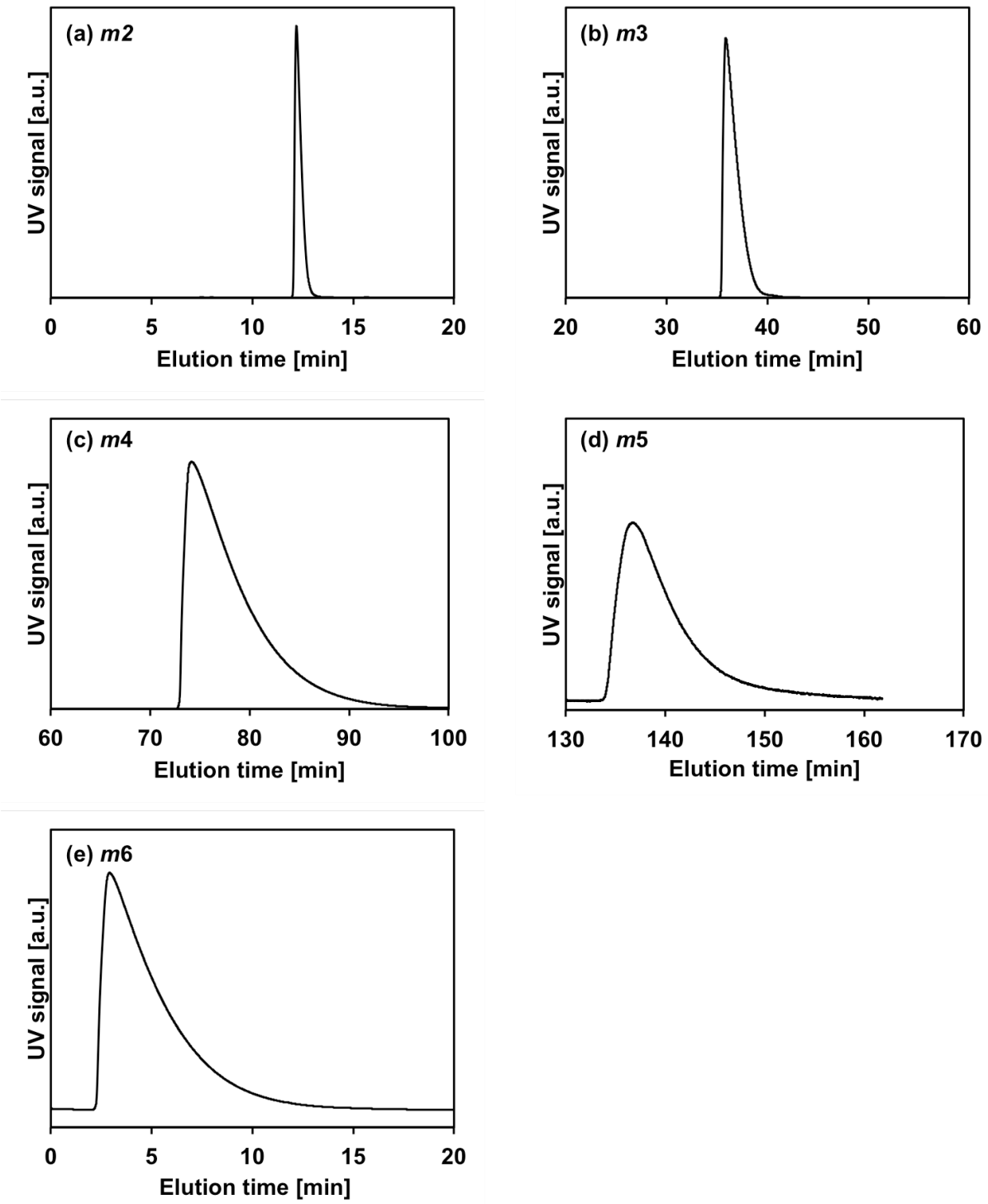

Figure 4. Chiral column chromatograms of (a) ***m*2**, (b) ***m*3**, (c) ***m*4**, (d) ***m*5**, and (e) ***m*6**.

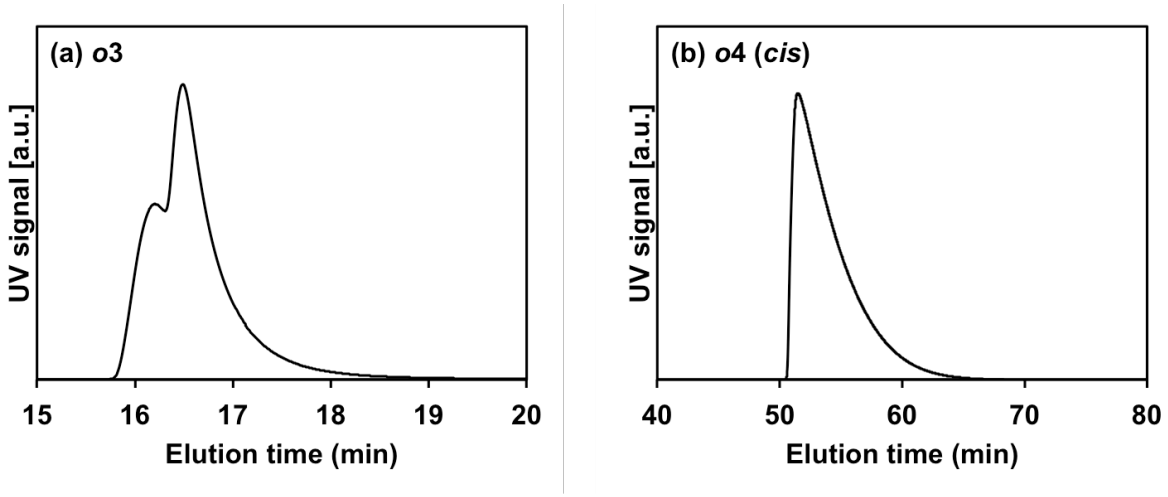

Figure 5. Chiral column chromatograms of (a) ***o*3**, (b) ***o*4**.

Considering the steric structure of the TPE macrocycles, the *trans* isomer should be racemic mixture although the *cis* isomer is meso compound. Indeed, the chiral chromatogram of obtained ***o*3** showed two peaks, suggesting it was *trans* isomer, while the chromatograms of ***p*2-6**, ***m*2-6** and major isomer of ***o*4** showed s single peak (Figure 3-5), suggesting they were *cis* isomer. The para- and meta-linkage make the formation of *cis* isomer easy because the linkage distance between phenyl rings are too long, whereas the ortho-linkage inhibit the formation of *cis* isomer due to the steric hindrance near the linkage position.

Consequently, although NMR studies did not identify which isomers of TPE macrocycles were obtained, I could concluded that the obtained ***p*2-*p*6** and ***m*2-*m*6** were *cis* isomers, the obtained ***m*3** was *trans* isomer, and major isomer of obtained ***o*4** was *cis* isomer from the energy calculations, single crystal analysis, and chiral column analysis.

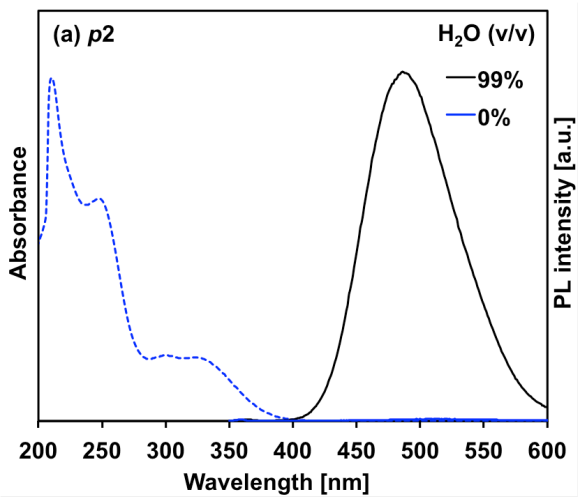

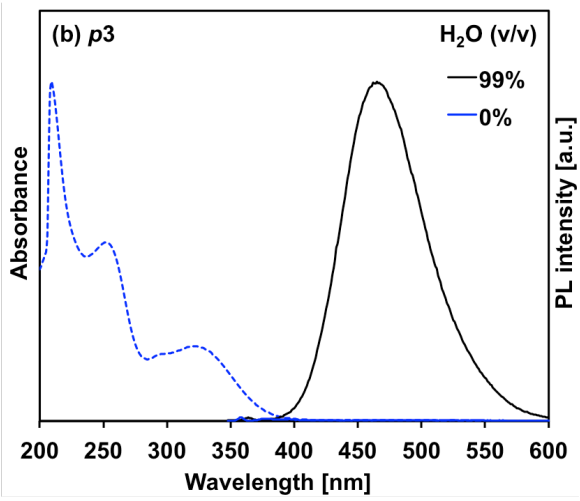

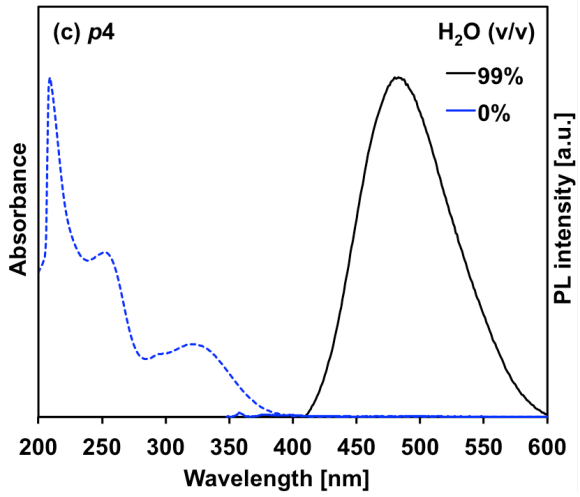

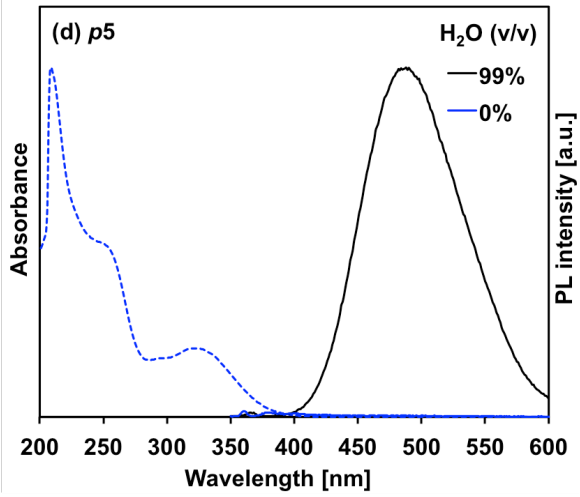

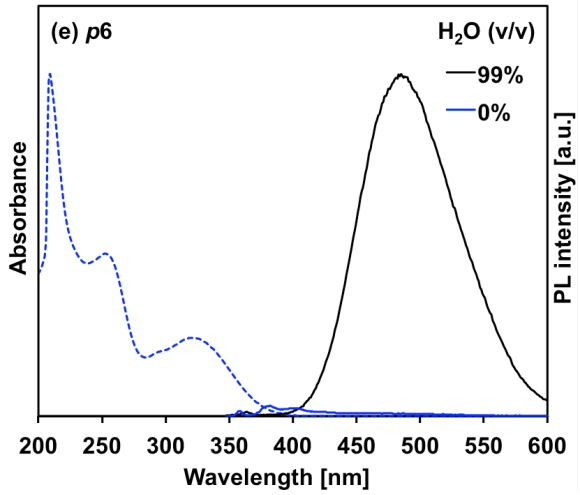

	λ_{abs} [nm][a]	$\lambda_{Em, Sol}$ [nm][b]	$\lambda_{Em, Agg}$ [nm][c]
p2	210, 247, 323	513	488
p3	209, 252, 321	-	466
p4	209, 252, 321	-	483
p5	236, 253, 323	-	488
p6	209, 253, 321	-	485

[a] Absorption maxima (THF, 10 μM). [b] Emission maxima in the solution state (THF, 10 μM). [c] Emission maxima in the aggregated state (THF/H_2O = 1/99, 10 μM)

Figure 6. UV-vis and photoluminescence (PL) spectra of ***p2***-***p6***. UV-vis spectra were measured in THF (10 μM), and PL spectra were measured in THF/H_2O mixed solvent (10 μM). Inset table shows the peak value of each spectra.

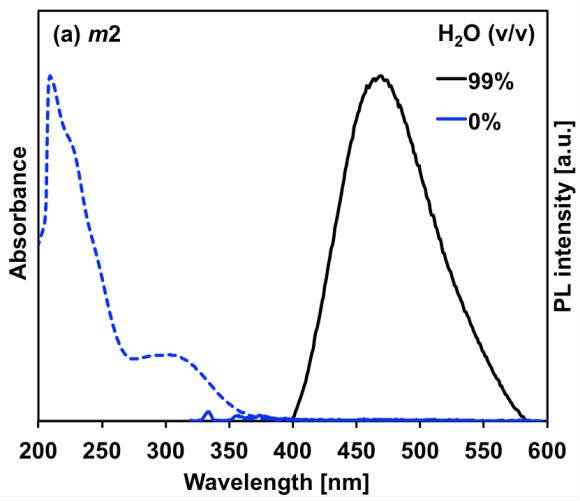

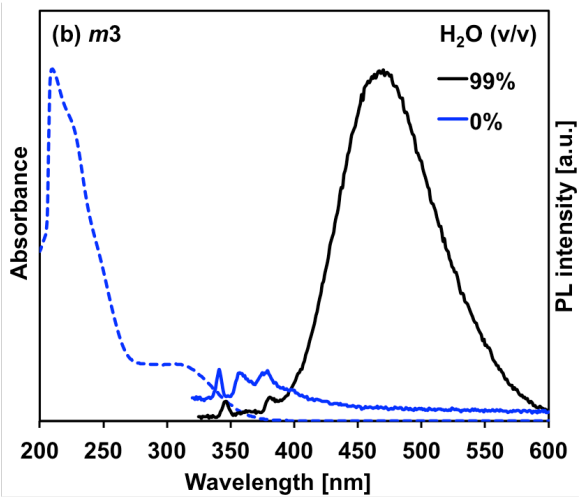

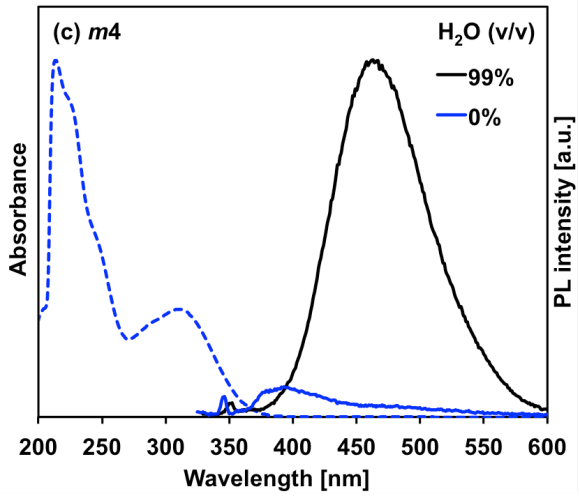

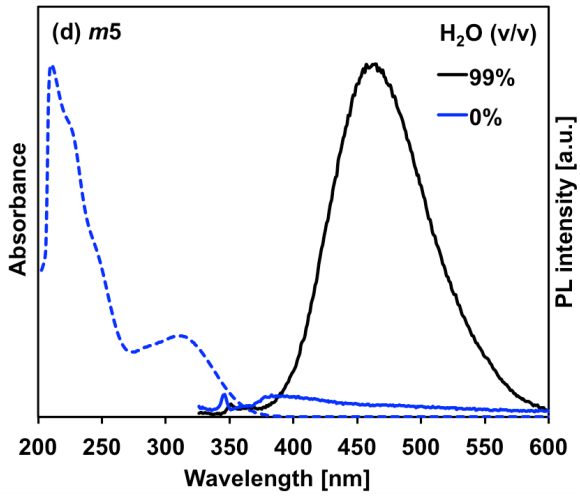

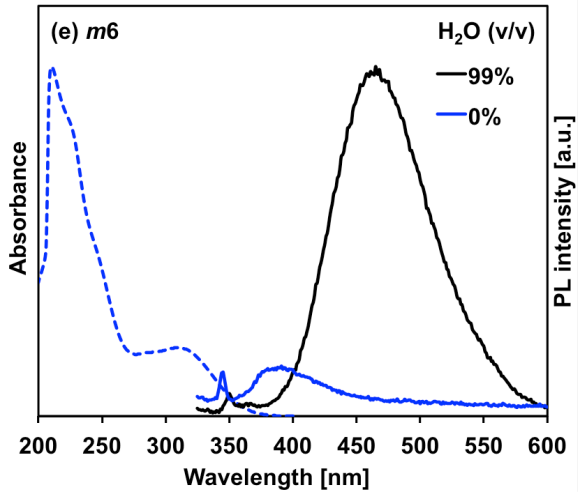

	λ_{abs} [nm][a]	$\lambda_{Em, Sol}$ [nm][b]	$\lambda_{Em, Agg}$ [nm][c]
m2	209, 302	-	469
m3	210, 306	-	467
m4	213, 310	-	463
m5	210, 310	-	464
m6	210, 309	-	465

[a] Absorption maxima (THF, 10 μM). [b] Emission maxima in the solution state (THF, 10 μM). [c] Emission maxima in the aggregated state (THF/H_2O = 1/99, 10 μM)

Figure 7. UV-vis and photoluminescence (PL) spectra of ***m2*-*m6***. UV-vis spectra were measured in THF (10 μM), and PL spectra were measured in THF/H_2O mixed solvent (10 μM). Inset table shows the peak value of each spectra.

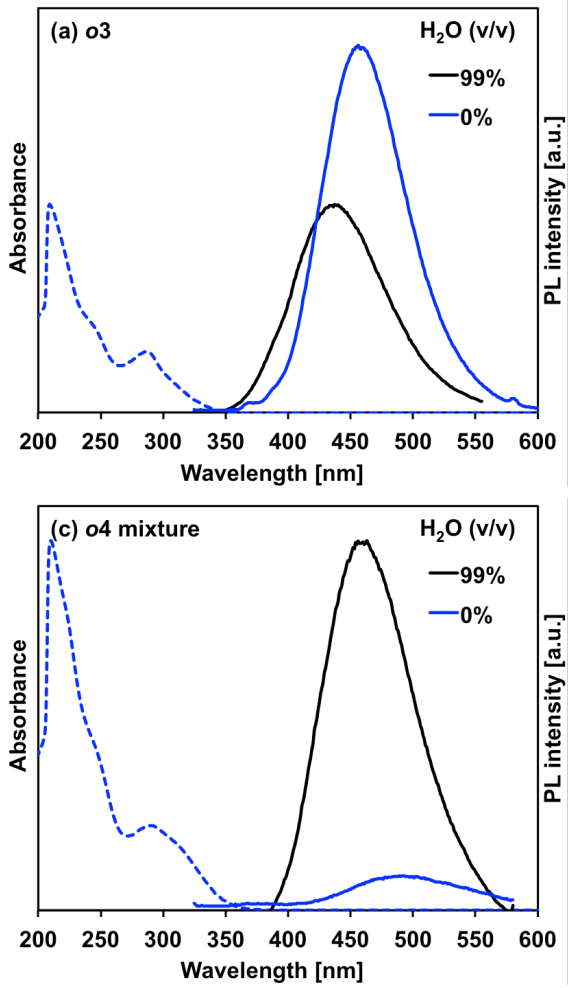

	λ_{abs} [nm][a]	$\lambda_{Em, Sol}$ [nm][b]	$\lambda_{Em, Agg}$ [nm][c]
***o*3**	209, 287	456	440
***o*4**	211, 301	-	462
***o*4 (mixture)**	210, 290	489	460

[a] Absorption maxima (THF, 10 μM). [b] Emission maxima in the solution state (THF, 10 μM). [c] Emission maxima in the aggregated state (THF/H_2O = 1/99, 10 μM)

Figure 8. (a-c) UV-vis and photoluminescence (PL) spectra of ***o*3**-***o*4**. UV-vis spectra were measured in THF (10 μM), and PL spectra were measured in THF/H_2O mixed solvent (10 μM). Inset table shows the peak value of each spectra.

All the obtained TPE macrocycles had potentially AIE property; they showed intense emission at the aggregated state prepared in a poor solvent mixture (THF/H_2O = 99/1) (Figure 6-8). According to the photoluminescence (PL) spectra in the aggregated state, the chain lengths did not affect the maximum emission wavelength ($\lambda_{Em, Agg}$), while the linkage position provided the slight differences (480-490 nm for ***p*2**-***p*6**, 460-470 nm for ***m*2**-***m*6**, and 440-460 nm for ***o*3**-***o*4**), meaning that they were mainly attributed to the electronic effect of the phenyl rings rather than the steric effect in the excited state. In addition, they are correlated to those of the absorption maxima in the solution state (λ_{Abs}), indicating that the linkage position affected the electronic effect not only in the excited state but also in the ground state.

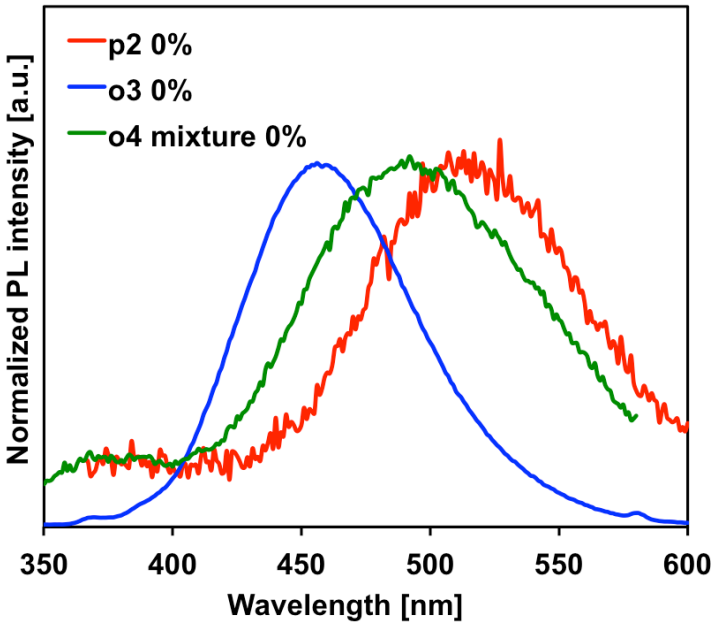

Figure 9. Normalized PL spectra of ***p*2**, ***o*3**, and ***o*4** mixture in THF (10 μM).

Notably, unlike the general TPE derivatives having AIE properties, ***p*2**, ***o*3**, and ***o*4** (mixture) showed emission even in the solution state. The relative quantum yields (Φ_f) of ***p*2**, ***o*3**, and ***o*4** (mixture) were 0.0023, 0.30, and 0.016, respectively. For ***o*4**, the mixture was emissive but isolated pure ***o*4** (*cis*-isomer) was non-emissive, therefore *trans*-isomer appeared to be emissive. Although several groups reported that formation of supramolecular complexes and covalent crosslinking made TPE derivatives emissive, this experimental result suggested that "tight" linkage was necessary for making emissive TPE derivatives in the solution.

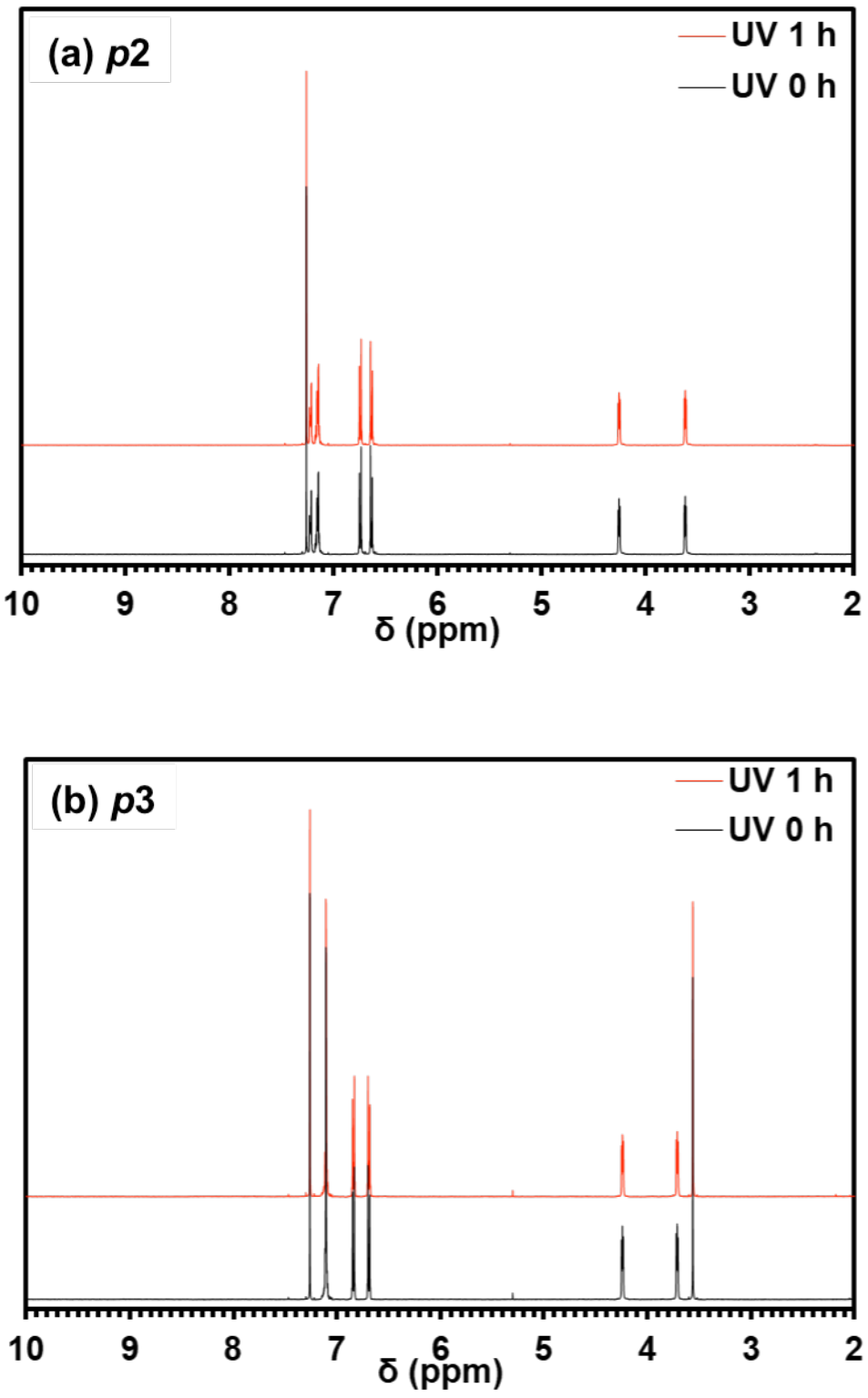

Figure 10. ^{1}H NMR spectra of (a) ***p*2** and (b) ***p*3** upon photoirradiation.

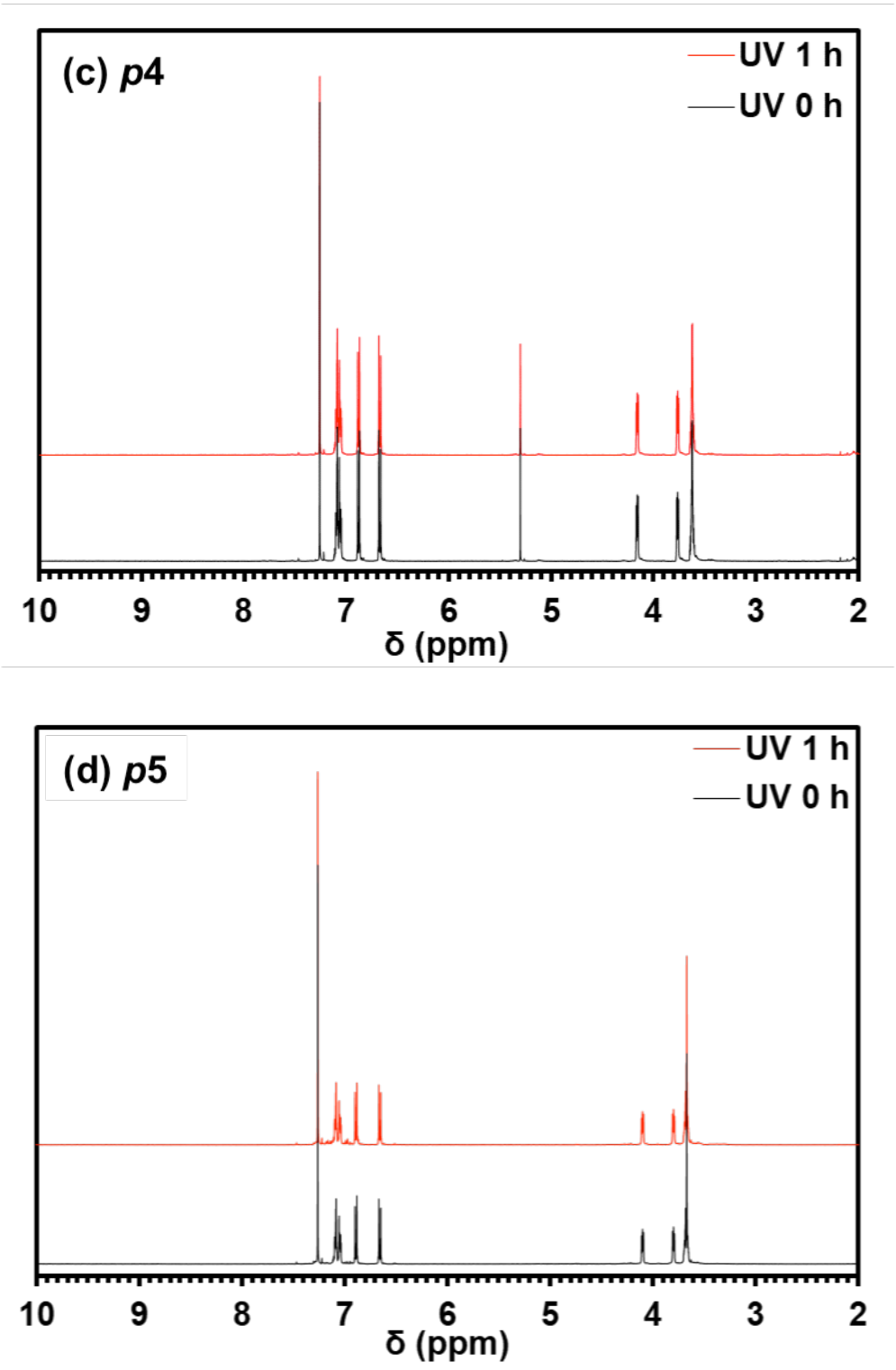

Figure 10 (*continued*). ^{1}H NMR spectra of (c) ***p*4** and (d) ***p*5** upon photoirradiation.

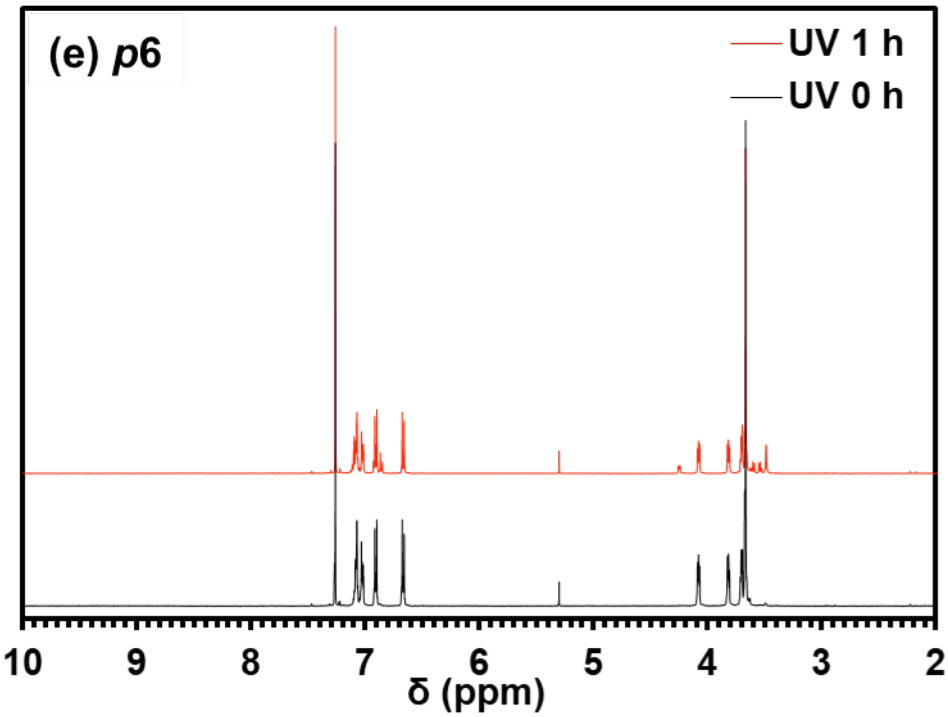

Figure 10 (*continued*). ^{1}H NMR spectra of (e) ***p*6** upon photoirradiation.

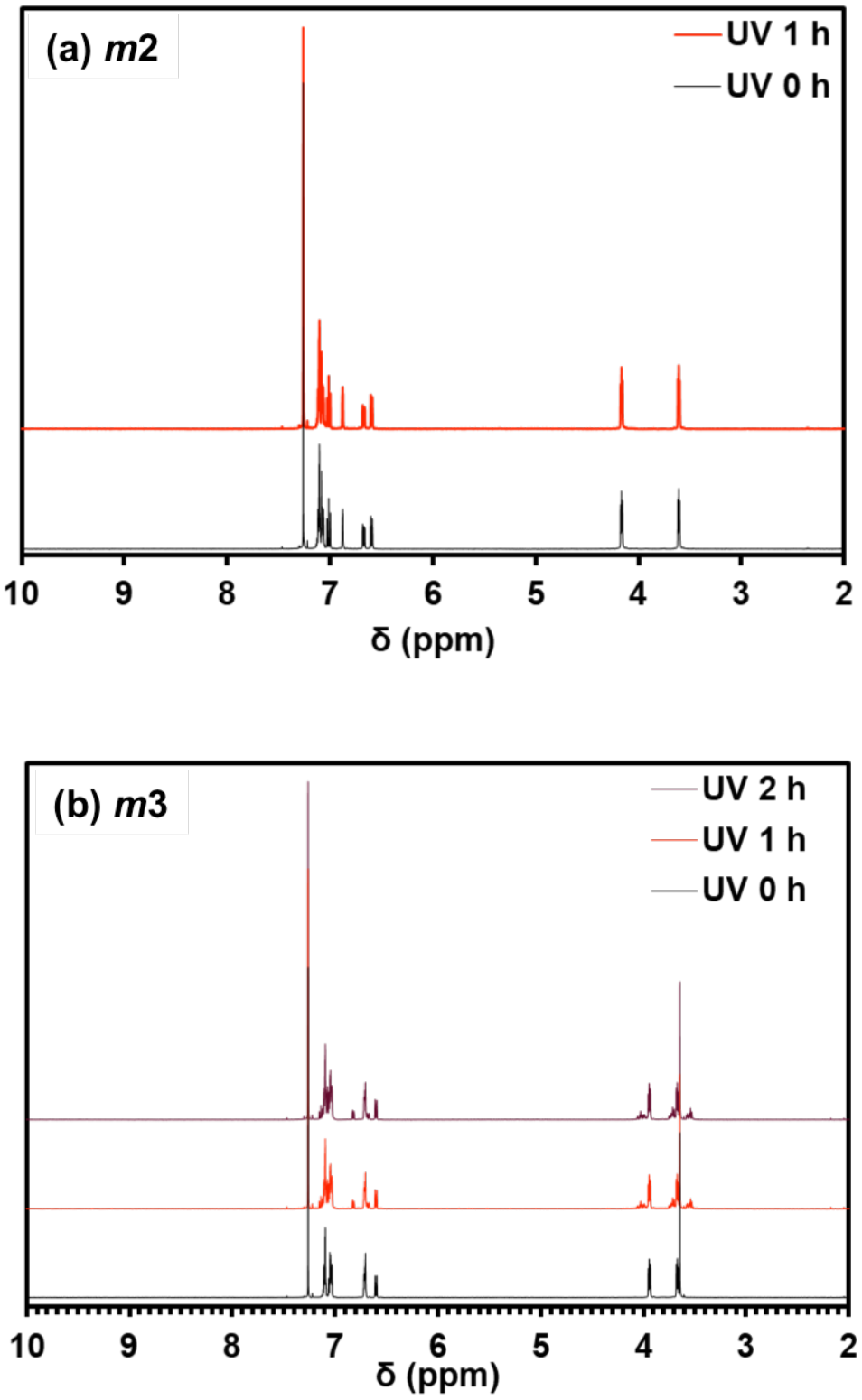

Figure 11. ^{1}H NMR spectra of (a) ***m2*** and (b) ***m3*** upon photoirradiation.

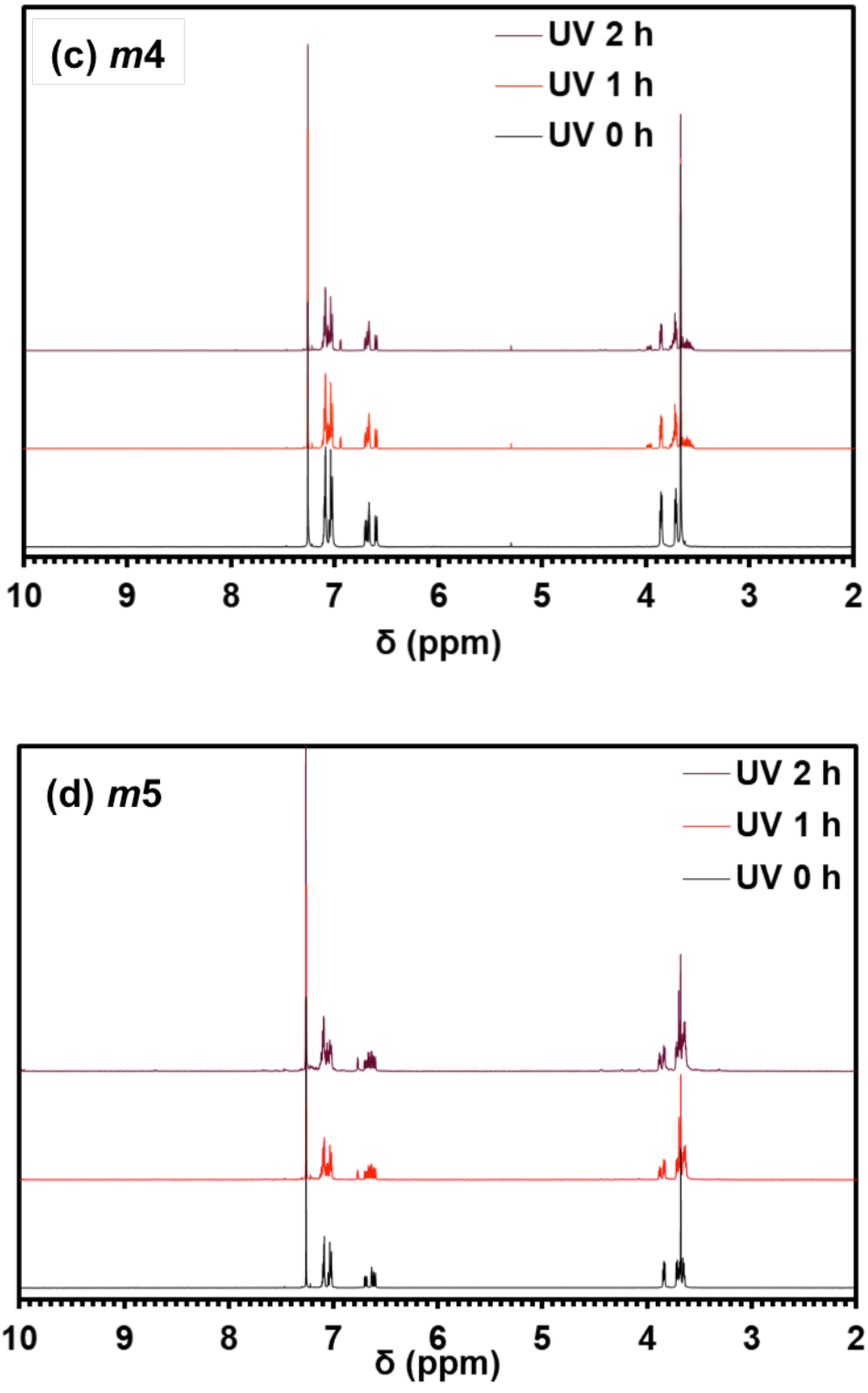

Figure 11 (*continued*). ^{1}H NMR spectra of (c) ***p*4** and (d) ***p*5** upon photoirradiation.

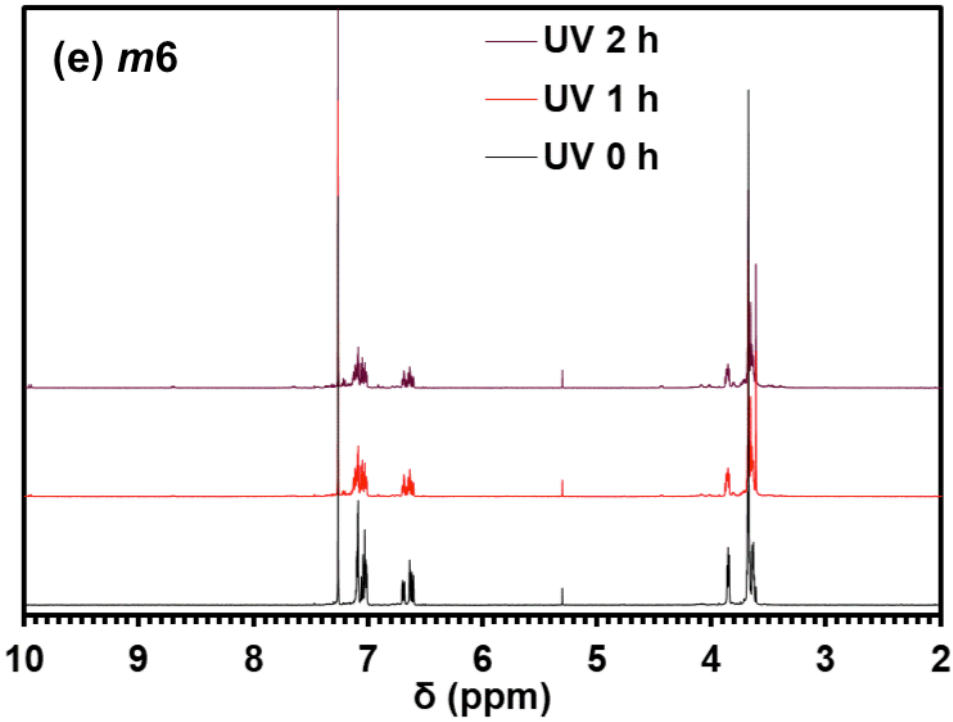

Figure 11 (*continued*). ^{1}H NMR spectra of (e) ***m*6** upon photoirradiation.

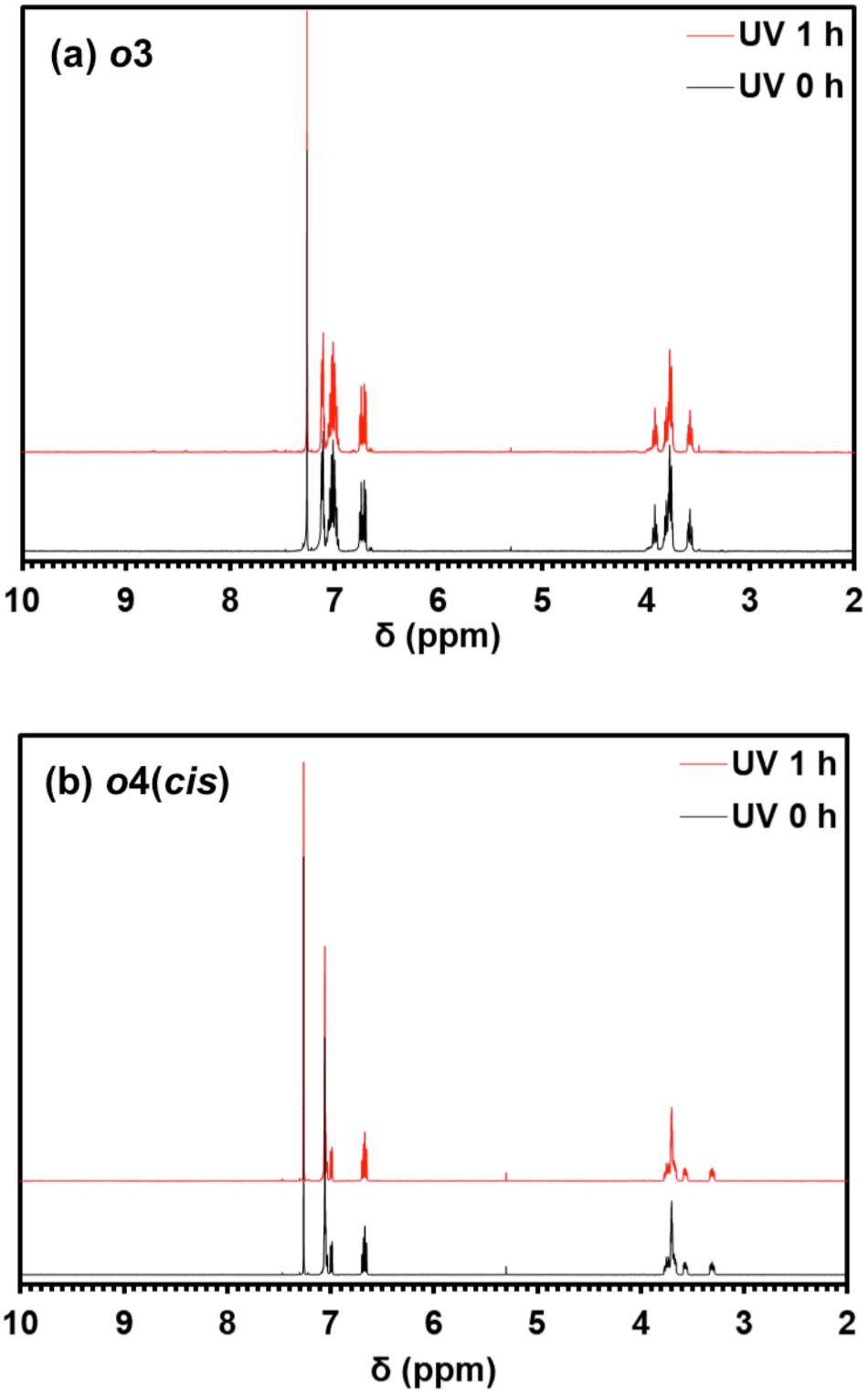

Figure 12. ^{1}H NMR spectra of (a) ***o*3** and (b) ***o*4** (*cis*) upon photoirradiation.

Among the non-emissive TPE macrocycles, ***p*6** and ***m*3**-***m*6** showed certain change in ^{1}H NMR spectra after 1 h photoirradiation (Figure 11 and 12), indicating that the photoreaction occurred (yields, ***p*6**: 20%, ***m*3**: 29%, ***m*4**: 29%, ***m*5**: 35%, ***m*6**: 48%), while the spectra of others did not change by photoirradiation. From the spectra of ***p*6** and ***m*3**-***m*6** upon photoirradiation, I could not observe peaks around 2-3 ppm or 9 ppm, which were attributed to dihydrophenanthrene[14] and phenanthrene derivatives[15] generated by photocyclization. Therefore, I concluded that the products obtained with photoreaction were *trans*-isomers of ***p*6** and ***m*3**-***m*6**. This observation suggested loose linkage could not inhibit the (*E*)-(*Z*) photoisomerization, and indeed, the yield of the photoisomerization was higher for large TPE macrocycles having the looser linkage.

Table 4. The calculated dihedral angle (θ_β) for TPE macrocycles at S_0min and S_1min at the B3LYP/6-31G(d) level.

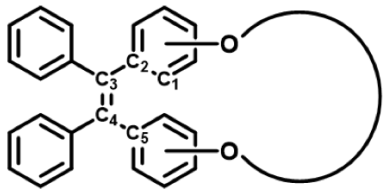

$\theta_\beta = \theta(C_2C_3C_4C_5)$

Compound	$\theta_{\beta, S0}$ [°][a]	$\theta_{\beta, S1}$ [°][b]	$\Delta\lvert\theta_{\beta, S1}-\theta_{\beta, S0}\rvert$ [°]
***p*2**	11	42	31
***p*3**	12	45	33
***p*4**	13	55	42
***p*5**	13	51	38
***p*6**	12	53	41
***m*2**	12	84	72
***m*3**	12	90	78
***m*4**	13	91	78
***m*5**	12	96	84
***m*6**	11	95	84
***o*3** (*cis*)	8	66	58
***o*3** (*trans*)	165	143	22
***o*4** (*cis*)	9	72	61
***o*4** (*trans*)	164	135	29

[a] θ_β at S_0min. [b] θ_β at S_1min.

Table 5. The calculated dihedral angle (θ_α) for TPE macrocycles at S_0min and S_1min at the B3LYP/6-31G(d) level.

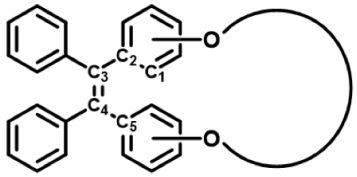

$\theta_\alpha = \theta(C_1C_2C_3C_4)$

Compound	$\theta_{\alpha, S0}$ [°][a]	$\theta_{\alpha, S1}$ [°][b]	$\Delta\lvert\theta_{\alpha, S1}-\theta_{\alpha, S0}\rvert$ [°]	C_3-C_4 [Å]		C_2-C_3 [Å]	
				S_0min	S_1min	S_0min	S_1min
***p*2**	59	34	25	1.369	1.473	1.499	1.458
***p*3**	54	30	24	1.369	1.473	1.497	1.454
***p*4**	47	16	31	1.368	1.477	1.492	1.443
***p*5**	48	19	29	1.369	1.475	1.492	1.445
***p*6**	46	16	30	1.369	1.475	1.493	1.443
***m*2**	53	12	41	1.364	1.484	1.497	1.466
***m*3**	46	3	43	1.366	1.488	1.496	1.457
***m*4**	49	8	41	1.367	1.486	1.496	1.451
***m*5**	53	10	43	1.365	1.489	1.496	1.450
***m*6**	50	8	42	1.366	1.475	1.496	1.459
***o*3** (*cis*)	83	37	46	1.360	1.485	1.504	1.452
***o*3** (*trans*)	116	135	19	1.358	1.457	1.497	1.454
***o*4** (*cis*)	67	30	37	1.361	1.487	1.500	1.448
***o*4** (*trans*)	129	140	11	1.363	1.465	1.495	1.452

[a] θ_α at S_0min. [b] θ_α at S_1min.

To obtain deeper insights into the origin of intense emission in the solution state of TPE macrocycles, I calculated optimized structure in the ground state (S_0min) and singlet excited state (S_1min) by density functional theory (DFT) and time-dependent density functional theory (TD-DFT) method at the B3LYP[16,17]/6-31G(d) level using Gaussian 16.[18] The same calculations in Chapter III were performed to all the obtained TPE macrocycles. They showed the elongation of the central C=C double bond, indicating the reduction of bond order. The dihedral angle of $C_2C_3C_4C_5$ at the S_0min ($\theta_{\beta,\,S0}$) was almost constant (8°-13°) regardless of the chain lengths and linkage positions, but that at the S_1min ($\theta_{\beta,\,S1}$) varied dependent on the chain lengths and linkage positions (Table 4). Concretely, the shorter chain lengths and the ortho-linkage roughly provided smaller $\theta_{\beta,\,S1}$ [para-: 53° (***p*6**) → 42° (***p*2**), meta-: 95° (***m*6**) → 84° (***m*2**), ortho-: 72° (***o*4** *cis*) → 66° (***o*3** *cis*)]. As the results, the difference between $\theta_{\beta,\,S1}$ and $\theta_{\beta,\,S0}$ ($\Delta|\theta_{\beta,\,S1} - \theta_{\beta,\,S0}|$) was also dependent on the chain lengths and linkage positions. In addition, the $\Delta|\theta_{\beta,\,S1} - \theta_{\beta,\,S0}|$ of *trans* isomers were significantly smaller than that of *cis* isomers [***o*3** 58° (*cis*) → 22° (*trans*), ***o*4** 61° (*cis*) → 29° (*trans*)]. As mentioned in Chapter III, the photophysical properties of the TPE derivatives were affected by twisting of the central C=C bond (π-twist). Indeed, the emissive TPE macrocycles (***p*2**, ***o*3**, ***o*4**) showed smaller $\Delta|\theta_{\beta,\,S1} - \theta_{\beta,\,S0}|$, and the order of fluorescence quantum yield [Φ_f, ***o*3** (0.30) < ***o*4** (mixture, 0.016) < ***p*2** (0.0023)] corresponded to the order of $\Delta|\theta_{\beta,\,S1} - \theta_{\beta,\,S0}|$ [***o*3** (22°) < ***o*4** (trans, 29°) < ***p*2** (31°)]. These results supported that the degree of π-twist was closely related to the photophysical properties of TPE derivatives. Note that the rotation of phenyl rings in the excited state ($\Delta|\theta_{\alpha,\,S1} - \theta_{\alpha,\,S0}|$) were mainly influenced by the linkage position (para-: 24° to 30°, meta-: 41° to 43°, ortho-: 11° to 19°) rather than the chain lengths (Table 5), meaning that the rotation of the phenyl rings in the excited state had little effect on the luminescence property.

Conclusion

This chapter described the effect of crosslinking between the two phenyl rings at vicinal position of TPE with flexible chains to the luminescent property. The TPE macrocycles linked with oligo-ethyleneglycol chains were prepared by intramolecular Mcmurry coupling that proceeded efficiently at low concentration. The chain lengths and the linkage positions significantly affected the emission properties. TPE macrocycles having shorter chains and ortho-linkage were emissive in the solution, because their linkage tightly restricted the twisting of central C=C bond of TPE in the excited state. Furthermore, *trans* isomers strongly restricted the twisting in the excited state compared to the *cis* isomer. These results, in combination with the results in Chapter II, will lead not only to develop new AIEgens but also to understand more universal photophysics, for example relationship between luminescent properties and large structural change of molecules in the excited state.

Experimental Section

Materials and Measurements. All reagents were obtained from commercial sources and used without further purification. The reaction was carried out under nitrogen atmosphere. ^{1}H (500 MHz) and ^{13}C (126 MHz) NMR measurements were recorded on a Bruker Biospin AVANCE DRX500 instrument, using 0.05% tetramethylsilane (TMS) as an internal standard. UV–vis spectra were recorded on a JASCO V-570 spectrophotometer. Emission spectra were obtained with SHIMADZU RF5300PC spectrofluorometer. X-ray diffraction (XRD) patterns were obtained by using a Bruker D8Advance / D with Cu Kα radiation source (40 kV, 40mA). Electrospray ionization mass spectroscopy (ESI-MS) was carried out at Global facility center, Hokkaido University. Chiral column chromatography was carried out on a SHIMAZU LC-9A system (DAICEL CHIRALPAK IF column) with a SHIMAZU RID-10A reflective index.

X-ray crystallography analysis. Single crystal was mounted in the loop using paraffin oil. The data were collected on a Rigaku XtaLAB Synergy-S with graphite monochromated Cu Kα radiation (λ = 1.5418 Å) and a PhotonJet-S microfocus generator operating at 50 kV and 1 mA. Diffraction data were collected and processed using the CrysAlisPro program. Structures were solved by direct methods using SHELXS.[19] Structural refinements were conducted by the full-matrix least-squares method using SHELXS.[19] Non-H atoms were refined anisotropically, and H atoms were refined using a riding model. All calculations were performed using the OLEX2[20] software packages.

Relative fluorescence quantum yields. Relative quantum yields were measured in THF or cyclohexane from the following formula(1) with corresponding 9,10-diphenylanthracene as a standard[21]. All measurements were carried out in the same experimental settings: excitation wavelength, slit widths, photomultiplier voltage.

$$\Phi_x = \Phi_{\text{std.}} \times \frac{A_{\text{std.}}}{A_x} \times \frac{F_x}{F_{\text{std.}}} \times \frac{{n_{\text{std.}}}^2}{{n_{\text{x}}}^2} \quad \cdots (1)$$

Φ: quantum yield

A: absorbance

F: integral area of emission spectrum

n: reflective index of solvent

Photoirradiation. Photoirradiation was carried out using USHIO Deep UV lamp UXM-500SX with band-pass filters (AGC Asahi Glass UV-D33S and HOYA HA50). A TPE macrocycle was dissolved in $CDCl_3$, (3 mM), and the first isomer ratio was determined by integral ratio of ^{1}H NMR. Then the photoirradiation was carried out by the deep UV lamp with setting the quartz NMR tube at 15 cm position from the lamp. Then, the second isomer ratio was determined by integral ratio of ^{1}H NMR.

Synthetic procedure and characterization.[21]

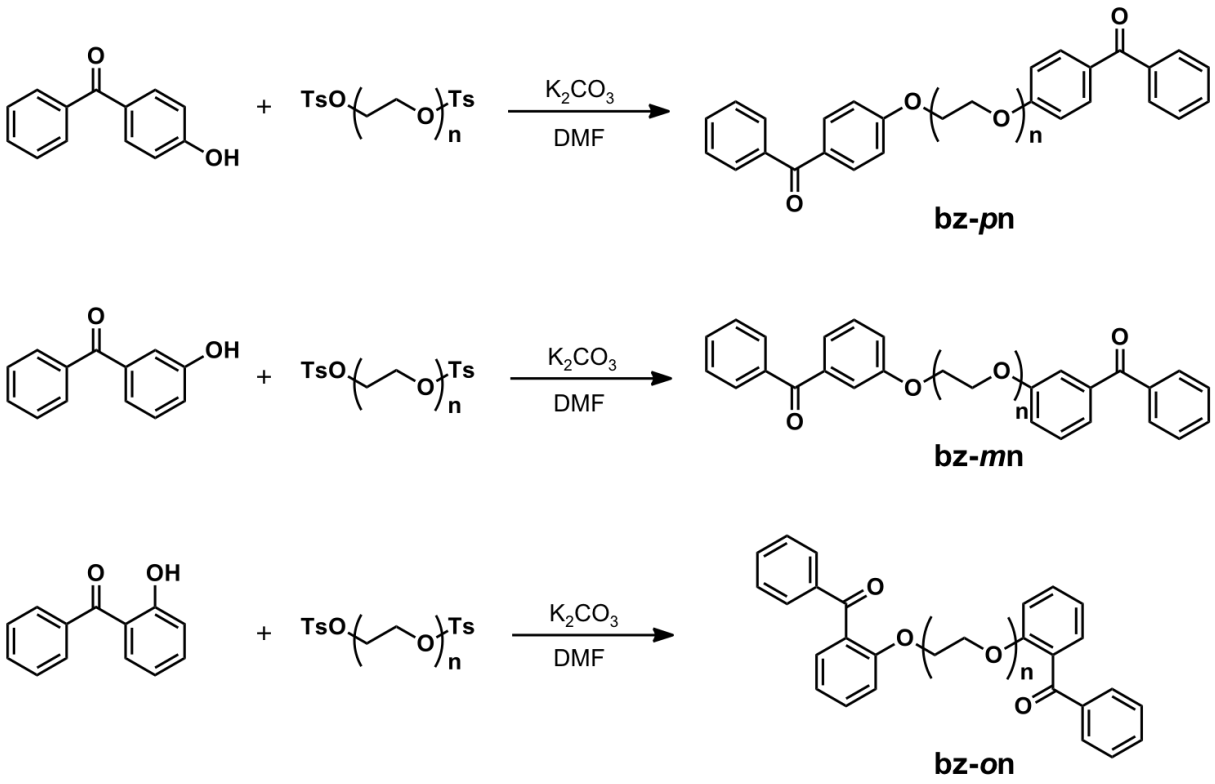

Scheme 1. Synthetic route of **bz-*p*n**, **bz-*m*n**, and **bz-*o*n**.

In a 200 mL two necked flask, A suspension of K_2CO_3 (1.67 g, 12.1 mmol), 4-hydroxybenzophenone (1.24 g, 2.99 mmol) and diethyleneglycol ditosylate (1.24 g, 2.99 mmol) in DMF (40 mL) was stirred at 80°C for 16 h. After filtration and distilling off DMF under reduced pressure, the organic layer was separation and the aqueous layer was extracted with CH_2Cl_2. The organic layer was combined, dried over $MgSO_4$ and the solvent was removed under reduced pressure. After the purification of the crude product by flash chromatography on SiO_2 (*n*-hexane/ethyl acetate), **bz-*p*2** was obtained.

bz-*p*2 (0.551 g, 40%): ^{1}H NMR (500 MHz, $CDCl_3$) δ (ppm) : 3.99 (4H, t, *J* = 4.7 Hz), 4.25 (4H, t, *J* = 4.8 Hz), 6.99 (4H, d, *J* = 8.9 Hz), 7.47 (4H, t, *J* = 7.6 Hz), 7.57 (2H, t, *J* = 7.4 Hz), 7.75 (4H, d, *J* = 6.9 Hz), 7.82 (4H, d, *J* = 8.9 Hz).

bz-*p*3 (1 .27g, 83%): ^{1}H NMR (500 MHz, $CDCl_3$) δ (ppm) 3.78 (4H, s), 3.91 (4H, t, *J* = 4.8 Hz), 4.21 (4H, t, *J* = 4.8 Hz), 6.97 (4H, d, *J* = 8.8 Hz), 7.47 (4H, t, *J* = 7.6 Hz), 7.56 (2H, t, *J* =

7.4 Hz), 7.74 (4H, d, *J* = 7.1 Hz) , 7.81 (4H, d, *J* = 8.8 Hz).

bz-*p*4 (2.20 g, 60%): ^{1}H NMR (500 MHz, $CDCl_3$) δ (ppm) 3.70–3.76 (8H, m), 3.89 (4H, t, *J* = 4.8 Hz), 4.21 (4H, t, *J* = 4.8 Hz), 6.97 (4H, d, *J* = 8.9 Hz), 7.47 (4H, t, *J* = 7.6 Hz), 7.56 (2H, t, *J* = 7.5 Hz), 7.74 (4H, d, *J* = 8.5 Hz) , 7.81 (4H, d, *J* = 8.9 Hz).

bz-*p*5 (0.588 g, 83%): ^{1}H NMR (500 MHz, $CDCl_3$) δ (ppm) 3.67–3.70 (8H, m), 3.73–3.74 (4H, m) , 3.89 (4H, t, *J* = 4.8 Hz), 4.21 (4H, t, *J* = 4.8 Hz), 6.97 (4H, d, *J* = 8.9 Hz), 7.47 (4H, t, *J* = 7.6 Hz), 7.56 (2H, t, *J* = 7.6 Hz), 7.74 (4H, d, *J* = 5.0 Hz) , 7.81 (4H, d, *J* = 8.9 Hz).

bz-*p*6 (1.78 g, 83%): ^{1}H NMR (500 MHz, $CDCl_3$) δ (ppm) 3.65–3.69 (12H, m), 3.73 (4H, t, *J* = 5.1) , 3.89 (4H, t, *J* = 4.8 Hz), 4.21 (4H, t, *J* = 4.8 Hz), 6.97 (4H, d, *J* = 8.9 Hz), 7.47 (4H, t, *J* = 7.6 Hz), 7.56 (2H, t, *J* = 7.4 Hz), 7.74 (4H, d, *J* = 7.0 Hz) , 7.81 (4H, d, *J* = 8.8 Hz).

bz-*m*2 (1.15 g, 82%): ^{1}H NMR (500 MHz, $CDCl_3$) δ (ppm) : 3.96 (4H, t, *J* = 4.7 Hz), 4.21 (4H, t, *J* = 4.7 Hz), 7.14–7.17 (2H, m), 7.34–7.39 (6H, m), 7.48 (4H, t, *J* = 7.7 Hz), 7.59 (2H, t, *J* = 7.4 Hz), 7.79 (4H, d, *J* = 7.8 Hz).

bz-*m*3 (0.679 g, 53%): ^{1}H NMR (500 MHz, $CDCl_3$) δ (ppm) : 3.75 (4H, s), 3.88 (4H, t, *J* = 4.9 Hz), 4.17 (4H, t, *J* = 4.7), 7.13–7.15 (2H, m), 7.33–7.37 (6H, m), 7.46 (4H, t, *J* = 7.9 Hz), 7.57 (2H, t, *J* = 7.5 Hz), 7.78 (4H, d, *J* = 8.5 Hz).

bz-*m*4 (1.29 g, 78%): ^{1}H NMR (500 MHz, $CDCl_3$) δ (ppm) : 3.68–3.74 (8H, m), 3.87 (4H, t, *J* = 4.8 Hz), 4.17 (4H, t, *J* = 4.8), 7.13–7.16 (2H, m), 7.33–7.38 (6H, m), 7.47 (4H, t, *J* = 7.7 Hz), 7.58 (2H, t, *J* = 8.0 Hz), 7.79 (4H, d, *J* = 8.1 Hz).

bz-*m*5 (1.42 g, 83%): ^{1}H NMR (500 MHz, $CDCl_3$) δ (ppm) : 3.66–3.73 (12H, m), 3.86 (4H, t, *J* = 4.7 Hz), 4.17 (4H, t, *J* = 4.7), 7.14–7.16 (2H, m), 7.33–7.38 (6H, m), 7.48 (4H, t, *J* = 7.7 Hz), 7.58 (2H, t, *J* = 7.4 Hz), 7.79 (4H, d, *J* = 8.1 Hz).

bz-*m*6 (1.28 g, 93%): ^{1}H NMR (500 MHz, $CDCl_3$) δ (ppm) : 3.65–3.73 (16H, m), 3.87 (4H, t, *J* = 4.7 Hz), 4.17 (4H, t, *J* = 4.8), 7.15 (2H, d, *J* = 7.7 Hz), 7.35–7.38 (6H, m), 7.48 (4H, t, *J* = 7.6 Hz), 7.59 (2H, t, *J* = 7.4 Hz), 7.80 (4H, d, *J* = 7.3 Hz).

bz-*o*3 (1.09 g, 93%): ^{1}H NMR (500 MHz, $CDCl_3$) δ (ppm) : 3.18 (4H, s), 3.42 (4H, t, *J* = 5.1

Hz), 4.00 (4H, d, *J* = 5.0 Hz), 6.96 (2H, d, *J* = 8.3 Hz), 7.06 (2H, t, *J* = 7.2 Hz), 7.37–7.42 (6H, m), 7.45 (2H, t, *J* = 7.6 Hz), 7.51 (2H, t, *J* = 7.4 Hz), 7.77 (4H, d, *J* = 6.9 Hz).

bz-*o*4 (1.15 g, 71%): ^{1}H NMR (500 MHz, $CDCl_3$) δ (ppm) : 3.32–3.39 (8H, m), 3.47 (4H, t, *J* = 5.0 Hz), 4.03 (4H, t, *J* = 5.0 Hz), 6.97 (2H, d, *J* = 8.4 Hz), 7.06 (2H, t, *J* = 7.5 Hz), 7.39–7.46 (8H, m), 7.53 (2H, t, *J* = 7.4 Hz), 7.77 (4H, t, *J* = 7.3 Hz).

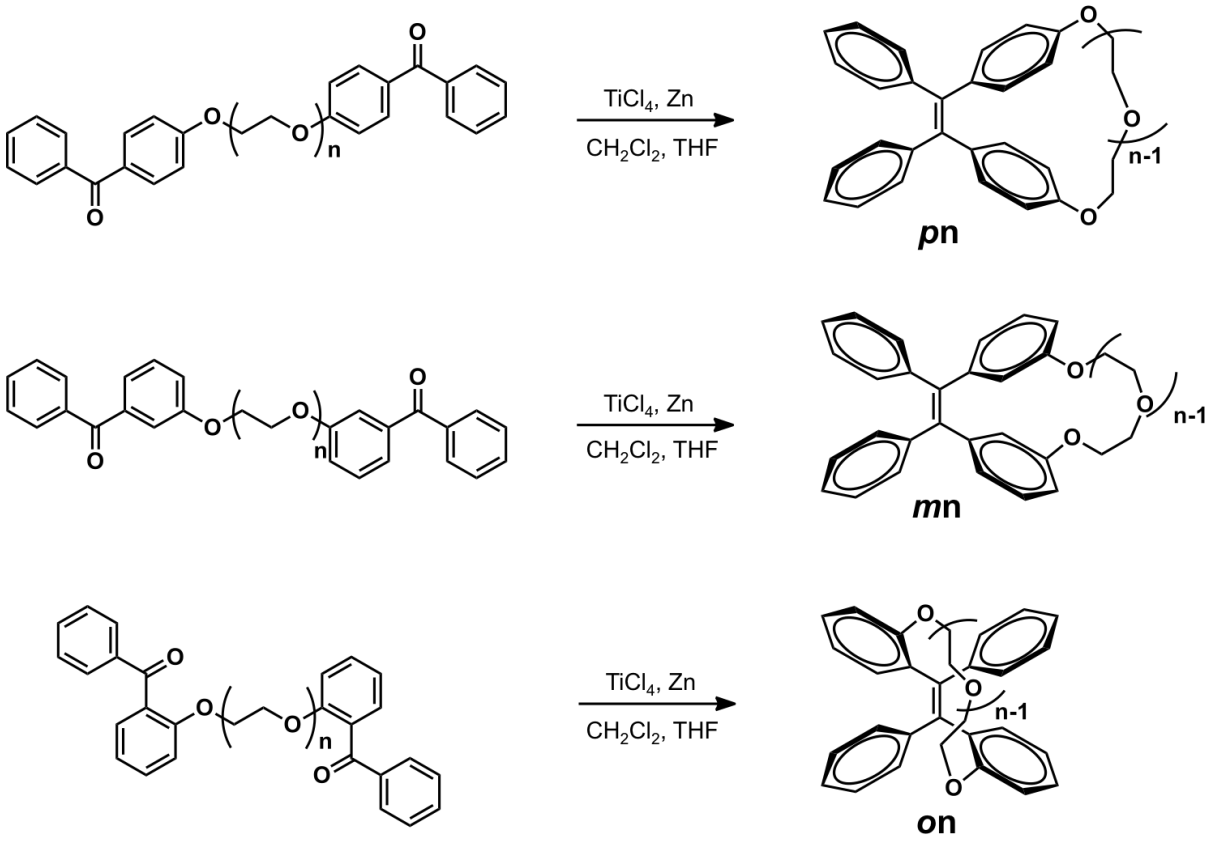

Scheme 2. Synthetic route of ***p*n**, ***m*n**, and ***o*n**.

In a 300 mL three necked flask, zinc powder (3.17 g, 48.5 mmol), THF (58 mL), pyridine 0.5 mL and 1M $TiCl_4/CH_2Cl_2$ solution were added and heated at 80^{o}C. Then **bz-*p*2** (0.500 g, 1.07 mmol) in anhydrous THF (21 mL) was dropped into this slurry over for 6 h and the resulting mixture was stirred at 80^{o}C for 16 h. After cooling to room temperature, the mixture was hydrolyzed by addition of aqueous K_2CO_3 solution (18 mL, 10 %) and distilled water (18 mL). After filtration and distilling off THF, the organic layer was separation and the aqueous layer

was extracted with CH_2Cl_2. The organic layer was combined, dried over $MgSO_4$ and the solvent was removed under reduced pressure. After the purification of the crude product by flash chromatography on SiO_2 (*n*-hexane/ethyl acetate), ***p*2** was obtained.

***p*2** (0.206 g, 44%): ^{1}H NMR (500 MHz, $CDCl_3$) δ (ppm) : 3.61 (4H, t, *J* = 4.4 Hz), 4.25 (4H, t, *J* = 4.5 Hz), 6.63 (4H, d, *J* = 8.7 Hz), 6.74 (4H, d, *J* = 8.6 Hz), 7.14–7.18 (6H, m), 7.21–7.23 (4H, m). ^{13}C NMR (126 MHz, $CDCl_3$) δ (ppm): 68.77, 71.85, 115.76, 126.72, 127.80, 130.86, 132.18, 138.12, 141.35, 142.10, 157.36. HRMS(ESI) Calcd. for $C_{30}H_{26}O_3$ $[M+Na]^+$: *m*/*z* 457.1780, Found: *m*/*z* 457.1768.

***p*3** (0.12 g, 11%): ^{1}H NMR (500 MHz, $CDCl_3$) δ (ppm) 3.65 (4H, s), 3.72 (4H, t, *J* = 4.6 Hz), 4.24 (4H, t, *J* = 4.5 Hz), 6.70 (4H, t, *J* = 8.8 Hz), 6.85 (4H, d, *J* = 8.8 Hz), 7.09~7.12 (10H, m). ^{13}C NMR (126 MHz, $CDCl_3$) δ (ppm): 68.46, 70.50, 71.47, 115.05, 126.43, 127.65, 131.25, 132.36, 137.34, 140.62, 142.94, 157.14. HRMS(ESI) Calcd. for $C_{32}H_{30}O_4$ $[M+Na]^+$: *m*/*z* 501.2042, Found: *m*/*z* 501.2028.

***p*4** (0.0140 g, 4%): ^{1}H NMR (500 MHz, $CDCl_3$) δ (ppm) 3.61–3.65 (8H, m), 3.77 (4H, t, *J* = 4.6 Hz), 4.16 (4H, t, *J* = 4.6 Hz), 6.67 (4H, t, *J* = 8.8 Hz), 6.88 (4H, d, *J* = 8.8 Hz), 7.05–7.12 (10H, m). ^{13}C NMR (126 MHz, $CDCl_3$) δ (ppm): 67.92, 69.66, 70.64, 71.20, 114.38, 126.33, 127.61, 131.31, 132.46, 137.05, 140.25, 143.45, 157.06. HRMS(ESI) Calcd. for $C_{34}H_{34}O_5$ $[M+Na]^+$: *m*/*z* 545.2304, Found: *m*/*z* 545.2286.

***p*5** (0.0895 g, 16%): ^{1}H NMR (500 MHz, $CDCl_3$) δ (ppm) 3.67–3.68 (12H, m), 3.79 (4H, t, *J* = 4.6 Hz), 4.10 (4H, t, *J* = 4.6), 6.66 (4H, d, *J* = 8.7 HZ), 6.89 (4H, d, *J* = 8.7 Hz), 7.03–7.05 (4H, m), 7.08–7.10 (6H, m). ^{13}C NMR (126 MHz, $CDCl_3$) δ (ppm): 67.63, 69.47, 70.47, 70.65, 71.05, 113.99, 126.27, 127.58, 131.35, 132.48, 136.86, 140.07, 143.68, 157.06. HRMS(ESI) Calcd. for $C_{36}H_{38}O_6$ $[M+Na]^+$: *m*/*z* 589.2566, Found: *m*/*z* 589.2556.

***p*6** (0.341 g, 35%): ^{1}H NMR (500 MHz, $CDCl_3$) δ (ppm) 3.67–3.71 (16H, m), 3.82 (4H, t, *J* = 4.7 Hz), 4.08 (4H, t, *J* = 4.7 Hz), 6.67 (4H, d, *J* = 8.8 HZ), 6.91 (4H, d, *J* = 8.8 Hz), 7.01–7.03 (4H, m), 7.07–7.09 (6H, m). ^{13}C NMR (126 MHz, $CDCl_3$) δ (ppm): 67.31, 69.65, 70.63, 70.68, 70.84, 70.98, 113.80, 126.20, 127.55, 131.38, 132.45, 136.65, 139.85, 143.94, 157.12. HRMS(ESI) Calcd. for $C_{38}H_{42}O_7$ $[M+Na]^+$: *m*/*z* 633.2829, Found: *m*/*z* 633.2810.

***m*2** (0.177 g, 38%): ^{1}H NMR (500 MHz, $CDCl_3$) δ (ppm) : 3.61 (4H, t, *J* = 4.6 Hz), 4.16 (4H, t, *J* = 4.6 Hz), 6.60 (2H, d, *J* = 7.6 Hz), 6.67 (2H, d, *J* = 8.2 Hz), 6.88 (2H, t, *J* = 2.0 Hz), 7.01 (2H, t, *J* = 16 Hz), 7.09–7.13 (10H, m). ^{13}C NMR (126 MHz, $CDCl_3$) δ (ppm): 68.89, 71.43, 116.16, 119.16, 123.89, 126.53, 127.68, 128.67, 131.01, 141.10, 142.63, 144.94, 158.76. HRMS(ESI) Calcd. for $C_{30}H_{26}O_3$ $[M+Na]^+$: *m*/*z* 457.1780, Found: *m*/*z* 457.1769.

***m*3** (0.0470 g, 10%): ^{1}H NMR (500 MHz, $CDCl_3$) δ (ppm) : 3.65–3.68 (8H, m), 3.94 (4H, t, *J* = 4.8 Hz), 6.60 (2H, d, *J* = 7.6 Hz), 6.71–6.72 (4H, m), 7.03–7.06 (6H, m), 7.09–7.10 (6H, m). ^{13}C NMR (126 MHz, $CDCl_3$) δ (ppm): 67.68, 69.41, 71.04, 114.11, 118.10, 123.83, 126.51, 127.65, 128.78, 131.18, 141.00, 143.03, 145.14, 158.06. HRMS(ESI) Calcd. for $C_{32}H_{30}O_4$ $[M+Na]^+$: *m*/*z* 501.2042, Found: *m*/*z* 501.2031.

***m*4** (0.238 g, 43%): ^{1}H NMR (500 MHz, $CDCl_3$) δ (ppm) : 3.67–3.68 (8H, m), 3.71 (4H, t, *J* = 4.7 Hz), 3.86 (4H, t, *J* = 4.7 Hz), 6.60 (2H, d, *J* = 7.7 Hz), 6.67–6.71 (4H, m), 7.02–7.10 (12H, m). ^{13}C NMR (126 MHz, $CDCl_3$) δ (ppm): 67.68, 69.27, 70.56, 70.95, 114.02, 117.12, 123.77, 126.49, 127.64, 128.82, 131.22, 140.99, 143.15, 145.13, 158.17. HRMS(ESI) Calcd. for $C_{34}H_{34}O_5$ $[M+Na]^+$: *m*/*z* 545.2304, Found: *m*/*z* 545.2288.

***m*5** (0.201 g, 33%): ^{1}H NMR (500 MHz, $CDCl_3$) δ (ppm) : 3.64–3.72 (16H, m), 3.84 (4H, t, *J* = 4.8 Hz), 6.61 (4H, d, *J* = 7.9 Hz), 6.69 (2H, d, *J* = 8.1 Hz), 7.02–7.10 (12H, m). ^{13}C NMR (126 MHz, $CDCl_3$) δ (ppm): 67.43, 69.40, 70.70, 70.72, 70.81, 114.02, 116.87, 123.90, 126.47, 127.63, 128.78, 131.24, 140.94, 143.25, 145.08, 158.11. HRMS(ESI) Calcd. for $C_{36}H_{38}O_6$ $[M+Na]^+$: *m*/*z* 589.2566, Found: *m*/*z* 589.2550.

***m*6** (0.134 g, 21%): ^{1}H NMR (500 MHz, $CDCl_3$) δ (ppm) : 3.61–3.69 (22H, m), 3.85 (4H, t, *J* = 4.8 Hz), 6.60–6.34 (4H, m), 6.69 (2H, d, *J* = 8.2 Hz), 7.01–7.11 (12H, m). ^{13}C NMR (126 MHz, $CDCl_3$) δ (ppm): 67.43, 69.43, 70.76, 70.81, 70.85, 113.97, 117.16, 123.93, 126.47, 127.62, 128.78, 131.24, 140.90, 143.28, 145.03, 158.07. HRMS(ESI) Calcd. for $C_{38}H_{42}O_7$ $[M+Na]^+$: *m*/*z* 633.2829, Found: *m*/*z* 633.2818.

***o*3** (0.0755 g, 16%): ^{1}H NMR (500 MHz, $CDCl_3$) δ (ppm) : 3.57 (2H, t, *J* = 8.8 Hz), 3.76–3.81 (8H, m), 3.92 (2H, t, *J* = 8.3 Hz), 6.70 (2H, d, *J* = 8.2 Hz), 6.74 (2H, t, *J* = 7.4 Hz), 6.97–7.12 (14H, m). ^{13}C NMR (126 MHz, $CDCl_3$) δ (ppm): 67.94, 70.21, 70.97, 111.17, 120.10, 125.83,

126.92, 128.00, 129.58, 132.03, 132.56, 138.93, 143.12, 157.27. HRMS(ESI) Calcd. for $C_{32}H_{30}O_4$ $[M+Na]^+$: *m*/*z* 501.2042, Found: *m*/*z* 501.2027.

o*4** (0.0866 g, 16%): *cis*-o*4** (0.0770 g, 14%) was obtained by silica gel column chromatography due to difference in retention time. In this system, *cis*-*o*4 was eluted first and *cis*-*trans* mixture (*cis*-*o*4 0.0175 g, 3% *trans*-*o*4 0.0096, 2%) later eluted. *cis*-*o*4: ^{1}H NMR (500 MHz, $CDCl_3$) δ (ppm) : 3.29–3.33 (2H, m), 3.55–3.58 (2H, m), 3.66–3.77 (12H, m), 6.65–6.70 (4H, m), 6.98 (1H, d, *J* = 1.7 Hz), 7.00 (1H, d, *J* = 1.7 Hz), 7.03–7.08 (12H, m). ^{13}C NMR (126 MHz, $CDCl_3$) δ (ppm): 68.58, 69.13, 70.54, 70.72, 112.45, 119.78, 125.82, 127.28, 127.97, 130.74, 132.61, 132.95, 137.84, 143.61, 156.53. HRMS(ESI) Calcd. for $C_{34}H_{34}O_5$ $[M+Na]^+$: *m*/*z* 545.2304, Found: *m*/*z* 545.2287.

References

[1] J. Mei, N. L. C. Leung, R. T. K. Kwok, J. W. Y. Lam, B. Z. Tang, *Chem. Rev.*, **2015**, *115,* 11718–11940.

[2] X. Zhang, X. Zhang, L. Tao, Z. Chi, J. Xu, Y. Wei, *J. Mater. Chem. B*, **2014**, *2*, 4398–4414.

[3] A. Qin, J. W. Y. Lam, B. Z. Tang, *Prog. Polym. Sci.*, **2012**, *37*. 182–209.

[4] Y. Hong, J. W. Y. Lam, B. Z. Tang, *Chem. Soc. Rev.*, **2011**, *40*, 5361–5388.

[5] Y. Hong, J. W. Y. Lam, B. Z. Tang, *Chem. Commun.*, **2009**, 4332–4353.

[6] Z. Zhao, C. Y. K. Chan, S. Chen, C. Deng, J. W. Y. Lam, C. K. W. Jim, Y. Hong, P. Lu, Z. Chang, X. Chen, P. Lu, H. S. Kwok, H. Qiu, B. Z. Tang, *J. Mater. Chem.*, **2012**, *22*, 4527–4534.

[7] W. Qin, J. W. Y. Lam, Z. Yang, S. Chen, G. Liang, W. Zhao, H. S. Kwok, B. Z. Tang, *Chem. Commun.*, **2015**, *51*, 7321–7324.

[8] Z. Ning, Z. Chen, Q. Zhang, Y. Yan, S. Qian, Y. Cao, H. Tian, *Adv. Funct. Mater.*, **2007**, *17*, 3799–3807.

[9] T. Noguchi, B. Roy, D. Yoshihara, Y. Tsuchiya, T. Yamamoto, S. Shinkai, *Chem. Eur. J.* **2014**, *20*, 381−384.

[10] J. Zhao, D. Yang, Y. Zhao, X.-J. Yang, Y.-Y. Wang, B. Wu, *Angew. Chem. Int. Ed.* **2014**, *53*, 6632–6636.

[11] N. Sinha, L. Stegemann, T. T. Y. Tan, N. L. Doltsinis, C. A. Strassert, F. E. Hahn, *Angew. Chem. Int. Ed.* **2017**, *56*, 2785–2789.

[12] J.-B. Xiong, Y.-X. Yuan, L. Wang, J.-P. Sun, W.-G. Qiao, H.-C. Zhang, M. Duan, H. Han, S. Zhang, Y.-S. Zheng, *Org. Lett.* **2018**, *20*, 373−376.

[13] H.-T. Feng, Y.-X. Yuan, J.-B. Xiong, Y.-S. Zheng, B. Z. Tang, Chem. Soc. Rev. 2018, 47, 7452-7476.

[14] K. A.Muszkat, E. Fischer, *J. Chem. Soc. B,* **1967**, 662–678.

[15] Y. Cai, L. Du, K. Samedov, X. Gu, F. Qi, H. H. Y. Sung, B. O. Patrick, Z. Yan, X. Jiang, H. Zhang, J. W. Y. Lam, I. D. Williams, D. L. Phillips, A. Qin, B. Z. Tang, *Chem. Sci.* **2018**, *9*, 4662–4670.

[16] C. Lee, W. Yang, R. G. Parr, *Phys*. *Rev*. *B: Condens*. *Matter Mater*. *Phys*. **1988**, *37*, 785−789.

[17] A. D. Becke, *J. Chem*. *Phys*. **1993**, *98*, 5648−5652.

[18] Gaussian 16, Revision A.03, M. J. Frisch, G. W. Trucks, H. B. Schlegel, G. E. Scuseria, M. A. Robb, J. R. Cheeseman, G. Scalmani, V. Barone, G. A. Petersson, H. Nakatsuji, X.

Li, M. Caricato, A. V. Marenich, J. Bloino, B. G. Janesko, R. Gomperts, B. Mennucci, H. P. Hratchian, J. V. Ortiz, A. F. Izmaylov, J. L. Sonnenberg, D. Williams-Young, F. Ding, F. Lipparini, F. Egidi, J. Goings, B. Peng, A. Petrone, T. Henderson, D. Ranasinghe, V. G. Zakrzewski, J. Gao, N. Rega, G. Zheng, W. Liang, M. Hada, M. Ehara, K. Toyota, R. Fukuda, J. Hasegawa, M. Ishida, T. Nakajima, Y. Honda, O. Kitao, H. Nakai, T. Vreven, K. Throssell, J. A. Montgomery, Jr., J. E. Peralta, F. Ogliaro, M. J. Bearpark, J. J. Heyd, E. N. Brothers, K. N. Kudin, V. N. Staroverov, T. A. Keith, R. Kobayashi, J. Normand, K. Raghavachari, A. P. Rendell, J. C. Burant, S. S. Iyengar, J. Tomasi, M. Cossi, J. M. Millam, M. Klene, C. Adamo, R. Cammi, J. W. Ochterski, R. L. Martin, K. Morokuma, O. Farkas, J. B. Foresman, D. J. Fox, Gaussian, Inc., Wallingford CT, **2016**.

[19] *SHELXS-2013 and SHELXL-2013*: G. M. Sheldrick, Short History of SHELX. *Acta Crystallogr., Sect. A: Found. Crystallogr.* **2008**, *64*, 112–122.

[20] *Olex2*: O. V. Dolomanov, L. J. Bourhis, R. J. Gildea, J. A. K. Howard, H. Pushmann, *J. Appl. Crystallogr.* **2009**, *42*, 339–341.

[21] S. Hamai, F. Hirayama, *J. Phys. Chem.* **1983**, *87*. 83–89.

[22] A. Fürstner, G. Seidel, C. Kopiske, C. Krüger, R. Mynott, *Liebigs Ann.* **1996**, 655–662.

Chapter V

Photo-induced pyramidal inversion of phosphines involved in the AIE behavior

Chapter V

Photo-induced pyramidal inversion of phosphines involved in the AIE behavior

Abstract: In this chapter, the author investigated the large structural change in the excited state of phosphines that was involved with the AIE behavior. The phosphines having three different polycyclic aromatic hydrocarbons (PAH) were synthesized by stepwise Grignard reactions. In the diluted solution, the fluorescence intensity of the PAH-containing phosphines definitely decreased compared to the correspond PAHs, like typical AIE behavior, moreover, the phosphines exhibited racemization by photoexcitation. According to the theoretical calculations, the photoplanarization of phosphines promotes nonradiative decay from the excited state, resulted in photoracemization in the diluted solution. This photoplanarization was not specific to PAH-containing phosphines, but was also observed in common phosphines such as PH_3, PMe_3, and PPh_3.

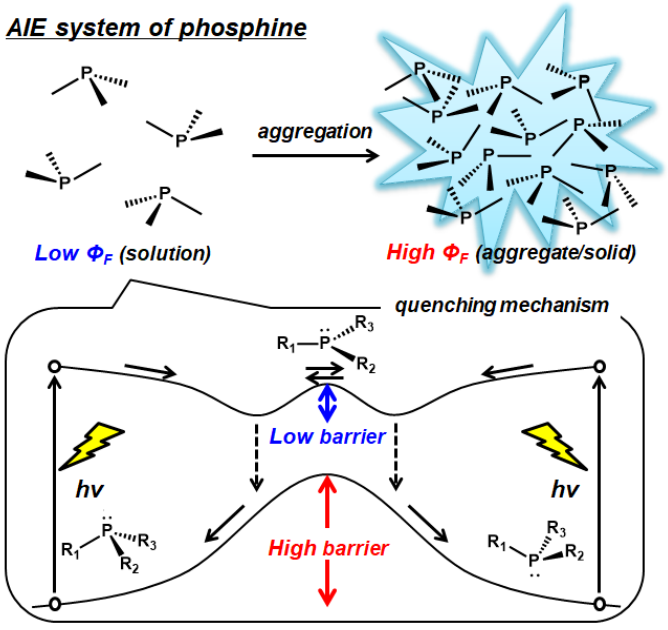

Introduction

The luminogens showing aggregation induced-emission behavior (AIEgens) have been vigorously studied for applications in organic light emitting diode (OLED) and luminescent sensors. On another front, in recent years, not only such applications but also the quenching mechanism of AIEgens in the diluted solution has also attracted attention, because the quenching is often involved in the large molecular motions in the excited state which lead to interesting photo-induced phenomena such as photochemical reactions, photoisomerizations, twisted intramolecular charge-transfer (TICT), and so on.

In Chapter IV, I studied AIE behavior of tetraphenylthene (TPE) derivatives, and revealed that the twisting of central C=C bond (π-twist) in the excited state played a crucial role for the quenching. Then, in other AIE molecules not having C=C bond, what kind of large molecular motions promote quenching from the excited state in the diluted solution? For example, phenylsilole is known to be AIE-active molecule,[1] but don't have twistable C=C bond. To elucidate the AIE mechanism of phenylsilole derivatives, Blancafort *et al.* calculated descent pathway of dimethyl tetraphenylsilole (DMTPS) from the excited state, and explained that silole ring puckering accelerated non-radiative decay process.[2] The ring puckering in the excited state was observed in other molecules.[3-8] In case of *o*-carborane derivatives that are known as typical AIEgens,[9] it was reported that elongation of C-C bond on the *o*-position played important role for the quenching in the diluted solution.[10] Excited state intramolecular proton transfer (ESIPT) is also known as a kind of photophenomenon related to the AIE effect.[11] Thus, large molecular motions associated with the quenching of AIEgens have been elucidated.[12,13]

Phosphines with the chemical formula PR_3 have been extensively studied in organic chemistry as ligands, catalysts, surfactants, semiconductors, energy transporters, and so on.[14-17] Although the excited state dynamics study of phosphines was rarely reported, Natarajan and Xue *et al.* recently reported that triphenylphosphine derivatives showed typical AIE behavior.[18,19] They did not experimentally demonstrate the AIE mechanism of phosphines, but this result implied that phosphines undergo a potentially large structural change in the excited state. Therefore, I wonder what structural change phosphines takes place in the excited state.

From the knowledge of structural chemistry, phosphines have pyramidal structure, and Mislow et al. have systematically studied the thermal pyramidal inversion behavior since 1970's.[20-30] According to those reports, phosphines have high inversion barrier except for a few cases,[23-27,29,30] thus it is believed that a high temperature is required to induce the pyramidal inversion of phosphines. On another front, it is known that sulfoxides with pyramidal structure similar to the phosphines have also high inversion barrier in the ground state, but the inversion barrier is decreased by photoexcitation.[31-33] Moreover, Finney et al. reported that pyrenyl-sulfoxides was non-emissive in the diluted solution, but they became emissive when the pyramidal inversion was inhibited by coordination of metal ion.[34] Based on the above findings, I anticipated that pyramidal inversion behavior of phosphines in the excited state was closely related to the AIE behavior.

Herein, in order to visualize the pyramidal inversion behavior of phosphines in the excited state, I synthesized *P*-stereogenic phosphines and revealed the photophysical properties including AIE behavior and photoracemization behavior by a variety of spectroscopies. Furthermore, I studied the molecular dynamics and the inversion barrier in the excited state by quantum chemical computations. This is first research about photo-induced pyramidal inversion of phosphines.

Results and Discussion

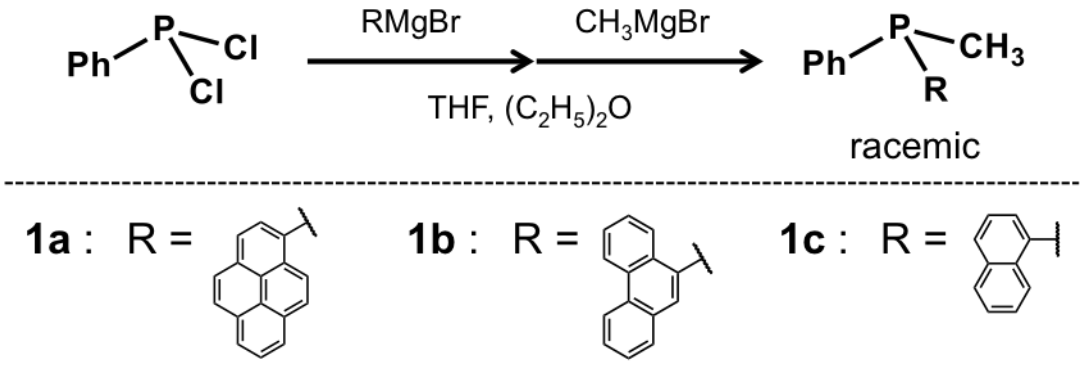

Figure 1. Synthetic route for racemic phosphines **1a-c**.

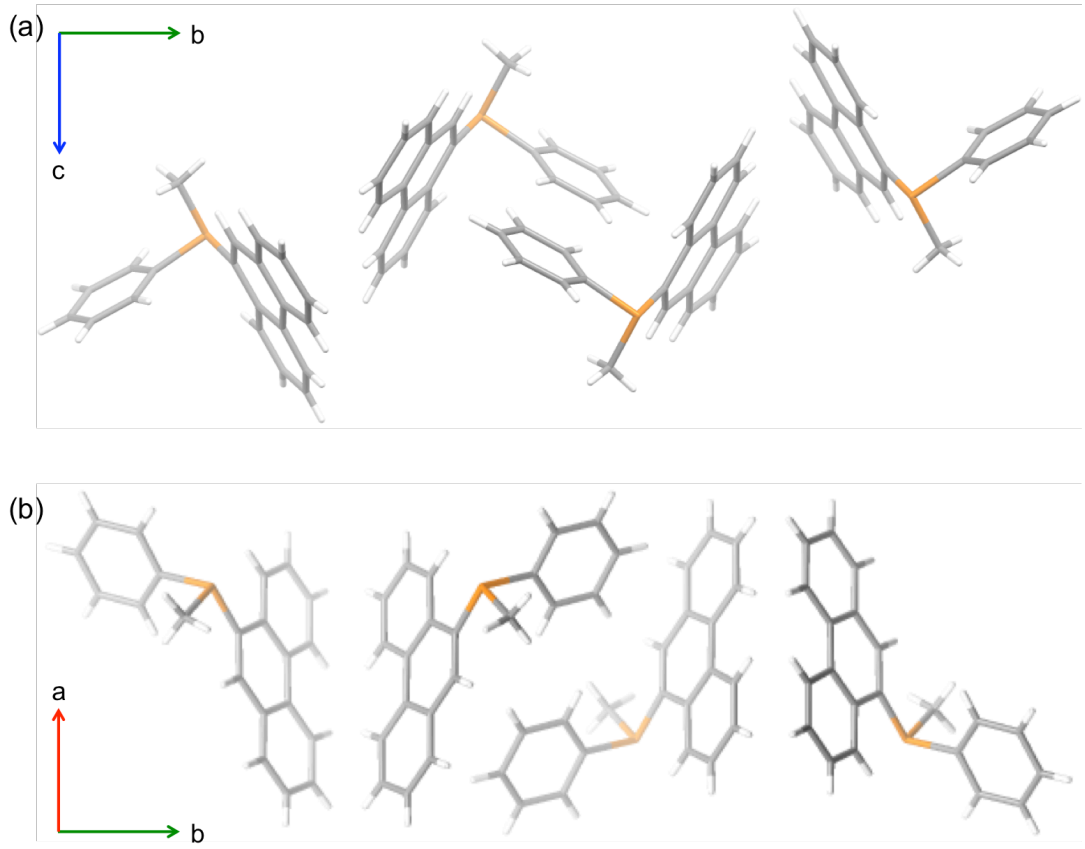

Figure 2. Crystal packing of racemic mixture of **1b** viewed from (a) a axis and (b) c axis.

Table 1. Summary of crystallographic data of racemic mixture of **1b**.

Identification code	**1b (racemic)**
Empirical formula	$C_{21}H_{17}P$
Formula weight	300.33
Temperature	193(2) K
Crystal system, space group	monoclinic, $P2_1/c$
Unit cell dimensions	a = 9.29910(10) Å α = 90 °
	b = 24.6719(2) Å β = 95.6580(10) °
	c = 6.86270(10) Å γ = 90 °
Volume	1563.87(3) $Å^3$
Z, Calculated density	4, 1.276 g/cm^3
Absorption coefficient	1.478 mm^{-1}
F(000)	632
Crystal size	0.80 × 0.60 × 0.20 mm
Theta range for data collection	3.58 to 77.05 °
Limiting indices	-11<=*h*<=11, -31<=*k*<=30, -8<=*l*<=8
Reflections collected / unique	20264 / 3248 [R_{int} = 0.0476]
Completeness to theta = 27.46	98.1%
Refinement method	Full-matrix least-squares on F^2
Data / restraints / parameters	3248 / 0 / 200
Goodness-of-fit on F^2	1.057
Final *R* indices [I>2sigma(I)]	R_1 = 0.0389, wR_2 = 0.1113
R indices (all data)	R_1 = 0.0399, wR_2 = 0.1122
Largest diff. peak and hole	0.276 and -0.345 e. $Å^{-3}$

Racemic tertiary phosphines of the type $PRPhCH_3$ were synthesized by two-step Grignard reactions from dichlorophenylphosphine (Figure 1). They were characterized by ^1H NMR, ^{13}C NMR, ^{31}P NMR spectroscopy, and electrospray ionization mass spectrometry (ESI-MS). Although **1a** and **1c** were not crystalized because they were liquid or sticky solid around room temperature, a single crystal of **1b** was obtained by recrystallization. According to the single crystal X-ray diffraction study of racemic **1b**, (*R*)- and (*S*)- isomers were arranged alternately in the crystal (Figure 2, Table 1). Pure isomer could be not separated by recrystallization or normal silica gel column chromatography.

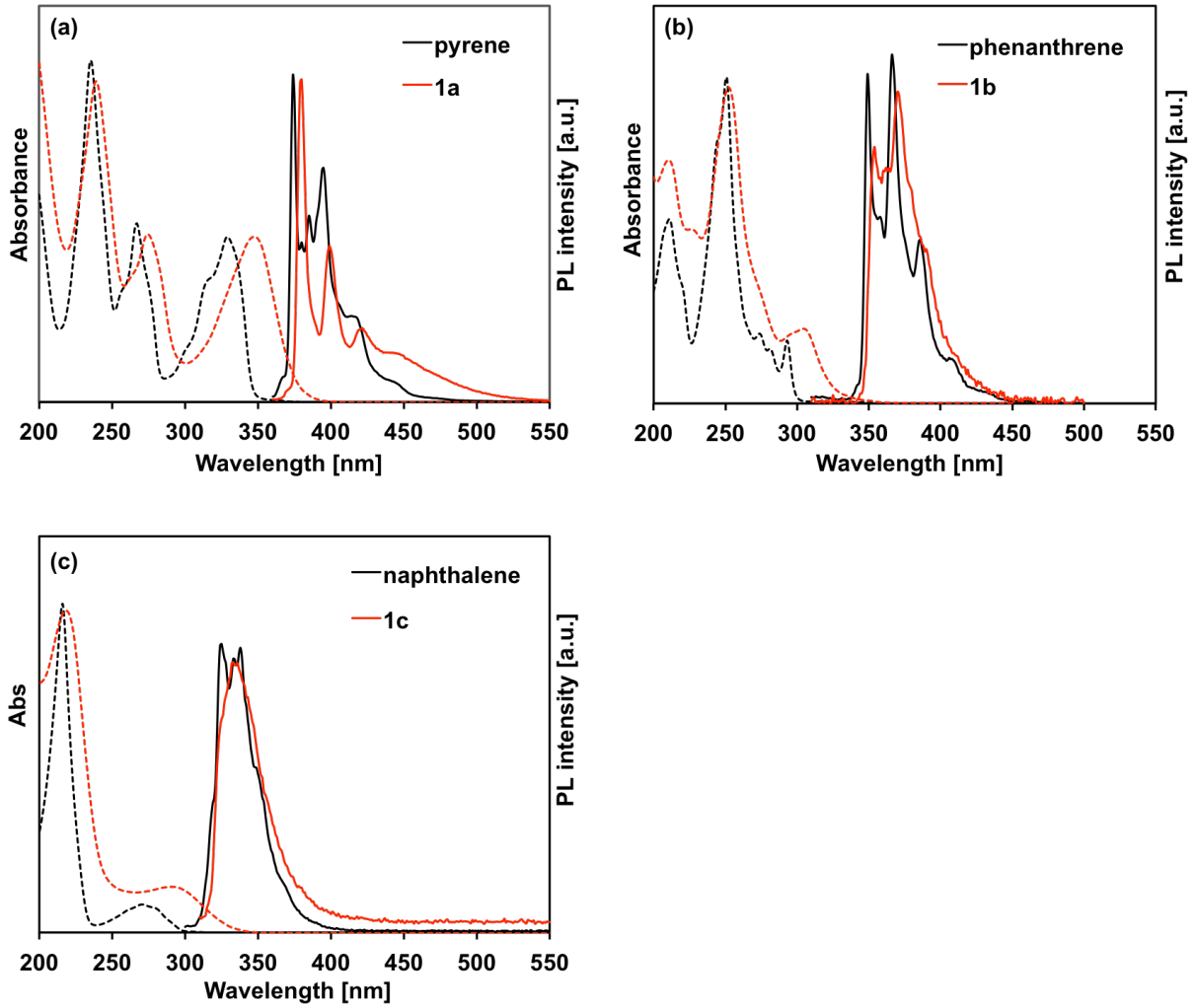

Figure 3. UV-vis absorption (dashed lines) and photoluminescence (PL) (solid lines) spectra of (a) pyrene and **1a**, (b) phenanthrene and **1b**, and naphthalene and **1c**.

Table 2. Photophysical properties of PAHs and **1a-c**.

Compound	Φ_f [a]	τ [ns]	k_r [10^6 s^{-1}]	k_{nr} [10^6 s^{-1}]
pyrene	0.34	16.8	20	39
1a	0.22	14.8	15	53
phenanthrene	0.10	12.6	79	7.1
1b	0.03	13.6	22	71
naphthalene	0.23	14.3	16	54
1c	0.12	6.9	13	98

[a] Φ_f of **1a-c** were measured with the corresponding PAHs as the standards

The photophysical properties of **1a-c** were measured in the diluted CH_3CN solutions to compare with the unsubstituted polycyclic aromatic hydrocarbons (PAHs), pyrene, phenanthrene, and naphthalene. The UV spectra of **1a-c** were similar to the corresponding PAHs, but the longer-wavelength absorption maxima were slightly red-shifted (Figure 2a-c), The red-shift was ascribed to partial contribution of the n-π* transition from the P atom to the PAHs moieties with the main π-π* transition of the PAHs, which was revealed by the calculations of molecular orbitals (*vide infra*).

Photoluminescence (PL) from **1a-c** were identified from the local excited state of the PAHs moieties (LE emission) because the PL spectra of **1a-c** were very similar to those of the corresponding PAHs (Figure 3a-c). Unlike typical AIEgens, **1a-c** were emissive in the diluted solution. However, the relative fluorescence quantum yield (Φ_f) were lower than those of the PAHs (Table 2). The fluorescence lifetime of 1a-c showed first-order decay. Radiative and non-radiative rate constants (k_r, k_{nr}) of **1a-c** were calculated from the Φ_f and τ. k_r of **1a-c** were lower than those of the corresponding PAHs, and k_{nr} of **1a-c** were higher. These results indicated that some nonradiative processes dissipated the excited energies of **1a-c**.

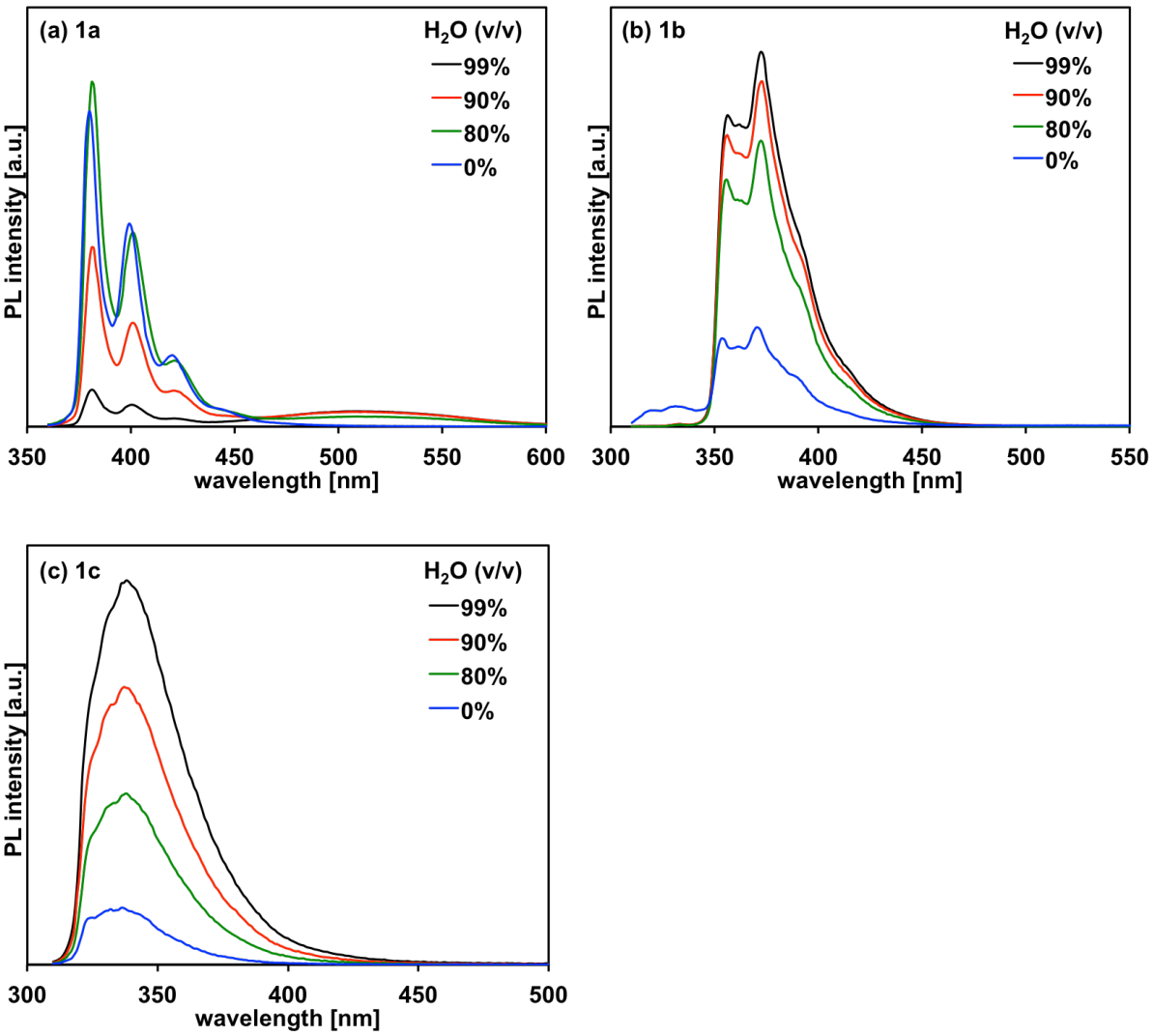

Figure 4. Photoluminescence (PL) spectra of (a) **1a**, (b) **1b**, and (c) **1c** in the aggregated state in the mixture of THF and H_2O (10 μM). Water volume fractions of the mixture (v/v) was varied in the range of 0-99 %.

AIE behavior of **1a-c** was monitored by the emission spectroscopy when the aggregates were formed in the mixtures of CH_3CN and water (Figure 4). The photoluminescence (PL) intensities and the Φ_f increased by the addition of water (**1b**: 0.03→0.11, **1c**: 0.12→1.00, upon the solvent change (CH_3CN → CH_3CN/water =1/99 (*v*/*v*)). On the other hand, **1a** did not show AIE behavior because it strongly reflected the pyrenyl characteristic; the excimer emission on the longer wavelength appeared simultaneously with disappearance of the monomer emission by aggregation (Φ_f: 0.22→0.07).

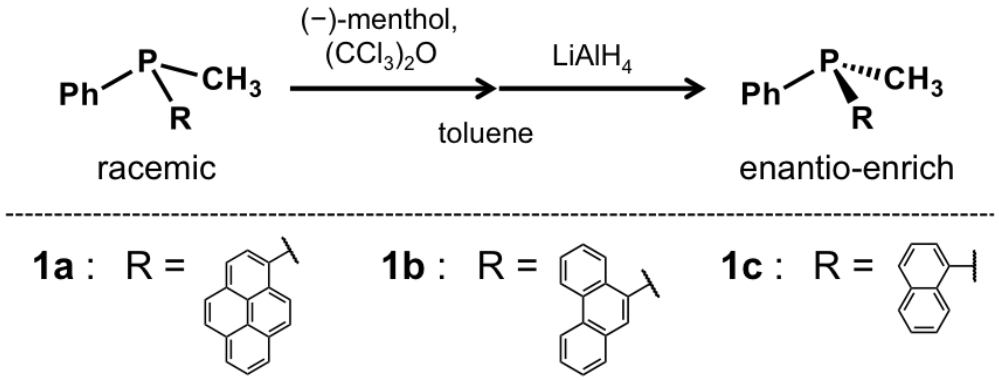

Figure 5. Synthetic route for enantio-enriched phosphines **1a-c**.

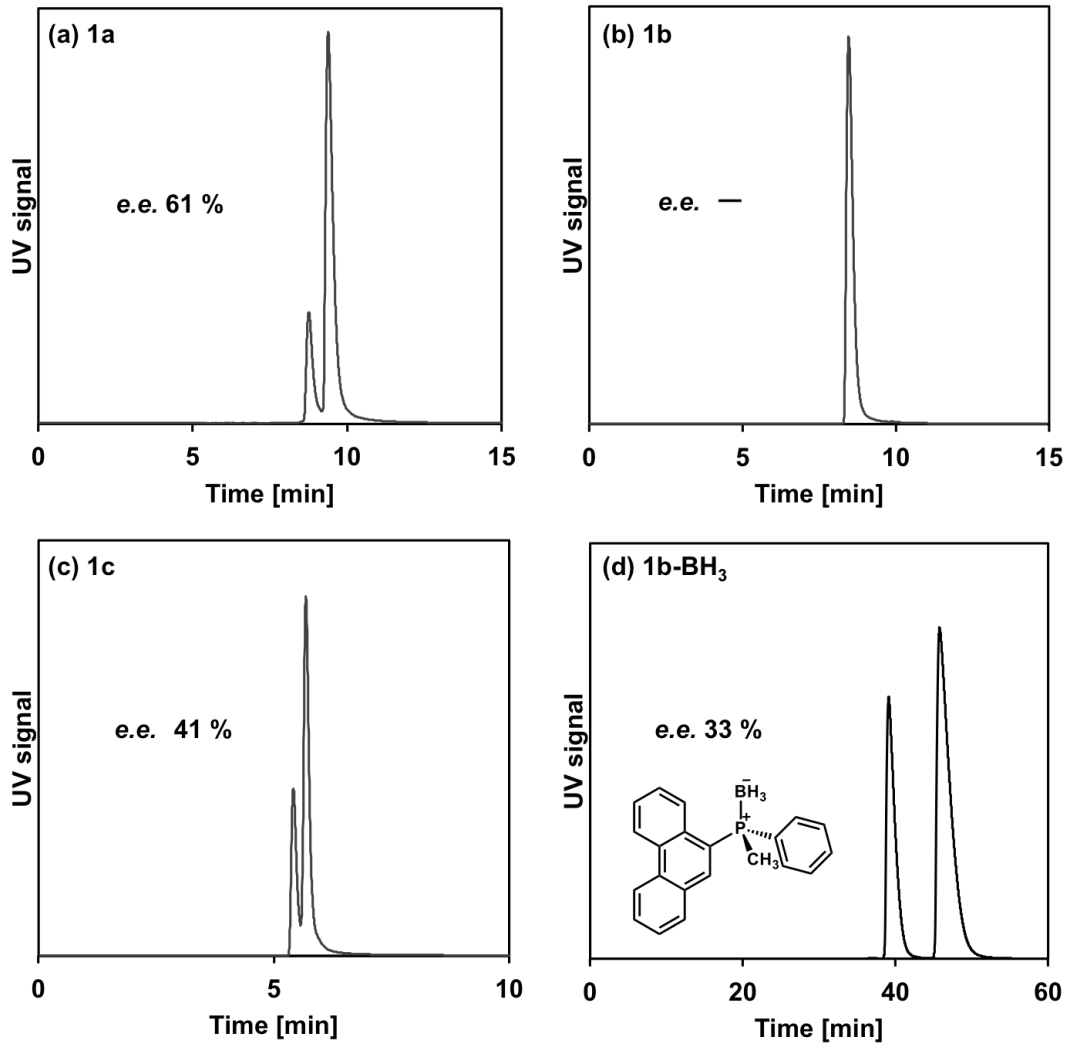

Figure 6. Chiral column chromatograms of enantio enriched (a) **1a**, (b) **1b**, (c) **1c**, and (d) **1b-BH3**. All samples were diluted in hexane/chloroform = 9/1 mixtures (1mg / 1mL).

To investigate pyramidal inversion behavior of phosphines, enantio-enriched **1a-c** were synthesized by asymmetric Appel reaction with (−)-menthol as the asymmetric source (Figure 5).[35-37] Their chiralities were confirmed by circular dichroism (CD) spectroscopy and chiral column. They all showed the signals in CD spectra, indicating that they had chirality. In addition, two separated peaks were observed in chiral HPLC column chromatograph of **1a** and **1c**. Although **1b** showed single peak in the chiral column chromatograph, boronated **1b** (**1b-BH_3**) showed two separated peaks, which also supported they were chiral molecules. In addition, the enantio-enrichment (*e.e.*) could be calculated from integrations of the chiral column chromatograph. Their *e.e* were not so high (**1a**: 61 %, **1b-BH_3**: 33 %, and **1c**: 41 %) but they were not so important to investigate photo-induced pyramidal inversion behavior, therefore enantio-enriched **1a-c** obtained here were used in the following experiments.

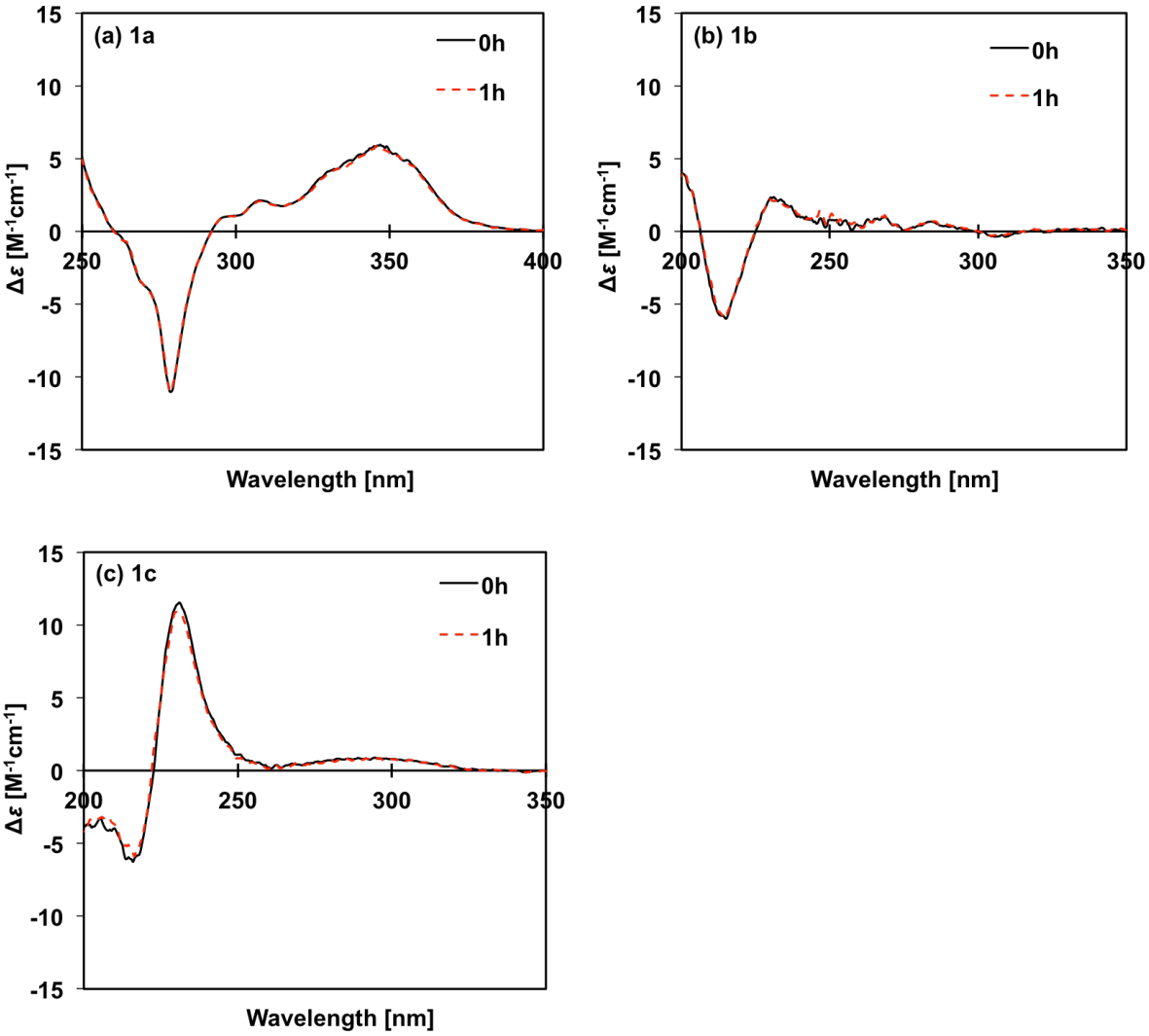

Figure 7. CD spectra of enantio enriched (a) **1a**, (b) **1b** and (c) **1c**. The samples were kept in dark condition for 1 hour at 70 °C in CH_3CN (50 μM).

Under dark conditions, the CD intensity remained unchanged for one hour at 70° solution, indicating that **1a-c** had high inversion barrier in the ground state (Figure 7).

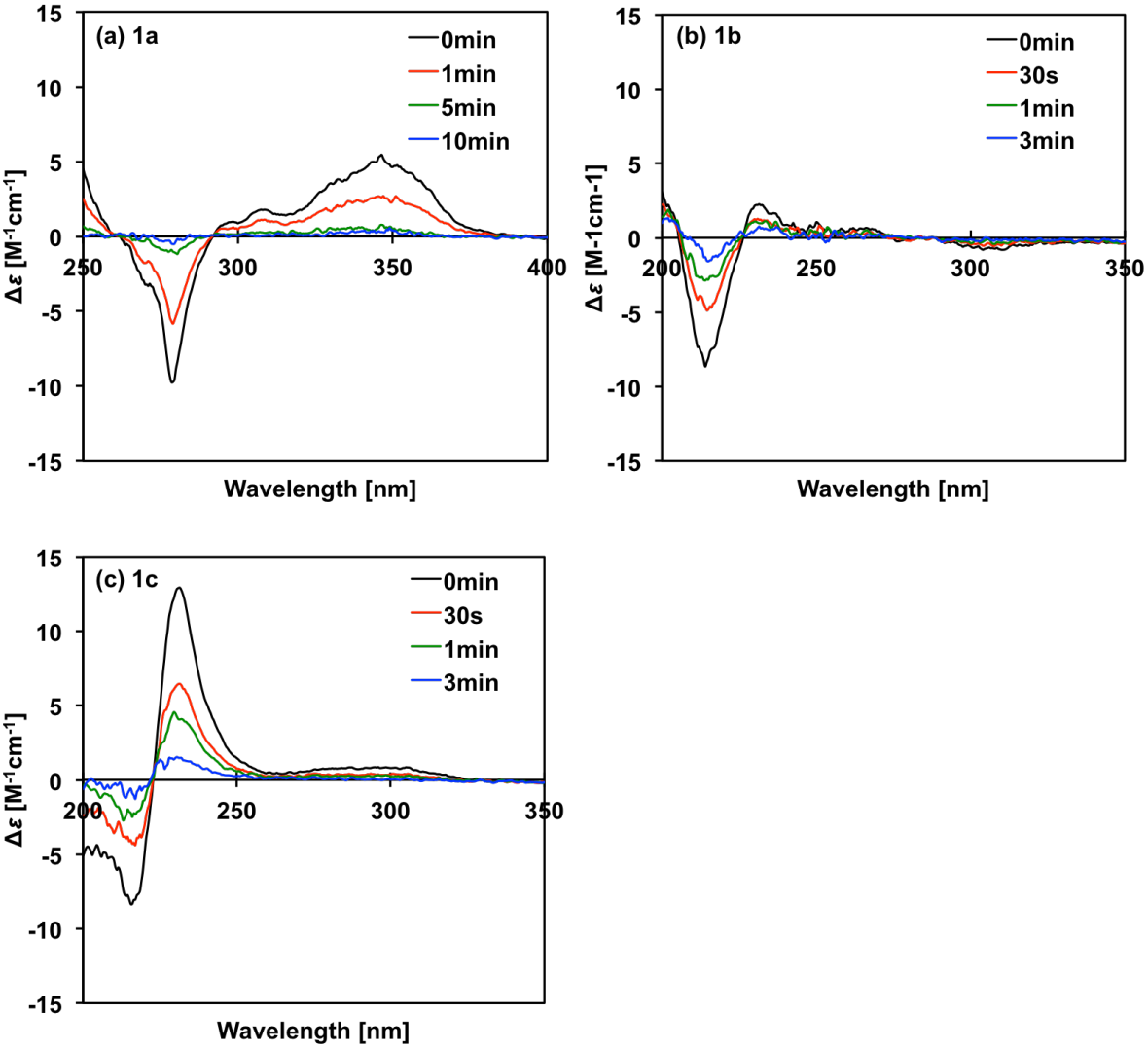

Figure 8. CD spectra of enantio enriched (a) **1a**, (b) **1b** and (c) **1c** taken upon photoirradiation every few times in CH_3CN (50 μM).

When the solution was photo irradiated, the CD intensity drastically decreased within a few minutes (Figure 8), suggesting that enantio-enriched **1a-c** became the racemic mixtures through the pyramidal inversion.

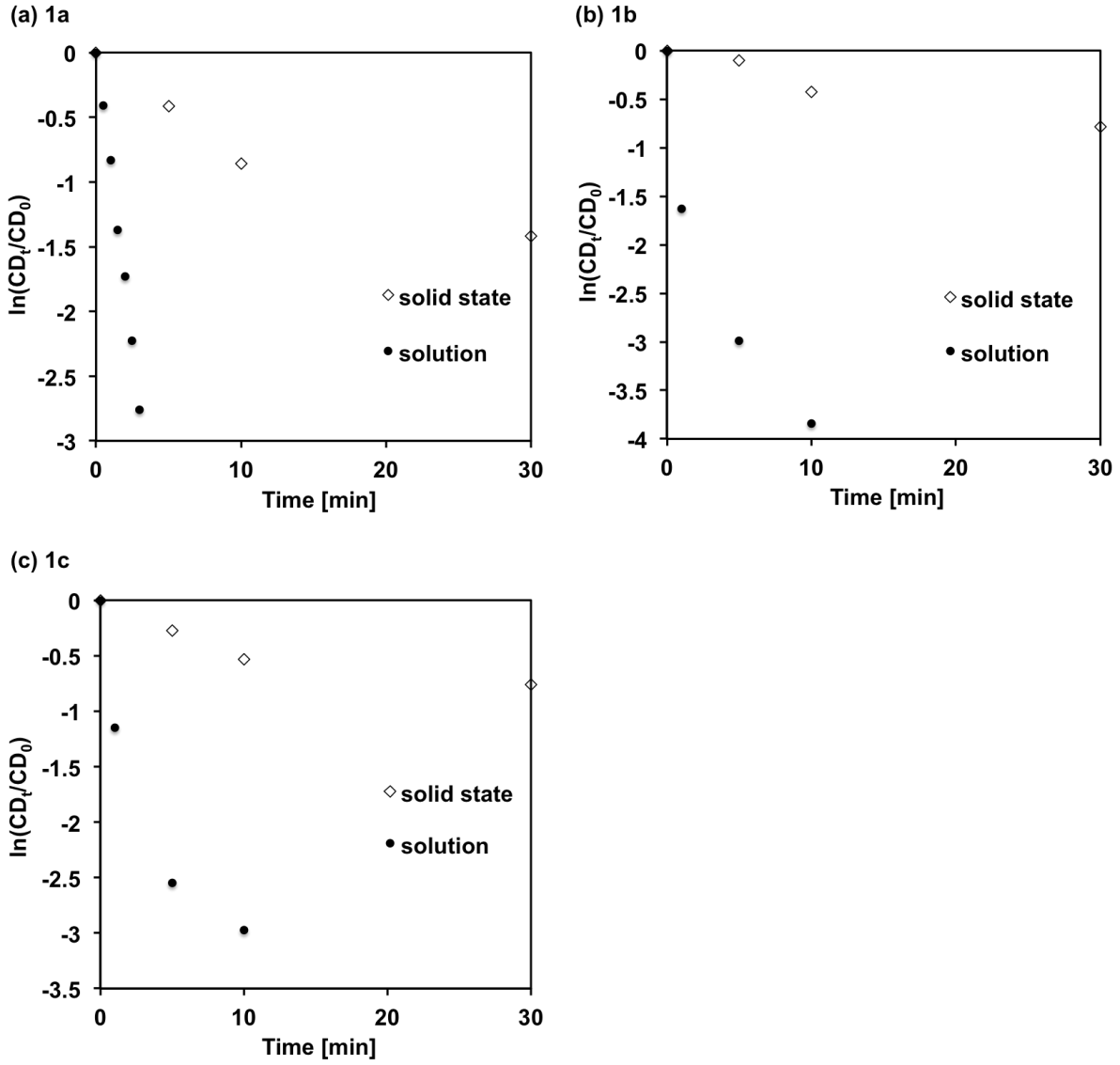

Figure 9. Time-dependent CD decay profiles of (a) **1a**, (b) **1b**, and (c) **1c** at the solid state.

In the solid state, they did not exhibit racemization even with long-time photoirradiation (Figure 9). In other words, the pyramidal inversion was suppressed in the solid state, which caused the strong photoluminescence (AIE behavior).

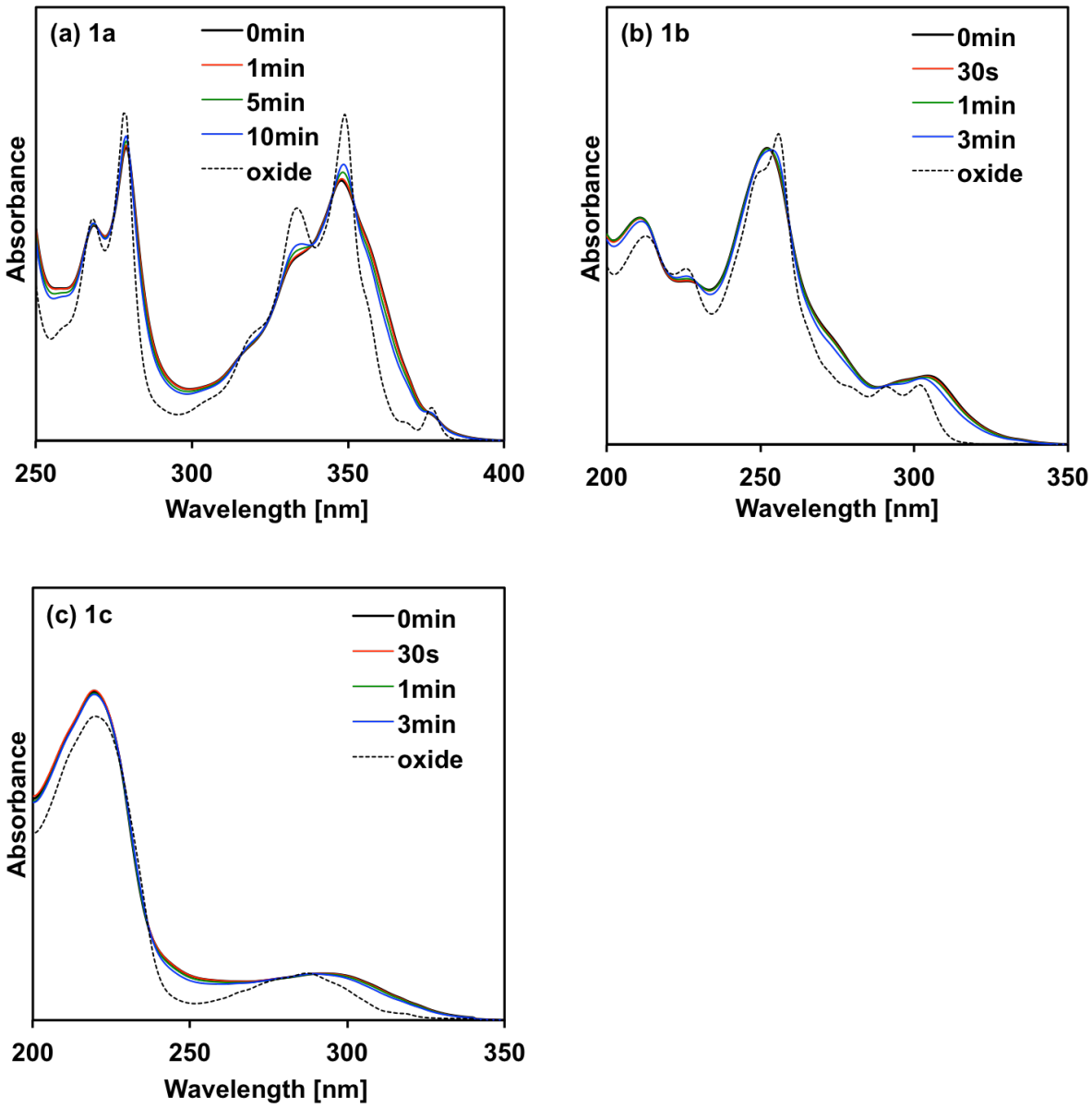

Figure 10. UV-vis absorption spectra of (d) **1a**, (e) **1b** and (f) **1c** taken upon photoirradiation every few times in CH_3CN (50 μM). Dashed lines show the spectra of the corresponding phosphine-oxides.

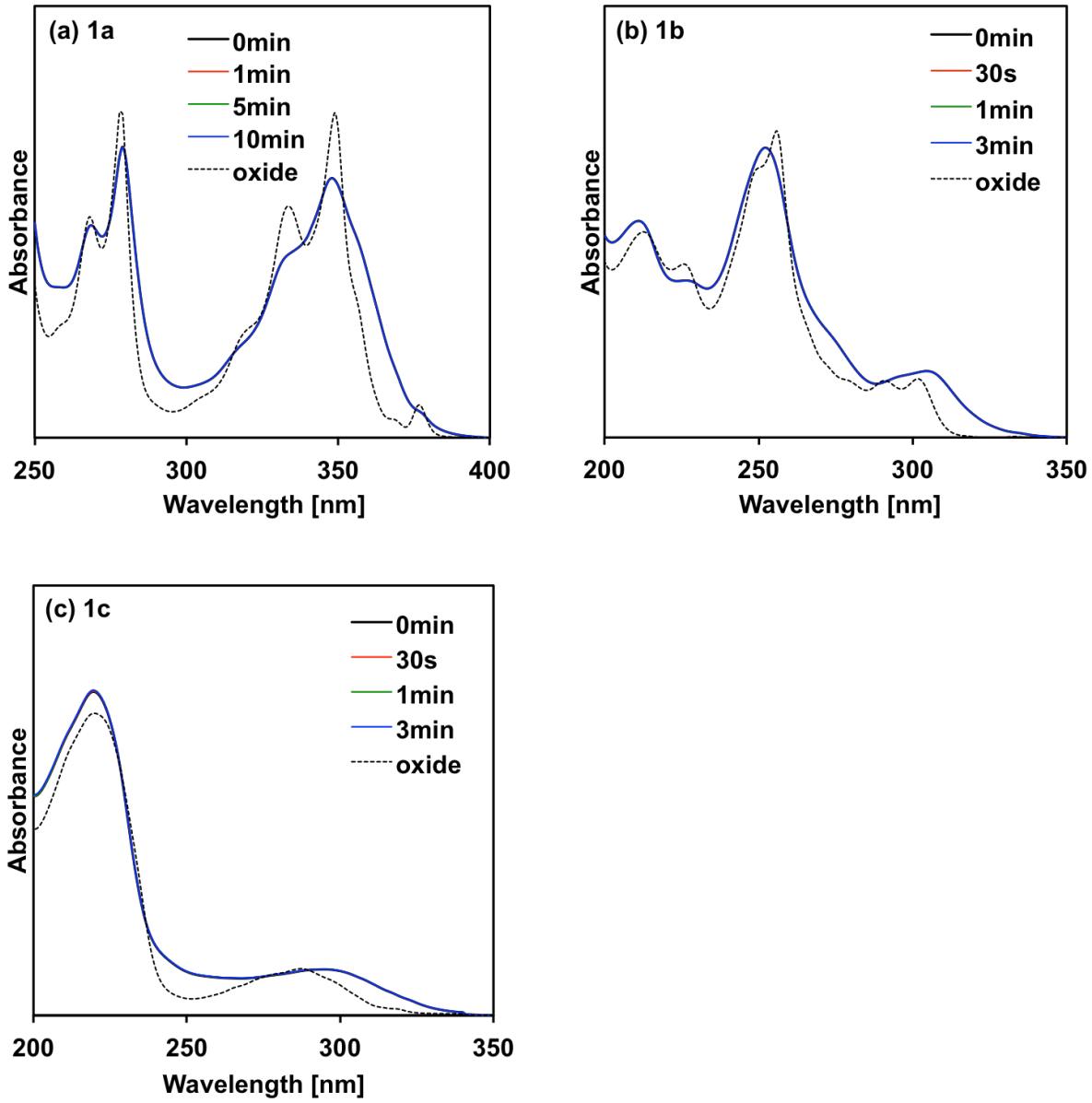

Figure 11. UV-vis absorption spectra of (d) **1a**, (e) **1b** and (f) **1c** taken upon photoirradiation every few times in "deoxygenated" CH_3CN (50 μM). Dashed lines show the spectra of the corresponding phosphine-oxides.

It has long been known that phosphines are easily photooxidized in the air.[38-40] Indeed, the absorption spectra slightly changed by the prolonged photoirradiation to the solution after disappearance of the CD intensity (Figure 10), which was attributed to the produce of phosphine-oxides (**1a-oxide**, **1b-oxide**, and **1c-oxide**). However, as was clear from comparing the CD and absorption spectra under photoirradiation, the photoracemization preceded much faster than photooxidation. In addition, the photooxidation was entirely inhibited in the deoxygenated CH_3CN solution (Figure 11).

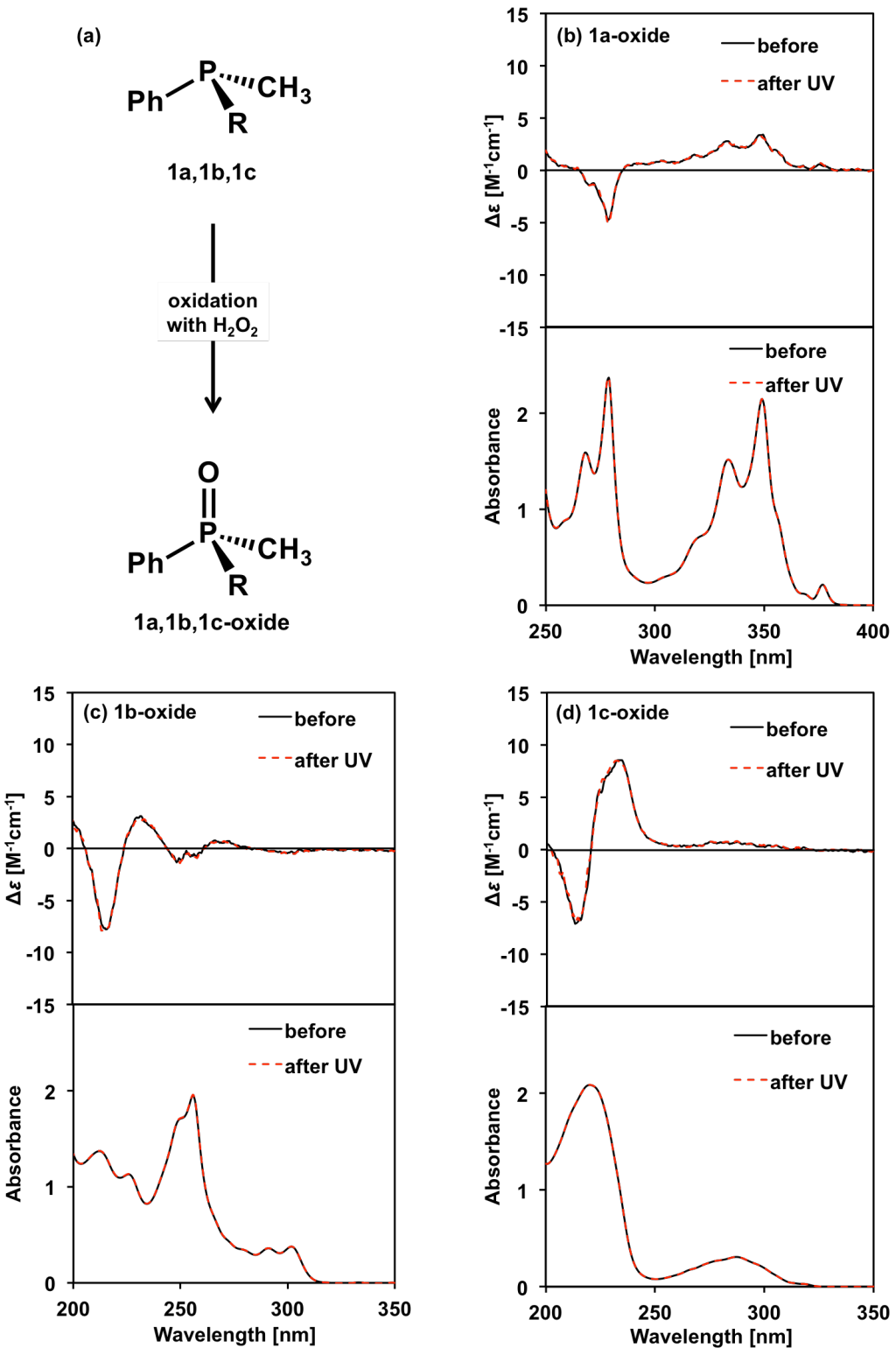

Figure 12. (a) Synthetic route for **1(a-c)**-oxides. CD and UV-vis absorption spectra of (b) **1a-oxide**, (c) **1b-oxide**, and (d) **1c-oxide** in CH_3CN before and after UV irradiation.

To carefully consider the influence of the photooxidation on the photoracemization, enantio-enriched phosphine-oxides were prepared by oxidation with H_2O_2 under dark conditions (Figure 12). Although **1a-c** were completely reacted to the **1a-oxide**, **1b-oxide**, and **1c-oxide**, but they retained their optical activity (Figure 13a). Furthermore, **1a-oxide**, **1b-oxide**, and **1c-oxide**, were not racemized even after one-hour photoirradiation (Figure 13b-d). From these experimental results, the photooxidation to phosphine-oxide did not affect the photoracemization at all. Note that the photooxidation was completely suppressed in the solid state.

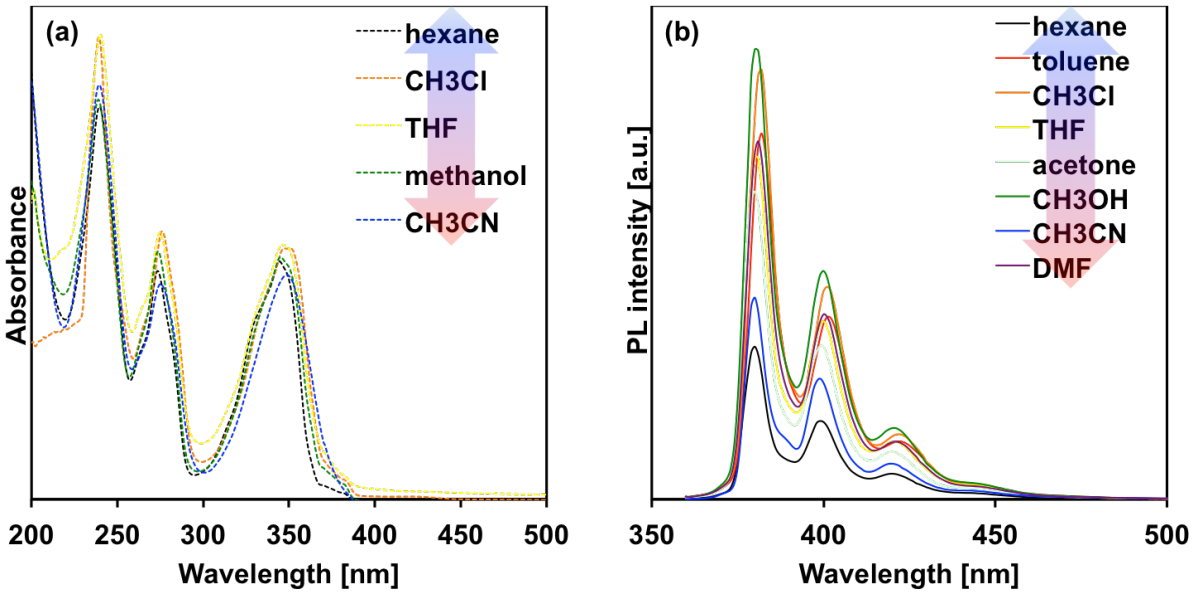

Figure 14. (a) UV-vis absorption and (b) photoluminescence (PL) spectra of **1a** in differenet solvents (10 μM).

Table 3. UV-vis absorption maxima (λ_{abs}) and emission maxima (λ_{em}) of **1a** in different solvents arranged in ascending order of dielectric constant (ε) from the left.

	hexane	toluene	CH_3Cl	THF	acetone	CH_3OH	CH_3CN	DMF
ε	1.88	2.38	4.81	7.58	20.7	32.7	37.5	38
λ_{abs} [nm]	240 273 344	-	239 276 350	240 275 346	-	239 274 345	239 275 349	-
λ_{em} [nm]	380 399 420	382 401 422	382 401 422	380 400 421	380 399 420	380 400 421	380 399 420	381 400 421

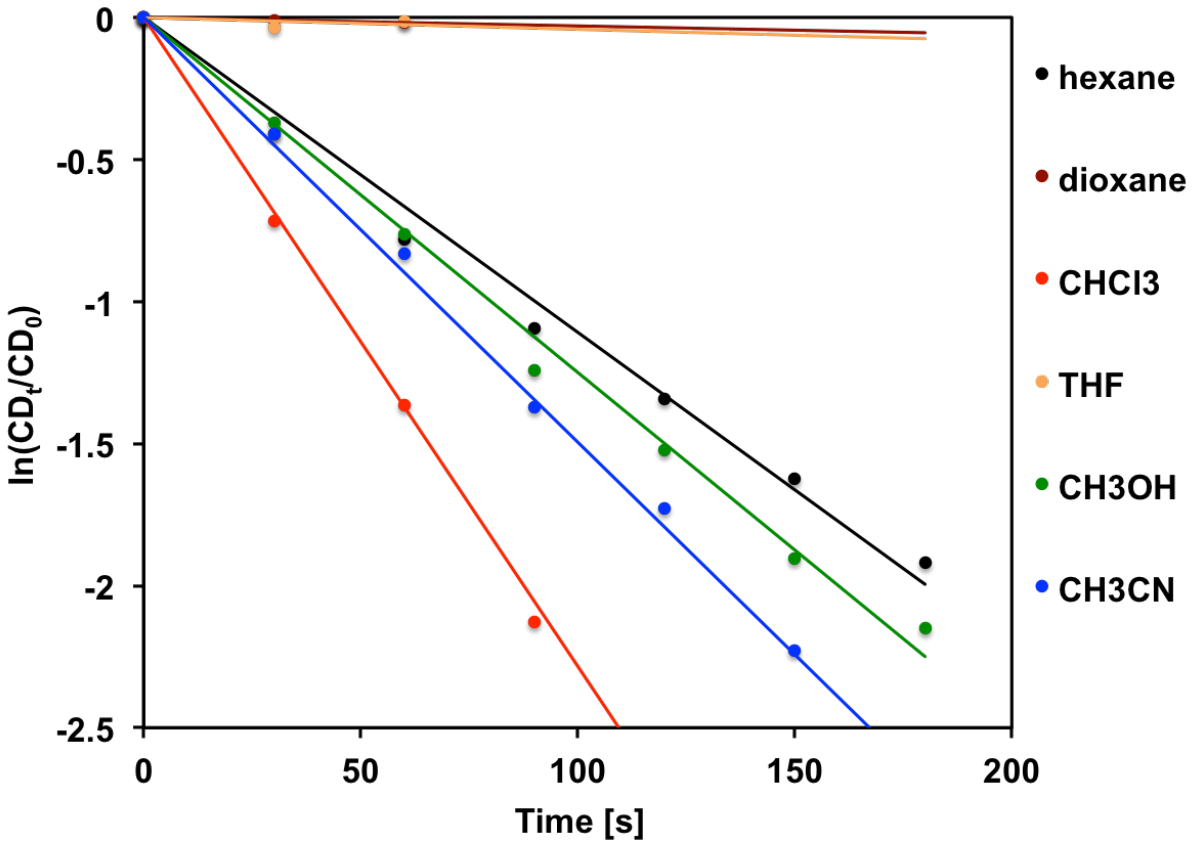

Figure 15. Time-dependent CD decay profiles of 1a in different solvents. These profiles were satisfied first-order kinetics, where the racemization rate constants (k_{rac}) were determind from the following formula(2). CD_t was the CD intensity at 280 nm taken upon photoirradiation

$$ln(\frac{CD_t}{CD_0}) = -k_{rac}t \quad \cdots \quad (2)$$

Table 4. Racemization rate constants (k_{rac}) in different solvents.

	hexane	dioxane	$CHCl_3$	THF	CH_3OH	CH_3CN
k_{rac} [$s^{-1}\times10^{-2}$]	1.1	- [a]	2.3	- [a]	1.3	1.5

[a] Photoracemization was not obersved

The excited-state molecular dynamics often differ from the solvents, thus the solvent dependency of UV-vis absorption and PL spectra of **1a** were measured in a variety of solvents. Even in the different solvents, the absorption and PL spectra were hardly changed (Figure 14 and Table 3). On the other hand, the photoracemization rate constants (k_{rac}) changed depending on the solvents (Figure 14 and Table 3). Note that, photoracemization was not observed at all in THF and dioxane. That was probably because the *O* atom of THF and dioxane coordinated to the *P* atom of **1a** in the excited state, thereby inhibiting the pyramidal inversion.

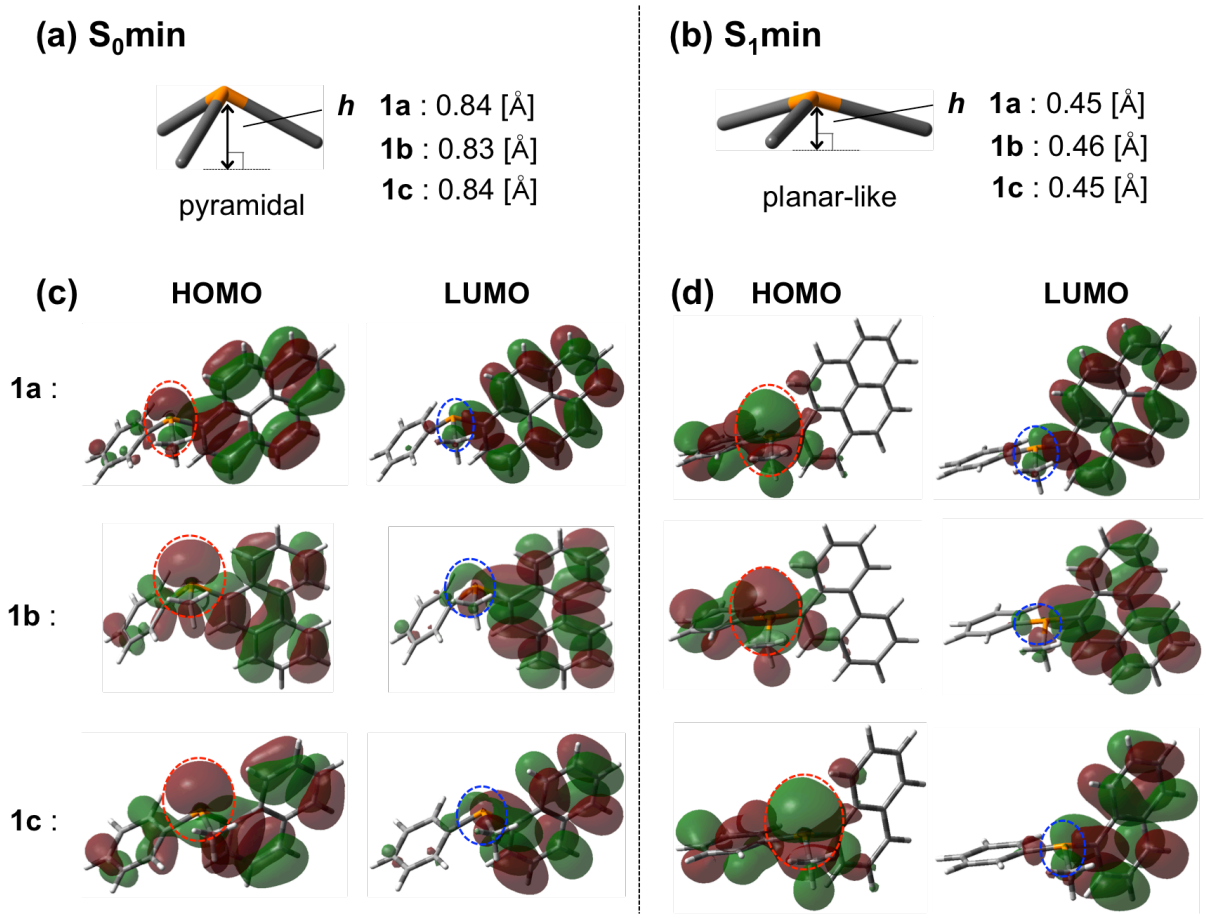

Figure 16. The height of the pyramid composed of PCCC (*h*) of **1a-c** at the (a) S_0min and (b) S_1min. The highest occupied molecular orbital (HOMO) and the lowest occupied molecular orbital (LUMO) of **1a-c** at the (c) S_0min and (d) S_1min. The orbitals around the *P* atoms are surrounded by dashed lines.

Table 5. S_0-S_1 transition properties of **1a-c**. Absorption wavelength maxima [λ_{abs}(meas.) and λ_{abs}(calc.)], and oscillator strength (f_{OS}) were obtained from UV-vis absorption spectrum measurements and DFT calculations, respectively. HOMO-LUMO ratio means the occupancy of HOMO-LUMO transition in the transition.

	1a	**1b**	**1c**
λ_{abs}(meas.) [nm]	344	302	292
λ_{abs}(calc.) [nm]	356	314	314
f_{OS}	0.29	0.12	0.10
HOMO-LUMO ratio	0.72	0.68	0.87

To obtain deeper insight into the pyramidal inversion behavior of *P*-stereogenic phosphines, theoretical computation were conducted regarding the minimum structures in the ground state (S_0min) and singlet excited state (S_1min) by density functional theory (DFT) and time-dependent DFT (TD-DFT) methods at the B3LYP[41,42]/6-31G(d) level using Gaussian 16.[43] The structural difference between the S_0min and S_1min were evident in the height of the pyramid composed of PCCC (*h*); the *h* at the S_0min were calculated to be 0.84 Å for **1a**, 0.83 Å for **1b**, and 0.84 Å for **1c**, respectively, while that at S_1min were 0.45 Å for **1a**, 0.46 Å for **1b**, and 0.45 Å for **1c**, respectively (Figure 15a and 15b). It could be explain from the electron densities of the highest occupied molecular orbital (HOMO) and the lowest occupied molecular orbital (LUMO) at the S_0min (Figure 15c). At the S_0min, the S_0-S_1 electronic transition was mainly derived from HOMO to LUMO, and the calculated energies corresponded well to the observed peaks in the UV-vis absorption spectra (Table 4). The electron density of HOMO was mainly distributed from PAHs moiety to *P* atom, while that of LUMO was localized in PAHs moiety, indicating that **1a-c** formed the intramolecular charge transfer (ICT) state from *P* atom to PAHs moieties after the S_0-S_1 electronic transitions. The ICT state promoted the planarization because it reduced the electronic repulsion between substituents and lone electron pairs on *P* atom. On the other hand, at S_1min, the relaxation pathway in the S_1 state was dominated by the spin-forbidden n-π* transition (Figure 15d) in which oscillator strength (*f*) was quite small (Table 4). From these results, I conclude that the non-radiative deactivation was accelerated by the planarization from the Flank-Condon (FC) structure.

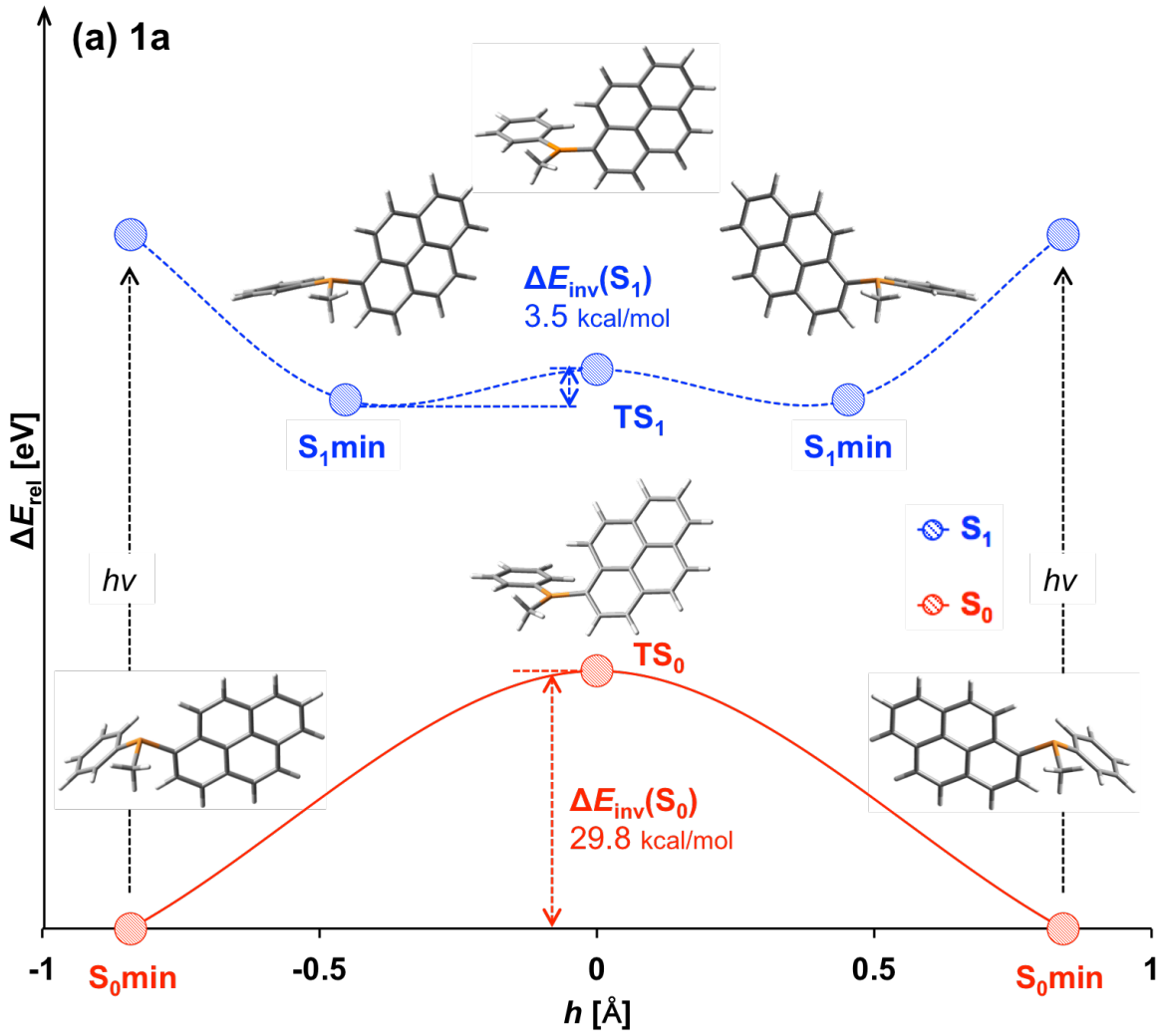

Figure 17. Pyramidal inversion diagrams of (a) **1a** in the S_0 state (red line) and S_1 state (blue line) obtained by the theoretical computations for the S_0min, S_1min, TS_0, and TS_1 along the *h*. Inset inversion barriers [$\Delta E_{inv}(S_0)$ or $\Delta E_{inv}(S_1)$] are measured from the energy differences between S_0min and TS_0, or S_1min and TS_1.

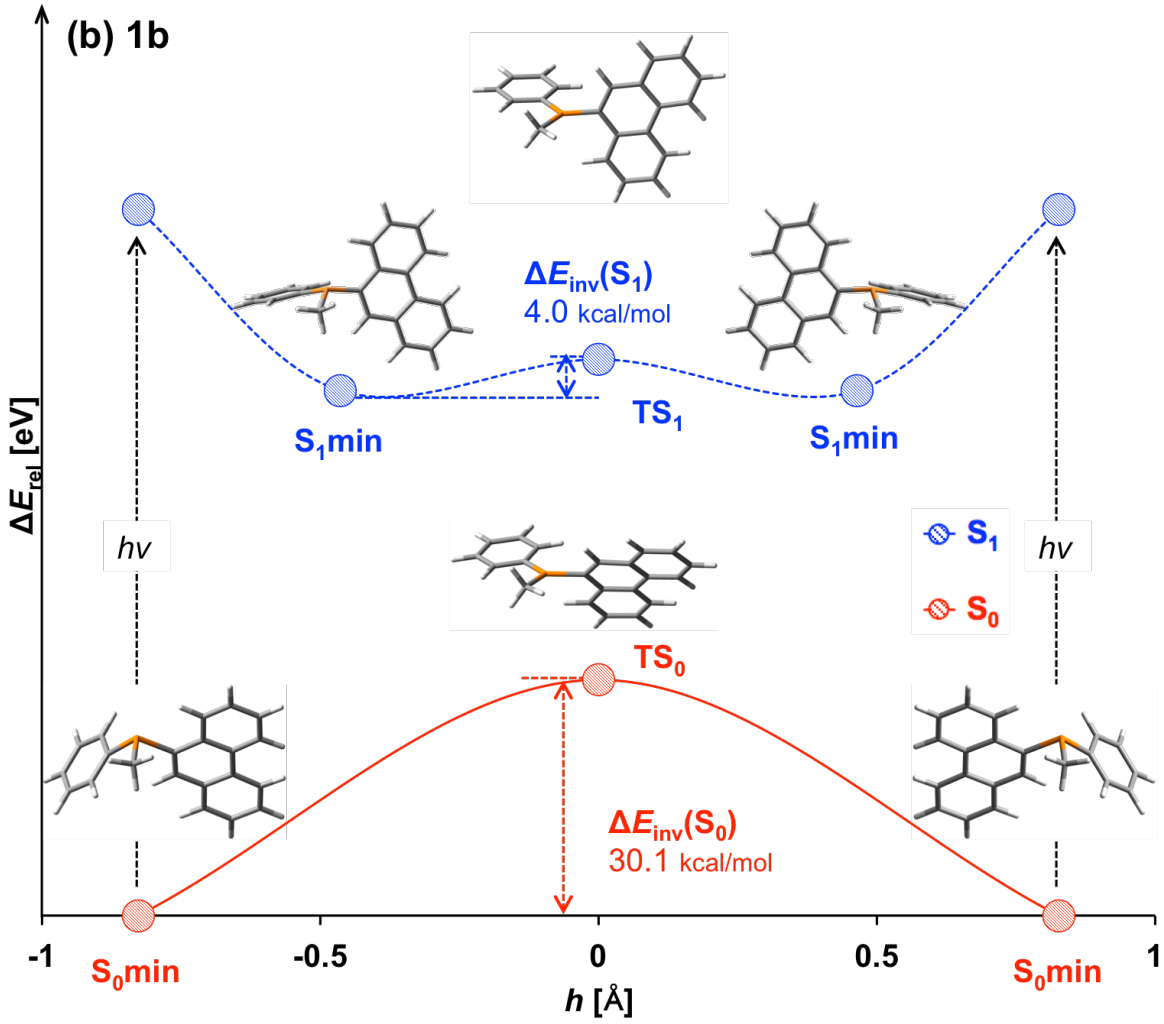

Figure 17 (*continued*). Pyramidal inversion diagrams of (b) **1b** in the S_0 state (red line) and S_1 state (blue line) obtained by the theoretical computations for the S_0min, S_1min, TS_0, and TS_1 along the *h*. Inset inversion barriers [$\Delta E_{inv}(S_0)$ or $\Delta E_{inv}(S_1)$] are measured from the energy differences between S_0min and TS_0, or S_1min and TS_1.

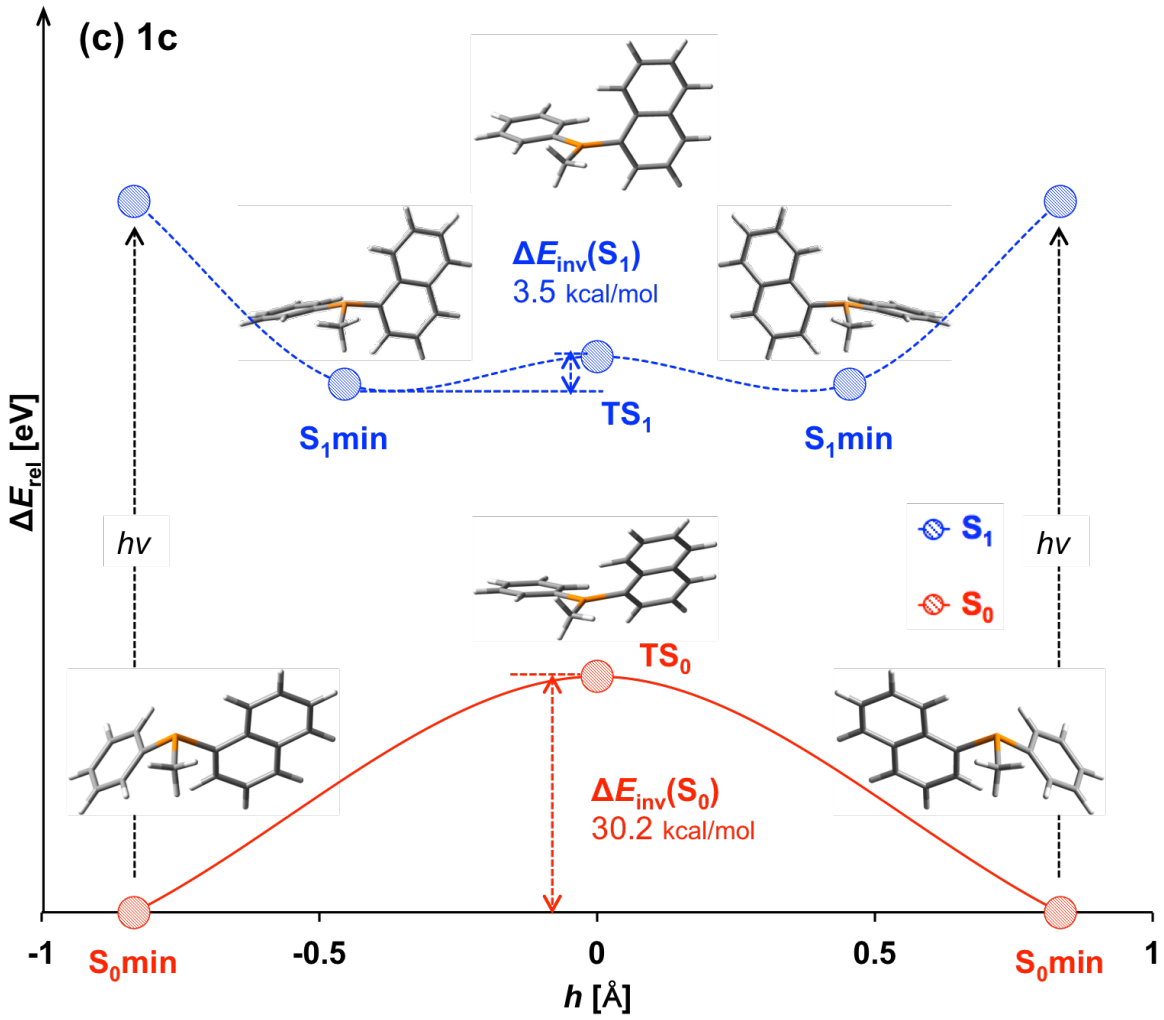

Figure 17 (*continued*). Pyramidal inversion diagrams of (c) **1c** in the S_0 state (red line) and S_1 state (blue line) obtained by the theoretical computations for the S_0min, S_1min, TS_0, and TS_1 along the *h*. Inset inversion barriers [$\Delta E_{inv}(S_0)$ or $\Delta E_{inv}(S_1)$] are measured from the energy differences between S_0min and TS_0, or S_1min and TS_1.

To estimate the inversion barrier of **1a-c** in the S_0 and S_1 state [$\Delta E_{inv}(S_0)$, $\Delta E_{inv}(S_1)$], energies and structural calculations of the transition state in the S_0 and S_1 state (TS_0, TS_1) were conducted by DFT and TD-DFT methods at the B3LYP[41,42]/6-31G(d). The energy diagrams in the S_0 and S_1 states are shown in Figure 17, in which the vertical axis is the relative energy ΔE_{rel} and the horizontal axis is *h*. $\Delta E_{inv}(S_0)$ was calculated to be 29.8 kcal/mol for **1a**, 30.1 kcal/mol for **1b**, and 30.0 kcal/mol for **1c**, respectively, while $\Delta E_{inv}(S_1)$ was much lower, i.e., 3.5, 4.0, and 3.5 kcal/mol respectively. Since the reaction with the activation energy less than 20 kcal/mol proceeds even at room temperature, **1a-c** undergo pyramidal inversion in the S_1 state before deactivation to the S_0 state.

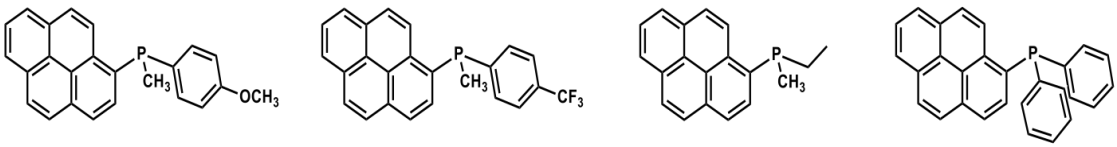

1d **1e** **2** **3**

Figure 18. Chemical structures of newly calculated phosphines **1d**, **1e**, **2**, **3**.

Table 6. Chemical structures including newly calculated phosphines **1d**, **1e**, **2**, **3** and the *h* at the S_0min, *h* at the S_1min, and $\Delta E_{inv}(S_1)$.

	1a	**1b**	**1c**	**1d***	**1e***	**2***	**3***
h at the S_0min [Å]	0.84	0.83	0.84	0.84	0.84	0.86	0.80
$\Delta E_{inv}(S_0)$ [kcal/mol]	29.8	30.1	30.2	31.0	28.6	33.6	26.7
h at the S_1min [Å]	0.45	0.46	0.45	0.48	0.44	0.61	0.40
$\Delta E_{inv}(S_1)$ [kcal/mol]	3.5	4.0	3.5	4.3	3.0	5.6	1.9

*calculation only

To elucidate the substituent effect of other phosphines on the photo-induced pyramidal inversion behavior, I compared $\Delta E_{inv}(S_0)$ and $\Delta E_{inv}(S_1)$ of **1a-c** and newly calculated phosphines **1d**, **1e**, **2**, and **3**. **1a** had electron-withdrawing substituent ($PhOCH_3$), **1e** had electron-donating one ($PhCF_3$), **2** was monoaryl- and **3** was triaryl-phosphines (Figure 18). $\Delta E_{inv}(S_0)$ was calculated to be **2** > **1d** > **1a-c** > **1e** > **3** (Table 6), which was consistent with the previously reported calculations.[28] As the steric bulk of the substituents increases, the steric repulsion within the pyramidal structure increases, which destabilizes pyramidal structure and leads to be lower $\Delta E_{inv}(S_0)$. The electron density on the *P* atom has also been cited as a factor affecting $\Delta E_{inv}(S_0)$. In this case, the electron-withdrawing substituent of **1e** decreased the electron density on the *P* atom, which stabilized the planar structure and leads to be lower $\Delta E_{inv}(S_0)$. **1d** had the opposite effect from **1e**. On the other hand, $\Delta E_{inv}(S_1)$ was calculated to be **2** > **1d** > **1b** > **1a**, **1c** > **1e** > **3**, which was almost the same order to $\Delta E_{inv}(S_0)$ and the same order to *h* at the S_1min. This result suggested that stability of pyramidal structure was also important in the excited state. The bulkiness and electron withdrawing effect destabilize the pyramidal structure in the excited state, which consequently leads to lower $\Delta E_{inv}(S_1)$.

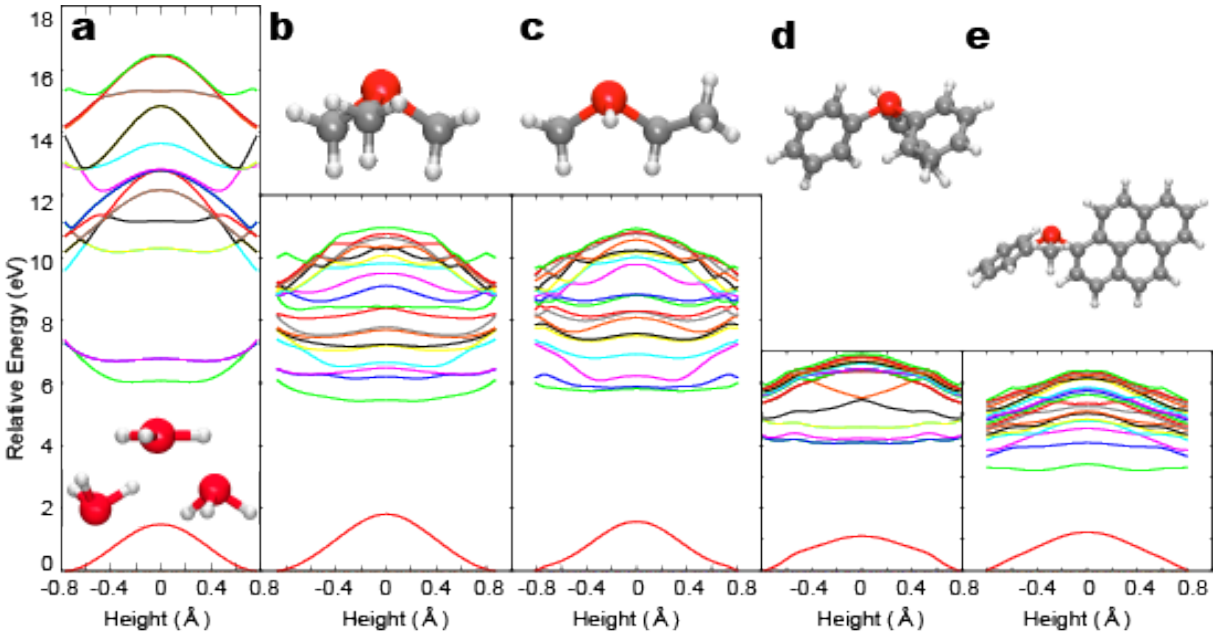

Figure 19. The potential energy curves along the IRC pathways for the inversion mode in the ground electronic states for molecules (a) PH3, (b) PMe3, (c) PHMeEt, (d) PPh3, and (e) **1a**, whose geometric structures are shown in the inset.

In the above discussions, I focused on the narrow range of PAH-containing phosphines, which might limited a wide range of applications. Thus, in order to examine whether photo-induced pyramidal inversion also occurs in common phosphines or not, I calculated S_0-S_{20} energy curves of PH_3, PMe_3, PHMeEt, PPh_3 and **1a** (Figure 19). The inversion pathway in the S_0 state was determined by the intrinsic reaction coordinates (IRC) calculation from the transition state for the inversion mode. In the S_0 state, all phosphines had a large upward convex curves, as previously known. The energy curves in the S_1-S_{20} were calculated using linear response TD-DFT calculations along the IRC pathway in the S_0 state. In the low-lying excited state including the S_1 state, all phosphines had downward convex or nearly flat curves. However, the upward convex curve was obtained only in some highly excited state. These results suggested not only PAH-containing phosphines, but also common phosphines presumably exhibited photo-induced pyramidal inversion.

Conclusion

In this Chapter, inspired by the report on AIE behavior of triphenylphosphine derivatives, I investigated the photo-induced pyramidal inversion behavior of phosphines. Three kinds of PAH-containing phosphines were synthesized by stepwise Grignard reactions. Unlike typical AIEgens, PAH-containing phosphines showed weak emission even in the diluted solution, but emission intensity definitely decreased compared with the corresponding PAHs. As I expected, *P*-stereogenic phosphines exhibited photo-induced pyramidal inversion in the diluted solution, and the inversion process was so fast that it was not affected by slow photooxidation. The theoretical computations revealed that PAH-containing phosphines formed ICT state after the excitation, and the consequent planarization accelerated the non-radiative decay process from the excited state. Therefore, they showed AIE-like behavior. According to the energy calculations about the planar transition state, $\Delta E_{inv}(S_1)$ of phosphines were quite lower than the $\Delta E_{inv}(S_0)$ because of the planarization in the excited state. In addition, it was revealed that the substituent effect on $\Delta E_{inv}(S_1)$ was almost the same on $\Delta E_{inv}(S_0)$. Furthermore, additional calculations suggested that the decrease of $\Delta E_{inv}(S_1)$ was not specific to PAH-containing phosphines, but was also observed in common phosphines such as PH_3 and PMe_3. These findings are important not only in terms of new photophysical properties of phosphines, but also in terms of applications to molecular machines, smart luminescence materials, asymmetric synthesis and the like.

Experimental Section

Materials and General Measurements. All other reagents were obtained from commercial sources and used without further purification. The reaction was carried out under nitrogen atmosphere. In all photoexperiments, solvents for spectrochemical analysis were used. NMR measurements of ^{1}H (500 MHz) with tetramethylsilane as an internal standard, ^{13}C (126 MHz), ^{31}P(203 MHz) with phosphoric acid as an internal standard were recorded on a Bruker Biospin AVANCE DRX500 instrument. Electrospray ionization mass spectroscopy (ESI-MS) was carried out at Global facility center, Hokkaido University. UV-Vis spectra were recorded on a JASCO V-570 spectrophotometer. Emission spectra were obtained with SHIMADZU RF5300PC spectrofluorometer. The relative luminescence quantum yield (Φ_F) was measured by following procedure. Circular dichroism spectra were measured by JASCO J-720 spectropolarimeter with SCINICS Cool Circular CH-201. Chiral column chromatography was carried out on a SHIMAZU LC-9A system (DAICEL CHIRALPAK IF column) with a SHIMAZU RID-10A reflective index. Photoirradiation was carried out by following procedure with USHIO Deep UV lamp UXM-500SX as a light source.

X-ray crystallography analysis. Single-crystal of **1b** was mounted in the loop using paraffin oil. The data were collected on a Rigaku XtaLAB Synergy-S with graphite monochromated Cu Kα radiation (λ = 1.5418 Å) and a PhotonJet-S microfocus generator operating at 50 kV and 1 mA. Diffraction data were collected and processed using the CrysAlisPro program. Structures were solved by direct methods using SHELXS.[44] Structural refinements were conducted by the full-matrix least-squares method using SHELXS.[44] Non-H atoms were refined anisotropically, and H atoms were refined using a riding model. All calculations were performed using the OLEX2[45] software packages.

Quantum yield. Relative quantum yield of **1a-c** were measured in the 10 μM CH_3CN solutions with the corresponding PAHs as standards (**1a**: pyrene, **1b**: phenanthrene, **1c**: naphthalene). The quantum yields of PAHs in CH_3CN were determined with the reported quantum yields in cyclohexane or ethanol as standards.[46,47] All measurements were carried out in the same experimental settings: excitation wavelength, slit widths, photomultiplier voltage.

Photoirradiation. The ranges of photo-irradiating wavelength were narrowed down using band-pass filter. In the case of **1a** that was 290-370 nm of half width by using HOYA COLORED OPTICAL GLASS HA50 and U340, and in the case of **1b** or **1c**, those were 220-300 nm of half-width by using ASAHI SPECTRA SU0300. The target solutions in 1×1×5 cm^3 quartz cell were covered with black sample holder to make the photoreaction slowly, therefore the irradiated area was reduced to be 0.78 cm^2. The energy density of light source was 6.28 mW/cm^2 that was measured by THORLABS PM100D digital power meter equipped with S310C thermal sensor.

Calculations. Calculations of PAH-containing phosphines were performed by DFT and TD-DFT at the B3LYP[57,58]/6-31G(d) level using Gaussian16. TS_0 and TS_1 were determined with Berny method and confirmed by frequency calculations at the levels of B3LYP[41,42]/6-31G(d). Single-point electronic energies were calculated by TD-DFT at the B3LYP[41,42]/6-31G(d) level. Molecular orbitals were visualized in Gaussview. Calculations of common phosphines were performed using the B3LYP/def2-TZVP[48] level, under the resolution of identity approximation for the Coulomb integral,[49] as implemented in TURBOMOLE.[50,51] IRC pathways were calculated for positive side using the DRC script.[52] In the excited state calculations along the IRC, we reduce the number of points because the IRC for PPh_3 and **1a** consist of 7800 and 8300 geometries, respectively. For PH_3, PMe_3, the IRC pathways for the positive and negative were confirmed to be the same. The energy curves are obtained using the ground and excited state energies along the positive IRC by mirroring for the negative directions for visibility.

Synthetic procedure and characterization.

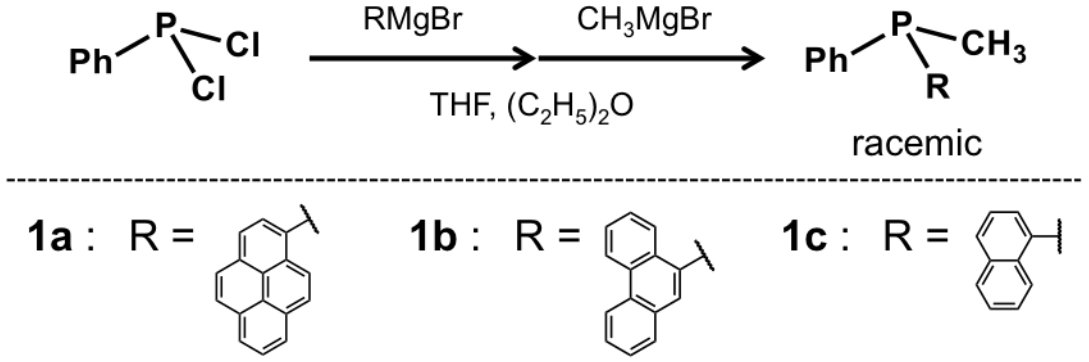

Scheme 1. Synthetic route of racemic phosphines **1a**, **1b**, and **1c**.

A dry 100 mL eggplant flask was charged with magnesium turnings (9.24 mmol, 1.3 eq) and heated by heatgun for 30 min. After cooling, anhydrous THF (3 mL) and a small amount of 1,2-dibromoethane were added. Then brominated aromatic compound [(**1a**: 1-bromopyrene, **1b**: 9-bromophenanthrene, **1c**: 1-bromonaphthalene), 7.11 mmol, 1eq)] in anhydrous THF (5 mL) was slowly added over a period of 30 minutes, and resulting mixture was stirred at 45 °C for two more hours. After cooling, dark brown solution (RMgBr) was obtained.

In a dry 100 mL eggplant flask, dichrolophenylphosphine (7.11 mmol, 1eq) and diethylether (10 mL) were added. After the solution was cooled to -78 °C with dry ice/acetone, RMgBr was dropwised over 30 minutes. The solution was stirred at room temperature for two hours before being cooled to -78 °C once more. A 3M MeMgBr / diethylether solution (4.7 mL, 14.2 mmol, 2 eq) was added over 30 min, and the mixture was then stirred at room temperature overnight. The reaction was quenched with distilled water. After distilling off THF, the residue was extracted with CH_2Cl_2 and washed with distilled water. The organic layer was combined, dried over with $MgSO_4$ and the solvent was removed under reduced pressure. After the purification of the crude product by chromatography on SiO_2 (n-hexane/$CHCl_3$), racemic mixture was obtained.

1a : (17 %): ^{1}H NMR (500 MHz, CD_3CN) δ (ppm): 1.82 (3H, d, J = 4.3 Hz), 7.26-7.31 (3H, m), 7.36-7.42 (2H, m), 8.04-8.20 (5H, m), 8.24-8.30 (3H, m), 8.79-8.84 (1H, dd, J = 9.3, 5.1 Hz). ^{31}P NMR (203 MHz, CD_3CN) δ (ppm): -39.57. ^{13}C NMR (126 MHz, $CDCl_3$) δ (ppm):

12.51, 124.63, 124.92, 125.34, 125.41, 126.01, 127.40, 127.68, 128.12, 128.47, 128.76, 130.91, 131.32, 131.78, 131.82, 132.01, 133.82, 134.21, 140.60. HRMS(ESI) Calcd. for $C_{23}H_{17}P$ $[M+H]^+$: *m*/*z* 325.1141 Found: *m*/*z* 325.1139.

1b : (26 %): ^{1}H NMR (500 MHz, CD_3CN) δ (ppm): 1.75 (3H, d, *J* = 4.1 Hz), 7.27-7.32 (3H, m), 7.43-7.49 (2H, m), 7.51-7.56 (1H, m), 7.63-7.69 (2H, m), 7.69-7.74 (1H, m), 7.95-8.00 (2H, m), 8.40 (1H, dd, *J* = 7.4, 4.8 Hz), 8.75 (1H, d, *J* = 8.2 Hz), 8.79 (1H, d, *J* = 8.5 Hz). ^{31}P NMR (203 MHz, CD_3CN) δ (ppm): -37.13. ^{13}C NMR (126 MHz, $CDCl_3$) δ (ppm): 12.40, 122.52, 122.99, 126.54, 126.74, 126.94, 127.15, 128.50, 128.74, 130.17, 130.64, 131.39, 132.30, 133,10, 134.98, 139.58. HRMS(ESI) Calcd. for $C_{21}H_{17}P$ $[M+H]^+$: *m*/*z* 301.1141 Found: *m*/*z* 301.1139.

1c : (14 %): ^{1}H NMR (500 MHz, CD_3CN) δ (ppm): 1.68 (3H, d, *J* = 4.1 Hz), 7.28-7.32 (3H, m), 7.37-7.42 (2H, m), 7.44-7.57 (3H, m), 7.58-7.63 (1H, m), 7.91 (2H, d, *J* = 8.3 Hz), 8.41 (1H, dd, *J* = 8.2, 4.1 Hz). ^{31}P NMR (203 MHz, CD_3CN) δ (ppm): -38.04. ^{13}C NMR (126 MHz, $CDCl_3$) δ (ppm): 12.27, 125.52, 125.88, 126.09, 128.34, 128.45, 128.66, 129.26, 132.17, 133.45, 135.20, 136.61, 139.87. HRMS(ESI) Calcd. for $C_{17}H_{15}P$ $[M+H]^+$: *m*/*z* 251.0984 Found: *m*/*z* 251.0983.

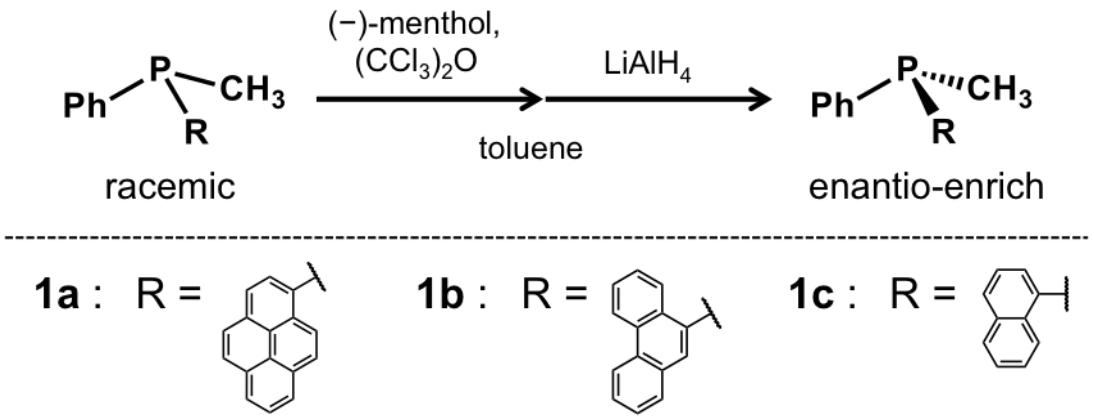

Scheme 1. Synthetic route of enantio enriched **1a**, **1b**, and **1c**.

Aasymmetric Appel reaction and subsequent reduction were carried out followed the procedure of Gilheany.[1] In a 50 mL eggplant flask, racemix mixture of phosphine [(**1a**, **1b** or **1c**), 0.55 mmol, 1 eq] and anhydrous toluene (5 mL) was added. In another 50 mL eggplant flask, (−)-menthol (0.715 mmol, 1.3 eq) and $(CCl_3)_2O$ (0.55 mmol, 1 eq) in anhydrous toluene (5 mL) was prepared. After both flasks were cooled to -78 °C with dry ice/acetone, phosphine solution was added dropwise into (−)-menthol and $(CCl_3)_2O$ solution. Resulting mixture was stirred at -78 °C for 10 minutes, then $LiAlH_4$ (2.75 mmol, 5 eq) in anhydrous toluene (5 mL) was added. The reaction was quenched with distilled water keeping the temperature at room temperature. After filtration, organic layer was separated and aqueous layer was extracted with CH_2Cl_2. The organic layer was combined, dried over with $MgSO_4$ and the solvent was removed under reduced pressure. After the purification by chromatography on SiO_2 (n-hexane/$CHCl_3$), product was identified with the same structure as the reactant phosphine by ^1H NMR and ^{31}P NMR spectra.

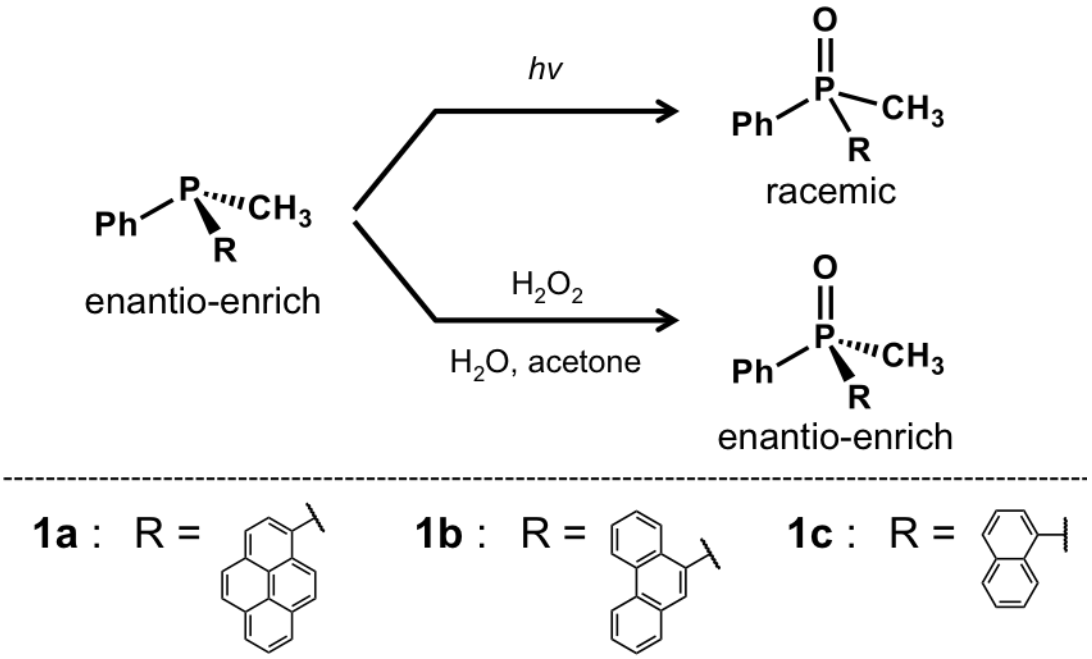

Scheme 1. Synthetic route of phosphine-oxides.

Method A (with racemization): A solution of phosphine (**1a**, **1b** or **1c**) in CH_3CN was photoirradiated until absorption spectrum was no longer changed.

Method B (without racemization): In a solution of phosphine (**1a**, **1b** or **1c**) in acetone (10 mL), distilled water (2 mL) and 30 % H_2O_2/H_2O (2 mL) were added, and the resulting mixture was stirred at room temperature under dark condition. After distilling off acetone, aqueous layer was extracted with CH_2Cl_2. The organic layer was combined, dried over with $MgSO_4$ and the solvent was removed under reduced pressure.

1a-oxide: ^{1}H NMR (500 MHz, CD_3CN) δ (ppm): 2.26 (3H, d, *J* = 13.4 Hz), 7.43-7.49 (2H, m), 7.49-7.55 (1H, m), 7.11-7.77 (2H, m), 8.08-8.13 (1H, t, *J* = 7.6 Hz), 8.15 (1H, d, *J* = 9.3 Hz), 8.19 (1H, d, *J* = 9.1 Hz), 8.25-8.36 (4H, m), 8.37-8.43 (1H, dd, *J* = 13.1, 8.0 Hz), 8.89 (1H, d, *J* = 9.4 Hz). ^{31}P NMR (203 MHz, CD_3CN) δ (ppm): 29.88. HRMS(ESI) Calcd. for $C_{23}H_{17}OP$ $[M+H]^+$: *m*/*z* 341.1090 Found: *m*/*z* 341.1088.

1b-oxide : ^{1}H NMR (500 MHz, CD_3CN) δ (ppm): 2.18 (3H, s), 7.43-7.48 (2H, m), 7.49-7.55 (2H, m), 7.64-7.69 (1H, m), 7.70-7.79 (3H, m), 7.80-7.85 (1H, m), 8.11 (1H, d, *J* = 8.0 Hz), 8.39 (1H, *J* = 16.4 Hz), 8.52 (1H, d, *J* = 8.5 Hz), 8.80 (2H, dd, *J* = 12.1, 8.5 Hz). ^{31}P NMR

(203 MHz, CD_3CN) δ (ppm): 29.49. HRMS(ESI) Calcd. for $C_{21}H_{17}OP$ $[M+H]^+$: *m*/*z* 317.1090 Found: *m*/*z* 317.1090.

1c-oxide : ^1H NMR (500 MHz, CD_3CN) δ (ppm): 2.12 (3H, d, *J* = 13.4 Hz), 7.43-7.49 (3H, m), 7.49-7.55 (2H, m), 7.59-7.64 (1H, m), 7.66-7.62 (2H, m), 7.94-8.01 (1H, m), 8.12 (1H, d, *J* = 8.6 Hz), 8.49 (1H, d, *J* = 8.5 Hz). ^{31}P NMR (203 MHz, CD_3CN) δ (ppm): 29.34. HRMS(ESI) Calcd. for $C_{17}H_{15}OP$ $[M+H]^+$: *m*/*z* 267.0933 Found: *m*/*z* 267.0933.

References

[1] J. Luo, Z. Xie, J. W. Y. Lam, L. Cheng, H. Chen, C. Qiu, H. S. Kwok, X. Zhan, Y. Liu, D. Zhu, B. Z. Tang, *Chem. Commun.* **2001**, 1740–1741.

[2] X. L. Peng, S. R. Barragan, Z. S. Li, Q. S. Li, L. Blancafort, *J. Mater. Chem. C* **2016**, *4*, 2802–2810.

[3] J. Sturala, M. K. Etherington, A. N. Bismillah, H. F. Higginbotham, W. Trewby, J. A. Aguilar, E. H. C. Bromley, A. J. Avestro, A. P. Monkman, P. R. McGonigal, *J. Am. Chem. Soc.* **2017**, *139*, 17882–17889.

[4] B. Ventura, Y. M. Poronik, I. Deperasinska, D. T. Gryko, *Chem. Eur. J.* **2016**, *22*, 15380–15388.

[5] S. Sasaki, S. Suzuki, W. M. C. Sameera, K. Igawa, K. Morokuma, G. i. Konishi, *J. Am. Chem. Soc.* **2016**, *138*, 8194–8206.

[6] S. Sasaki, S. Suzuki, K. Igawa, K. Morokuma, G. I. Konishi, *J. Org. Chem.* **2017**, *82*, 6865–6873.

[7] S. Suzuki, S. Maeda, K. Morokuma, *J. Phys. Chem.* A **2015**, *119*, 11479–11487.

[8] Z. Zhao, X. Zheng, L. Du, Y. Xiong, W. He, X. Gao, C. Li, Y. Liu, B. Xu, J. Zhang, F. Song, Y. Yu, X. Zhao, Y. Cai, X. He, R. T. K. Kwok, J. W. Y. Lam, X. Huang, D. L. Phillips, H. Wang, B. Z. Tang. *Nat. Commun.* **2019**, *10*, 2952.

[9] K. Kokado, Y. Chujo, *Macromolecules*, **2009**, *42*, 1418–1420.

[10] K. Tanaka, K. Nishino, S. Ito, H. Yamane, K. Suenaga, K. Hashimoto, Y. Chujo, *Faraday Discuss.* **2017**, *196*, 31–42

[11] M. Dommett, R. Crespo-Otero, *Phys. Chem. Chem. Phys.* **2017**, *19*, 2409–2416.

[12] R. C. Otero, Q. Li, L. Blancafort, *Chem. Asian. J.* **2019**, *14*, 700–714.

[13] K. Kokado, K. Sada, *Angew. Chem. Int. Ed.* **2019**, *58*, 8632–8639.

[14] G. Bettermann, W. Krause, G. Riess, T. Hofmann, Phosphorous Compounds, Inorganic, *"Ulmann's Encyclopedia of Reagents for Organic Synthesis (e-EROS)"*, Wiley-VCH, Weinheim, vol. 27, **2000**.

[15] D. Blunk, P. Bierganns, N. Bongartz, R. Tessendorf, C. Stubenrauch, *New J. Chem.* **2006**, *30*, 1705-1717.

[16] C. Queffelec, M. Petit, P. Janvier, D. A. Knight, B. Bujoli. *Chem. Rev.* **2012**, *112*, 3777-3807.

[17] H. Guo, Y. C. Fan, Z. Sun, Y. Wu, O. Kwon, Chem. Rev. 2018, *118*, 10049-10293.

[18] P. Natarajan, *Anal. Methods,* **2014**, *6*, 2432–2435.

[19] P. Xue, P. Wang, P. Chen, J. Ding, R. Lu, *RSC Adv.* **2016**, 6, 51683–51686.

[20] R. D. Baechler, W. B. Farnham, K. Mislow, *J. Am. Chem. Soc.* **1969**, *91*, 5686.

[21] J. M. Lehn, B. Munsch, *J. Chem. Soc. D* **1969**, 1327–1329.

[22] R. D. Baechler, K. Mislow, *J. Am. Chem. Soc.* **1970**, *92*, 3090–3093.

[23] J. B. Lambert, G. F. Jackson, III, D. C. Mueller, *J. Am. Chem. Soc.* **1970**, *92*, 3093-3097.

[24] R. D. Baechler, K. Mislow, *J. Am. Chem. Soc.* **1970**, *92*, 4758–4759.

[25] K. Mislow, R. D. Baechler, *J. Am. Chem. Soc.* **1971**, *93*, 773–774.

[26] K. Mislow, W. Egan, *J. Am. Chem. Soc.* **1971**, *93*, 1805–1806.

[27] W. Egan, R. Tang, G. Zon. K. Mislow, *J. Am. Chem. Soc.* **1971**, *93*, 6205–6216.

[28] C. D. Montgomery, *J. Chem. Educ.* **2013**, *90*, 661–664.

[29] K. D. Reichl, D. H. Ess, A. T. Radosevich, *J. Am. Chem. Soc.* **2013**, *135*, 9354–9357.

[30] K. Fujimoto, A. Osuka, *Chem. Sci.* **2017**, *8*, 8231–8239.

[31] K. Mislow, M. Axelrod, D. R. Rayner, H. Gotthardt, L. M. Coyne, G. S. Hammond, *J. Am. Chem. Soc.* **1965**, *87*, 4958–4959.

[32] G. Balavoine, S. Juge, H. B. Kagan, *Tetrahedron Lett.* **1973**, *14*, 4159–4162.

[33] Y. Tsurutani, K, Ishida, H. Nakano, K. Hirao, *J. Photochem. Photobiol. A: Chem.* **1999**, *122*, 161–168.

[34] R. S. Kathayat, L. Yang, T. Sattasathuchana, L. Zoppi, K. K. Baldridge, A. Linden, N. S. Finney, *J. Am. Chem. Soc.* **2016**, *138*, 15889–15895.

[35] E. Bergin, C. T. O'Connor, S. B. Robinson, E. M. McGarrigle, C. P. O'Mahony, D. G. Gilheany, *J. Am. Chem. Soc.* **2007**, *129*, 9566–9567

[36] K. V. Rajendran, L. Kennedy, K. S. Dunne, D. G. Gilheany, *Eur. J. Org. Chem.* **2010**, 5642–5649.

[37] K. V. Rajendran, J. S. Kudavalli, K. S. Dunne, D. G. Gilheany, *Eur. J. Org. Chem.* **2012**, 2720–2723.

[38] S. Yasui, S. Tojo, T. Majima, *J. Org. Chem.* **2005**, *70*, 1276–1280.

[39] S. Tojo, S. Yasui, M. Fujitsuka, T. Majima, *J. Org. Chem.* **2006**, *71*, 8227–8232.

[40] A. Ding, Y. Wang, R. Rios, J. Sun, H. Li, H. Guo, *Saudi Chem. Soc.* **2015**, *19*, 706–709.

[41] C. Lee, W. Yang, R. G. Parr, *Phys. Rev. B: Condens. Matter Mater. Phys.* **1988**, *37*, 785−789.

[42] A. D. Becke, *J. Chem. Phys.* **1993**, *98*, 5648−5652.

[43] Gaussian 16, Revision A.03, M. J. Frisch, G. W. Trucks, H. B. Schlegel, G. E. Scuseria, M. A. Robb, J. R. Cheeseman, G. Scalmani, V. Barone, G. A. Petersson, H. Nakatsuji, X. Li, M. Caricato, A. V. Marenich, J. Bloino, B. G. Janesko, R. Gomperts, B. Mennucci, H. P. Hratchian, J. V. Ortiz, A. F. Izmaylov, J. L. Sonnenberg, D. Williams-Young, F. Ding, F. Lipparini, F. Egidi, J. Goings, B. Peng, A. Petrone, T. Henderson, D. Ranasinghe, V. G.

Zakrzewski, J. Gao, N. Rega, G. Zheng, W. Liang, M. Hada, M. Ehara, K. Toyota, R. Fukuda, J. Hasegawa, M. Ishida, T. Nakajima, Y. Honda, O. Kitao, H. Nakai, T. Vreven, K. Throssell, J. A. Montgomery, Jr., J. E. Peralta, F. Ogliaro, M. J. Bearpark, J. J. Heyd, E. N. Brothers, K. N. Kudin, V. N. Staroverov, T. A. Keith, R. Kobayashi, J. Normand, K. Raghavachari, A. P. Rendell, J. C. Burant, S. S. Iyengar, J. Tomasi, M. Cossi, J. M. Millam, M. Klene, C. Adamo, R. Cammi, J. W. Ochterski, R. L. Martin, K. Morokuma, O. Farkas, J. B. Foresman, D. J. Fox, Gaussian, Inc., Wallingford CT, **2016**.

[44] SHELXS-2013 and SHELXL-2013: G. M. Sheldrick, Short History of SHELX. *Acta Crystallogr., Sect. A: Found. Crystallogr.* **2008**, *64*, 112–122.

[45] *Olex2:* O.V. Dolomanov, L. J. Bourhis, R. J. Gildea, J. A. K. Howard, H. Pushmann, *J. Appl. Crystallogr.* **2009**, *42*, 339–341.

[46] C. A. Parker, T. A. Joyce, *Trans*. *Faraday Soc*. **1966**, *62*, 2785–2792.

[47] I. B. Berlman, Handbook of Fluorescence Spectra of Aromatic Molecules. *Academic Press*. *N. Y*. **1971**.

[48] F. Weigend, R. Ahlrichs, *Phys. Chem. Chem. Phys.* **2005**, *7*, 3297.

[49] F. Weigend, *Phys. Chem. Chem. Phys.* **2006**, *8*, 1057.

[50] TURBOMOLE, A development of University of Karlsruhe and Forschungszentrum Karlsruhe GmbH, 1989-2007, TURBOMOLE GmbH, since **2007**; available from http://www.turbomole.com.

[51] R. Ahlrichs, M. Bär, M. Häser, H. Horn, C. Kölmel, *Chem. Phys. Lett.* **1989**, *162*,165.

[52] A. Hellweg, *J. Comput. Chem.* **2013**, *34*, 1835–1841.

[53] H. Shmidbaur, E. Weiss, *Angew. Chem. Int. Ed. Engl.* **1979**, *18*, 781.

Chapter VI

Concluding Remarks

Chapter VI

Concluding Remarks

Aggregation-induced emission (AIE) has studied for applications of organic light emitting diode (OLED) and luminescence sensor in the past 20 years. The mechanism of AIE has also been studied because understanding of the mechanism leads to the development of new AIE luminogens (AIEgens) and the control of the AIE. The early reports about the AIE mechanism insisted intramolecular motion such as the rotation of phenyl rings played a crucial role for AIE, the recent computational studies revealed that the large structural change in the excited state rather than such small motions closely related to the AIE behavior. Thus, in this thesis, the author focused on the large structural change in the excited state of AIE molecules tetraphenylethene (TPE) and phosphines derivatives.

In Chapter II, in order to liberate TPE from the restriction of intramolecular rotation, the author synthesized liquid TPE derivatives at room temperature. The liquefaction was attained by attaching long branched alkyl chains to pristine TPE. Notably the liquid TPE derivatives showed stronger luminescence than the solid TPE derivatives in the bulk state. Since the liquefaction should diminish the restriction of the intramolecular rotation of the phenyl rings, this result indicated that the intramolecular rotation was not important in AIE.

Inspired by the results of Chapter II, the author studied the C=C bond twist of TPE as the large structural change of the AIE in Chapter III. The photoexperiments of di-substituted TPE derivatives showed the negative correlation between *E-Z* isomerization and photoluminescence intensity; the TPE derivative strongly emitted but the isomerization was inhibited in the solid state, while the TPE derivative rapidly underwent the isomerization but the emission was quenched in the diluted solution. According to theoretical computations for

the TPE in the excited state, the central C=C bond of TPE was largely twisted in the excited state, and the structural change promoted the nonradiative decay from the excited state in the diluted solution. The calculations also revealed that the C=C bond twist was fully restricted in the solid state. From these results, author concluded the C=C bond twist was necessary for AIE behavior of TPE derivatives. Indeed, some AIE-inactive TPE derivatives showed the smaller C=C bond twist when they were excited.

In Chapter IV, in order to obtain deeper insight into the relationship between the C=C bond twist and AIE behavior, the author synthesized TPE macrocycles whose phenyl rings were crosslinked by flexible oligo-ethyleneglycol chains with different chain lengths and linkage positions. Because of the flexibility of the chains, most TPE macrocycles retained AIE behavior, however those having shorter chains, ortho-linkage derivatives, and trans isomers emitted luminescence even in the diluted solutions. The calculations about the degree of C=C bond twist of the TPE macrocycles in the excited state corresponded well to the experimental results; largely twisted derivatives retained AIE behavior and *vise versa*. Thus the calculation of the degree of C=C bond twist of TPE derivatives in the excited state should be useful for determination of AIEgen.

Although the studies of Chapter II-IV was limited to TPE derivatives among the AIEgens, in Chapter V, the author investigated the large structural change of phosphine that had been known as a AIEgen. The photoluminescence and circular dichroism (CD) spectroscopies of phosphine derivatives having poly aromatic hydrocarbons (PAHs) under photoirradiation indicated that the phosphines underwent pyramidal inversion in the diluted solution and which was a cause of AIE behavior. This was the first observation of the photo-induced pyramidal inversion of phosphine. The energy calculations of phosphines in the excited state supported that photo-induced pyramidal inversion easily occurred in the excited state, and moreover, it was revealed that the photo-induced pyramidal inversion was not specific to the PAH-containing phosphines but also occurred in general phosphines.

A key conclusion to be drawn from all the chapters together is the large structural changes of AIE molecules in the excited state lead to the AIE, which is not specific to TPE or phosphine derivatives. In other words, all AIE molecules showed the large structural change in

the excited state. This means that the study about AIE can lead to the study about molecular dynamics in the excited state as shown in Chapter V. The molecular dynamics in the excited state is not only related to AIE, but also to a variety of photophenomena such as photochemical reactions, photoisomerizations, twisted intramolecular charge-transfer and so on. Therefore, the conclusion obtained in this thesis will greatly expand the interpretation of AIE and are expected to serve as a foundation for the future research of molecular dynamics in the excited state.

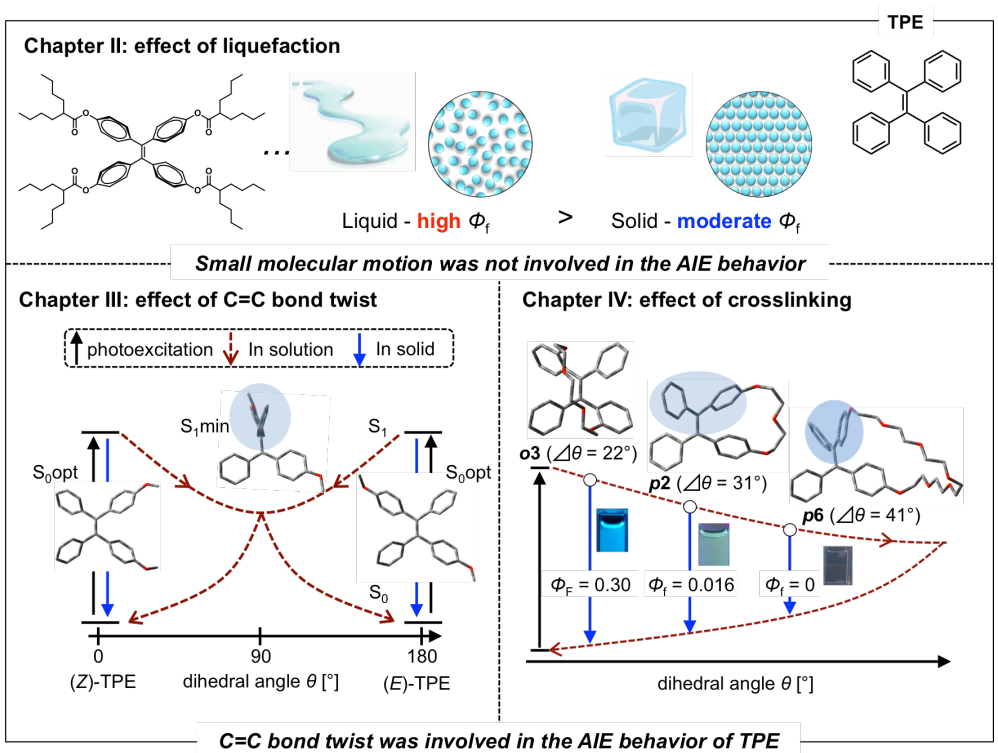

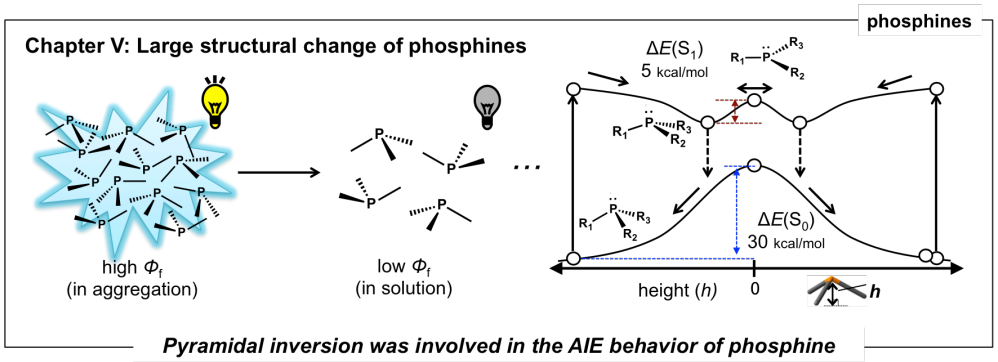

AIE molecules undergo large structural change in the excited state

List of Publication

List of Publication

Chapter II

"Liquefaction-induced emission enhancement of tetraphenylethene derivatives"

T. Machida, R. Taniguchi, T. Oura, K. Sada, K. Kokado, *Chem. Commun.* **2017**, *53*, 2378-2381.

Chapter III

"Twist of C=C Bond Plays a Crucial Role in the Quenching of AIE-Active Tetraphenylethylene Derivatives in Solution"

K. Kokado, T. Machida, T. Iwasa, T. Taketsugu, K. Sada, *J. Phys. Chem. C.* **2018**, *122*, 245-251.

Chapter IV

"Emissive Tetraphenylethylene (TPE) Derivatives in a Dissolved State Tightly Fastened by a Short Oligo(Ethylene Glycol) Chain"

Y. Tanaka, T. Machida, T. Noumi, K. Sada, K. Kokado, to be submitted

Chapter V

"Photoinduced Pyramidal Inversion Behavior of Phosphanes Involved with Aggregation-Induced Emission Behavior"

T. Machida, T. Iwasa, T. Taketsugu, K. Sada, K. Kokado, *Chem. Eur. J.* **2020**, *26*, 8028-8034.

Post Script

The studied presented in this thesis have been carried out under the direction of Professor Kazuki Sada at Graduate School of Chemical Science and Engineering, Hokkaido University during April 2015 - September 2020. The studies are concerned with "Investigation of Large Structural Change of Aggregation Induced Emission Molecules in the Excited State".

I wish to express my sincerest gratitude to Prof. Kazuki Sada and Prof. Kenta Kokado for their kind guidance, valuable suggestions and warm encouragement through this work. I am also deeply grateful to Prof. Akira Kakugo, Prof. Kenji Hirai and Prof. and Prof. Kabir Arif for their constant advices and helpful discussions during this work.

I would like to thank Prof. Tetsuya Taketsugu, Prof. Takanori Suzuki, Prof. Yasuchika Hasegawa for their valuable suggestions and discussions.

I am also grateful to Prof. Shizuka Anan, Dr. Takumi Ishiwata, Dr. Shunjiro nagata, Dr. Taihei Yamada, Dr. Shinya Sudo, Dr. Masaki Ito, Dr. Shizuka Anan, Dr. Masami Naya, Mr. Kyohe Uenishi, Mr. Ryosuke Taniguch, Mr. Tsuyoshi Oura, Mr. Toshiaki Noumi, Mr. Uma Tanaka and all the members of Prof. Sada's laboratory for their active collaboration.

I owe a very important debt to Prof. Masako Kato and Prof. Atsushi Kobayashi for the measurements of absolute quantum yield, fluorescence lifetime and XRD, Prof. Sadamu Takeda and Prof. Yoshiyuki Kageyama for the use of DSC, Prof. Tamotsu Inabe and Prof. Jun Harada for the use of XRD.

I wish to express special thanks to Prof. Takashi Nakanishi and all the members of his group for their hospitable support and valuable suggestions during my stay in National Institution for Material Science (NIMS).

I wish to express special thanks to Prof. G. Dan Pantos and all the members of his laboratory for their hospitable support and valuable suggestions during my stay in Bath, UK.

I am in acknowledgement of Research Fellowship of the Japan Society for the Promotion of Science (JSPS) for Young Scientists for Financial Support. Research activity in Bath University, UK was supported by Japan Student Services Organization (JASSO), Short Visit Program.

Finally, I express deep appreciation to my friends, family, especially my parents Hiroyuki Machida and Kaoru Machida for their continuous assistance and encouragement.

Takashi Machida